NAVAL POSTGRADUATE SCHOOL

MONTEREY, CALIFORNIA

THESIS

AEROSOL SCATTERING PHASE FUNCTION RETRIEVAL FROM POLAR ORBITING SATELLITES

by

Daniel P. Wunder

March 2005

Thesis Advisor:	Philip A. Durkee
Second Reader:	Carlyle H. Wash

Approved for public release, distribution is unlimited

THIS PAGE INTENTIONALLY LEFT BLANK

REPORT DOCUMENTATION PAGE			*Form Approved OMB No. 0704-0188*
Public reporting burden for this collection of information is estimated to average 1 hour per response, including the time for reviewing instruction, searching existing data sources, gathering and maintaining the data needed, and completing and reviewing the collection of information. Send comments regarding this burden estimate or any other aspect of this collection of information, including suggestions for reducing this burden, to Washington headquarters Services, Directorate for Information Operations and Reports, 1215 Jefferson Davis Highway, Suite 1204, Arlington, VA 22202-4302, and to the Office of Management and Budget, Paperwork Reduction Project (0704-0188) Washington DC 20503.			
1. AGENCY USE ONLY *(Leave blank)*	2. REPORT DATE March 2005	3. REPORT TYPE AND DATES COVERED Master's Thesis	
4. TITLE AND SUBTITLE: Aerosol Scattering Phase Function Retrieval From Polar Orbiting Satellites		5. FUNDING NUMBERS	
6. AUTHOR(S) Daniel P. Wunder			

7. PERFORMING ORGANIZATION NAME(S) AND ADDRESS(ES)
    Naval Postgraduate School
    Monterey, CA 93943-5000
		8. PERFORMING ORGANIZATION REPORT NUMBER	

9. SPONSORING /MONITORING AGENCY NAME(S) AND ADDRESS(ES) N/A		10. SPONSORING/MONITORING AGENCY REPORT NUMBER	
11. SUPPLEMENTARY NOTES The views expressed in this thesis are those of the author and do not reflect the official policy or position of the Department of Defense or the U.S. Government.			
12a. DISTRIBUTION / AVAILABILITY STATEMENT Approved for public release, distribution is unlimited		12b. DISTRIBUTION CODE A	

13. ABSTRACT (maximum 200 words)

        The retrieval of an aerosol scattering phase function using a multi-satellite technique is proposed. A total of 33 phase functions were derived from 18 smoke cases and 15 dust cases. Each case was interrogated using four to nine satellite passes over the aerosol in a two to four hour time frame. The radiance values for the Red and Near-Infrared (NIR) channels were combined with backscattering angles to determine the shape of the scattering phase function. The radiance values were input into the Naval Postgraduate School (NPS) aerosol model to determine optical depths and sample phase functions. A comparison was made between the actual phase functions retrieved and the NPS model phase functions. It was found that the phase functions for the smoke cases more closely matched the model phase functions than in the dust cases. Some conclusions could be drawn about the actual aerosol size and density distribution based on how well it matched the model phase function. Further analysis is necessary to define the exact size and number of the aerosol particles. Fully understanding the aerosol composition is crucial in determining its effects on military sensors and impacts to operations.

14. SUBJECT TERMS Scattering phase function, aerosol optical depth, aerosol model, Mie scattering, smoke, dust, aerosol			15. NUMBER OF PAGES 97
			16. PRICE CODE
17. SECURITY CLASSIFICATION OF REPORT Unclassified	18. SECURITY CLASSIFICATION OF THIS PAGE Unclassified	19. SECURITY CLASSIFICATION OF ABSTRACT Unclassified	20. LIMITATION OF ABSTRACT UL

NSN 7540-01-280-5500

Standard Form 298 (Rev. 2-89)
Prescribed by ANSI Std. 239-18

THIS PAGE INTENTIONALLY LEFT BLANK

AEROSOL SCATTERING PHASE FUNCTION RETRIEVAL FROM POLAR
ORBITING SATELLITES

Daniel P. Wunder
Captain, United States Air Force
B.S., Florida State University, 1998

Submitted in partial fulfillment of the
requirements for the degree of

MASTER OF SCIENCE IN METEOROLOGY

from the

NAVAL POSTGRADUATE SCHOOL
March 2005

Author: Daniel P. Wunder

Approved by: Philip A. Durkee
                 Thesis Advisor

                 Carlyle H. Wash
                 Second Reader

                 Philip A. Durkee
                 Chairman, Department of Meteorology

THIS PAGE INTENTIONALLY LEFT BLANK

ABSTRACT

The retrieval of an aerosol scattering phase function using a multi-satellite technique is proposed. A total of 33 phase functions were derived from 18 smoke cases and 15 dust cases. Each case was interrogated using four to nine satellite passes over the aerosol region in a two to four hour time frame. The radiance values for the red and near-infrared (NIR) channels were combined with backscattering angles to determine the shape of the scattering phase function. The radiance values were input into the Naval Postgraduate School (NPS) aerosol model to determine optical depths and sample phase functions. A comparison was made between the actual phase functions retrieved and the NPS model phase functions. It was found that the phase functions for the smoke cases more closely matched the model phase functions than in the dust cases. Some conclusions could be drawn about the actual aerosol size and density distribution based on how well it matched the model phase function. Further analysis is necessary to define the exact size and number of the aerosol particles. Fully understanding the aerosol composition is crucial in determining its effects on military sensors and impacts to operations.

THIS PAGE INTENTIONALLY LEFT BLANK

TABLE OF CONTENTS

LIST OF FIGURES

THIS PAGE INTENTIONALLY LEFT BLANK

LIST OF TABLES

THIS PAGE INTENTIONALLY LEFT BLANK

ACKNOWLEDGMENTS

THIS PAGE INTENTIONALLY LEFT BLANK

I. INTRODUCTION

A. MOTIVATION

The Air Force Weather (AFW) Strategic Plan and Vision outlines eight "Transformation Vectors" that will radically change the weather core processes of collection, analysis, prediction, tailoring, and dissemination. Transformation vector #1 is to integrate environmental information collection into the theater Intelligence, Surveillance and Reconnaissance (ISR) collection plan. Issue #1 of transformation vector #1 is to improve the ability to collect globally target-quality environmental information in hostile and data-denied areas to build an accurate real-time picture of the environment for battlespace awareness and decision superiority (Air Force Weather, 2004). Obtaining a complete picture of atmospheric aerosol properties is a crucial step in obtaining full battlespace awareness.

Satellite data from several polar orbiting satellites was used in this thesis to determine the scattering phase function of an aerosol region. Data from the Moderate Resolution Imaging Spectroradiometer (MODIS) instrument onboard the Earth Observing System (EOS) satellites, the Advanced Very High Resolution Radiometer (AVHRR) onboard the National Oceanographic and Atmospheric Administration (NOAA) satellites, and the Sea-viewing Wide Field-of-view Sensor (SeaWiFS) onboard the National Aeronautics and Space Administration (NASA) satellite was used to determine the scattering phase function for various aerosol areas.

Currently NASA's Multi-angle Imaging SpectroRadiometer (MISR) (Figure 1) is performing a similar technique for aerosol and terrain interrogation. The MISR views the earth in a narrow swath from nine different view angles. Most satellite instruments look only straight down, or toward the edge of the planet. To fully understand Earth's climate, and to determine how it may be changing, we need to know the amount of sunlight that is scattered in different directions under natural conditions. MISR is an instrument designed to address this need; it views

1

the Earth with sensors pointed at nine different angles. One sensor points toward nadir, and the others provide forward and aftward view angles, at the Earth's surface, of 26.1°, 45.6°, 60.0°, and 70.5°. As the instrument flies overhead, each region of the Earth's surface is successively imaged by all nine sensors in each of four wavelengths (blue, green, red, and near-infrared). With its nine different look angles, MISR is uniquely capable of observing cloud and aerosol plume structures in the atmosphere three-dimensionally, as well as measuring the relative heights and types of clouds. Its stereoscopic measurement abilities enable MISR to observe the amount of sunlight that is reflected at various angles. MISR will also help scientists trace smoke and aerosol plumes back to their sources (NASA Jet Propulsion Laboratory 2005).
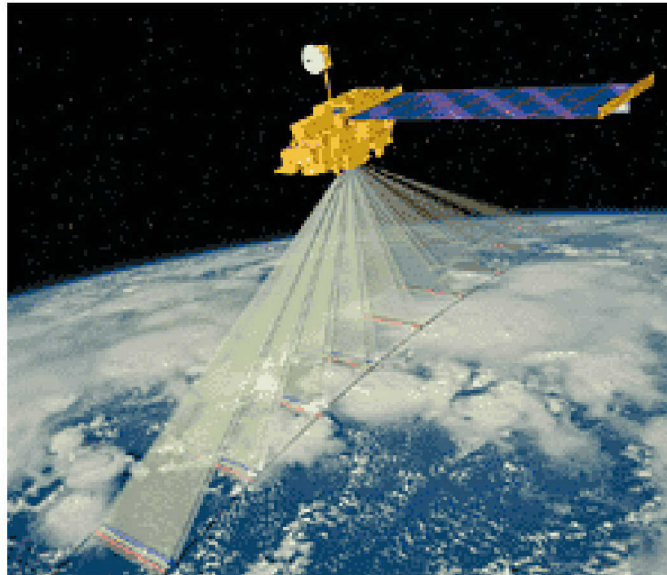
Figure 1.   Multi-angle Imaging SpectroRadiometer (MISR)

B.   OBJECTIVES

Improving visibility estimates in areas of limited data has been and will continue to be an area of interest for the military war-fighter. Many tools are available to assist in the visibility estimates. However, most are based on a single sized spherical aerosol model. Unfortunately aerosols are often mixed in composition, size and shape. This leads to a very complex scattering regime of the aerosols, which is not handled well by any single aerosol model. The

purpose of this thesis is to determine the scattering phase function of an aerosol of unknown size, shape, and composition. This in turn would lead to better optical depth interpretation, which would lead to better visibility estimation.

The thesis will start with a description of the instruments used for data collection. That is followed by a brief explanation of scattering theory. A large section is devoted to the procedures used to determine the scattering phase function. The results section describes the findings of this study. The last section contains the conclusions and some recommendations for further study.

THIS PAGE INTENTIONALLY LEFT BLANK

II. BACKGROUND

A. SATELLITE INSTRUMENTS

Several different satellite instruments were used for the collection of radiance values in the red and near-infrared (NIR) wavelengths

1. Advanced Very High Resolution Radiometer (AVHRR)

The Advanced Very High Resolution Radiometer (AVHRR) provides as few as four to as many as six bands of multispectral data from the NOAA polar-orbiting satellite series. There has been fairly continuous global coverage since June 1979, with morning and afternoon acquisitions available (Table 1). The resolution is 1.1 kilometer at nadir.

Satellite #	Dates	Pass	# of bands
NOAA-6	6/79 – 11/86	am	4
NOAA-7	8/81 – 6/86	pm	5
NOAA-8	5/83 – 10/85	am	4
NOAA-9	2/85 – 11/88	pm	5
NOAA-10	11/86 – 9/91	am	4
NOAA-11	11/88 – 9/94	pm	5
NOAA-12	5/91 – 12/94	am	5
NOAA-13	failed	pm	n/a
NOAA-14	12/94 – present	pm	5
NOAA-15	5/98 – present	am	5
NOAA-16	9/00 – present	pm	6
NOAA-17	10/02 – present	am	6

Table 1. NOAA satellite properties and history
(from US Geological Survey, 2004)

In Table 2 the NOAA bands are listed. Bands one and two were used to collect the red and NIR data respectively. The spectral response curves for Bands one, two and three are shown in Figures 2, 3 and 4. Their significance is explained in further detail in the Procedures section of this thesis.

5

Band #	Satellites: NOAA-6,8,10	Satellites: NOAA-7,9,11,12,14	Satellites: NOAA-15,16,17	IFOV
1	0.58 – 0.68	0.58 – 0.68	0.58 – 0.68	1.39
2	0.725 – 1.10	0.725 – 1.10	0.725 – 1.0	1.41
3	3.55 – 3.93	3.55 – 3.93		1.51
3A			1.58 – 1.64	1.51
3B			3.55 – 3.93	1.51
4	10.50 – 11.50	10.3 – 11.3	10.3 – 11.3	1.41
5	band 4 repeated	11.5 – 12.5	11.5 – 12.5	1.30
	(micrometers)	(micrometers)	(micrometers)	(milliradians)

Table 2.   NOAA AVHRR Bands
(from US Geological Survey, 2004)

Figure 2.   Spectral Response Curve for NOAA-17 AVHRR/3 Channel 1
(from NOAA, 2002)

6
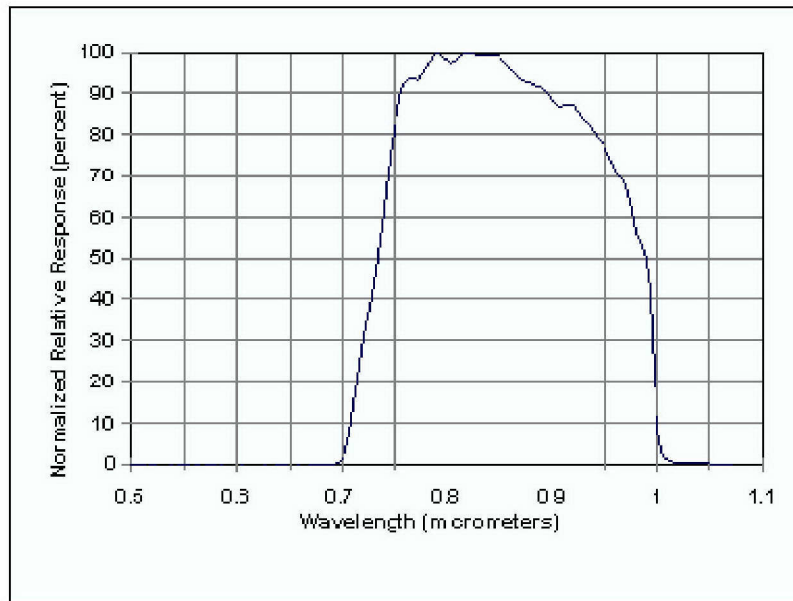
Figure 3.   Spectral Response Curve for NOAA-17 AVHRR/3 Channel 2
(from NOAA, 2002)
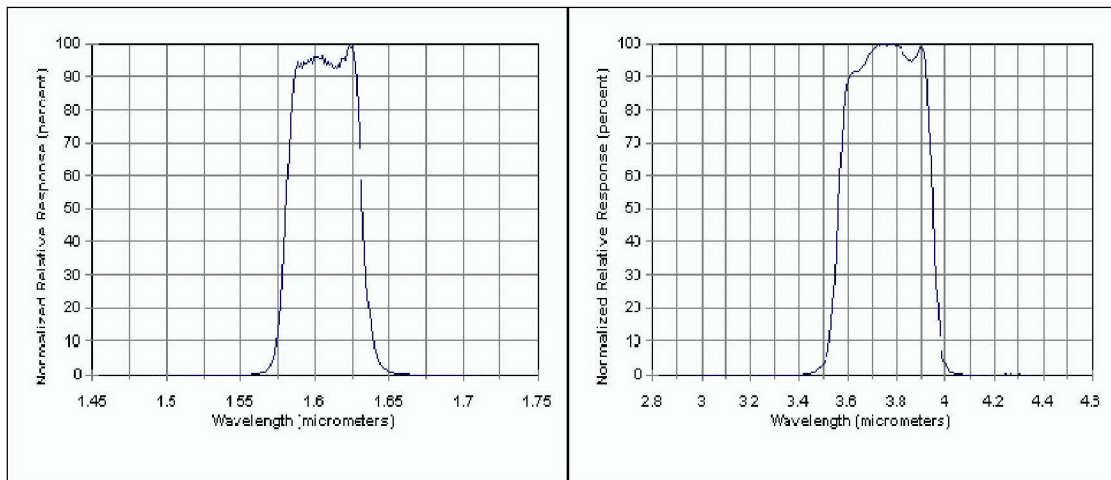
Figure 4.   Spectral Response Curve for NOAA-17 AVHRR/3 Channel 3A/3B
(from NOAA, 2002)

2.   Moderate Resolution Imaging Spectroradiometer (MODIS)

MODIS (or Moderate Resolution Imaging Spectroradiometer) is a key instrument aboard the Terra (EOS AM) and Aqua (EOS PM) satellites. Terra's orbit around the Earth is timed so that it passes from north to south across the equator in the morning (10:30 a.m. LT), while Aqua passes south to north over

7

the equator in the afternoon (1:30 p.m. LT). Terra MODIS and Aqua MODIS are viewing the entire earth's surface every 1 to 2 days, acquiring data in 36 spectral bands, or groups of wavelengths (Tables 3 and 4).   Bands one and two were used to collect the red and NIR data respectfully.

Primary Use	Band	Bandwidth[1]	Spectral Radiance[2]	Required SNR[3]
Land/ Cloud/ Aerosols Boundaries	1	620 – 670	21.8	128
	2	841 – 876	24.7	201
Land/ Cloud/ Aerosols Properties	3	459 – 479	35.3	243
	4	545 – 565	29.0	228
	5	1230 – 1250	5.4	74
	6	1628 – 1652	7.3	275
	7	2105 – 2155	1.0	110
Ocean Color/ Phytoplankton/ Biogeochemistry	8	405 – 420	44.9	880
	9	438 – 448	41.9	838
	10	483 – 493	32.1	802
	11	526 – 536	27.9	754
	12	546 – 556	21.0	750
	13	662 – 672	9.5	910
	14	673 – 683	8.7	1087
	15	743 – 753	10.2	586
	16	862 – 877	6.2	516
Atmospheric Water Vapor	17	890 – 920	10.0	167
	18	931 – 941	3.6	57
	19	915 – 965	15.0	250

Table 3.   MODIS Bands 1-19
(from Conboy, 2002)

Primary Use	Band	Bandwidth[1]	Spectral Radiance[2]	Required NE[delta]T(K)[4]
Surface/Cloud Temperature	20	3.660 – 3.840	0.45(300K)	0.05
	21	3.929 – 3.989	2.38(335K)	2.00
	22	3.929 – 3.989	0.67(300K)	0.07
	23	4.020 – 4.080	0.79(300K)	0.07
Atmospheric Temperature	24	4.433 – 4.498	0.17(250K)	0.25
	25	4.482 – 4.549	0.59(275K)	0.25
Cirrus Clouds Water Vapor	26	1.360 – 1.390	6.00	150(SNR)
	27	6.535 – 6.895	1.16(240K)	0.25
	28	7.175 – 7.475	2.18(250K)	0.25
Cloud Properties	29	8.400 - 8.700	9.58(300K)	0.05
Ozone	30	9.580 - 9.880	3.69(250K)	0.25
Surface/Cloud Temperature	31	10.780 - 11.280	9.55(300K)	0.05
	32	11.770 - 12.270	8.94(300K)	0.05
Cloud Top Altitude	33	13.185 - 13.485	4.52(260K)	0.25
	34	13.485 - 13.785	3.76(250K)	0.25
	35	13.785 - 14.085	3.11(240K)	0.25
	36	14.085 - 14.385	2.08(220K)	0.35

[1] Bands 1 to 19 are in nm; Bands 20 to 36 are in µm
[2] Spectral Radiance values are (W/m^2-µm-sr)
[3] SNR = Signal-to-noise ratio
[4] NE(delta)T = Noise-equivalent temperature difference
Note: Performance goal is 30-40% better than required

Table 4.   MODIS Bands 20-36
(from Conboy, 2002)

3.   Sea-viewing Wide Field-of-view Sensor (SeaWiFS)

The purpose of the Sea-viewing Wide Field-of-view Sensor (SeaWiFS) project is to provide quantitative data on global ocean bio-optical properties to the Earth science community. The NASA SeaWiFS instrument is composed of an optical scanner and an electronics module (Figure 5). The eight bands (Table 5), most of which are visible wavelengths, make it very useful for the interrogation of aerosols. Another key feature of the SeaWiFS sensor is its scanner tilt mechanism that enables the instrument to be oriented in the along-track direction from +20 to -20 degrees to avoid sun glint from the sea surface. Tilting the entire

scanner, rather than only a section of the optical train, assures that the SeaWiFS calibration, polarization, and angular scanning characteristics will be identical for all tilt positions and, thereby, simplifies the ground processing of in-flight data.

Instrument Bands	
Band	Wavelength
1	402-422 nm
2	433-453 nm
3	480-500 nm
4	500-520 nm
5	545-565 nm
6	660-680 nm
7	745-785 nm
8	845-885 nm
Mission Characteristics	
Orbit Type	Sun Synchronous at 705 km
Equator Crossing	Noon +20 min, descending
Orbital Period	99 minutes
Swath Width	2,801 km LAC/HRPT (58.3 degrees)
Swath Width	1,502 km GAC (45 degrees)
Spatial Resolution	1.1 km LAC, 4.5 km GAC
Real-Time Data Rate	665 kbps
Revisit Time	1 day
Digitization	10 bits

Table 5.   SeaWiFS Bands and Mission Characteristics
(from Feldman, 1997)
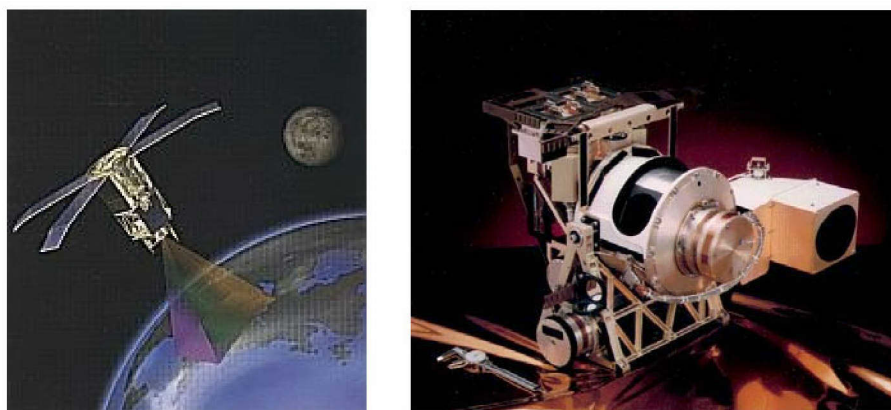
Figure 5.   NASA Satellite and SeaWiFS Sensor
(from Feldman, 1997)

B.   AERONET

(AErosol RObotic NETwork) is an optical ground based aerosol monitoring network and data archive supported by NASA's Earth Observing System and expanded by federation with many non-NASA institutions.   The network hardware consists of identical automatic sun-sky scanning spectral radiometers owned by national agencies and universities.   Data from this collaboration provides globally distributed near real time observations of aerosol spectral optical depths, aerosol size distributions, and precipitable water in diverse aerosol regimes.   The data undergo preliminary processing (real time data), reprocessing (final calibration ~6 mo. after data collection), quality assurance, archiving and distribution from NASA's Goddard Space Flight Center master archive and several identical data bases maintained globally.   The data provide algorithm validation of satellite aerosol retrievals, as well as characterization of aerosol properties that are unavailable from satellite sensors.

The primary instrument of the AERONET is the CIMEL Electronique 318A spectral radiometer (Figure 6) is a solar powered weather hardy robotically pointed sun and sky spectral radiometer.   The radiometer makes two basic measurements, either direct sun or sky, both within several programmed sequences.   The direct sun measurements are made in eight spectral bands at wavelengths of 340, 380, 440, 500, 670, 870, 940 and 1020 nm.   A

11

preprogrammed sequence of measurements is taken by these instruments. Optical thickness is calculated from spectral extinction of direct beam radiation at each wavelength based on the Beer-Bouguer Law. Attenuation due to Rayleigh scatter, absorption by ozone (from interpolated ozone climatology atlas), and gaseous pollutants is estimated and removed to isolate the aerosol optical thickness (AOT). Sky radiance measurements are inverted with the Dubovik and Nakajima inversions to provide aerosol properties of size distribution and phase function over the particle size range of 0.1 to 5 μm (Holbren, 2004). Although the data from the AERONET is highly accurate it has limited coverage. It was often difficult to locate a sensor in close proximity to the over the water aerosol regions being interrogated .Displayed in Figure 7 is a sample of the AERONET optical thickness output. All of the AERONET data products used can be seen in Appendix C. The graphics were generated at the NASA, Goddard Space Flight Center web site (http://aeronet.gsfc.nasa.gov/data_menu.html).

Figure 6.   CIMEL Spectral Radiometer
(from Holbren, 2004)
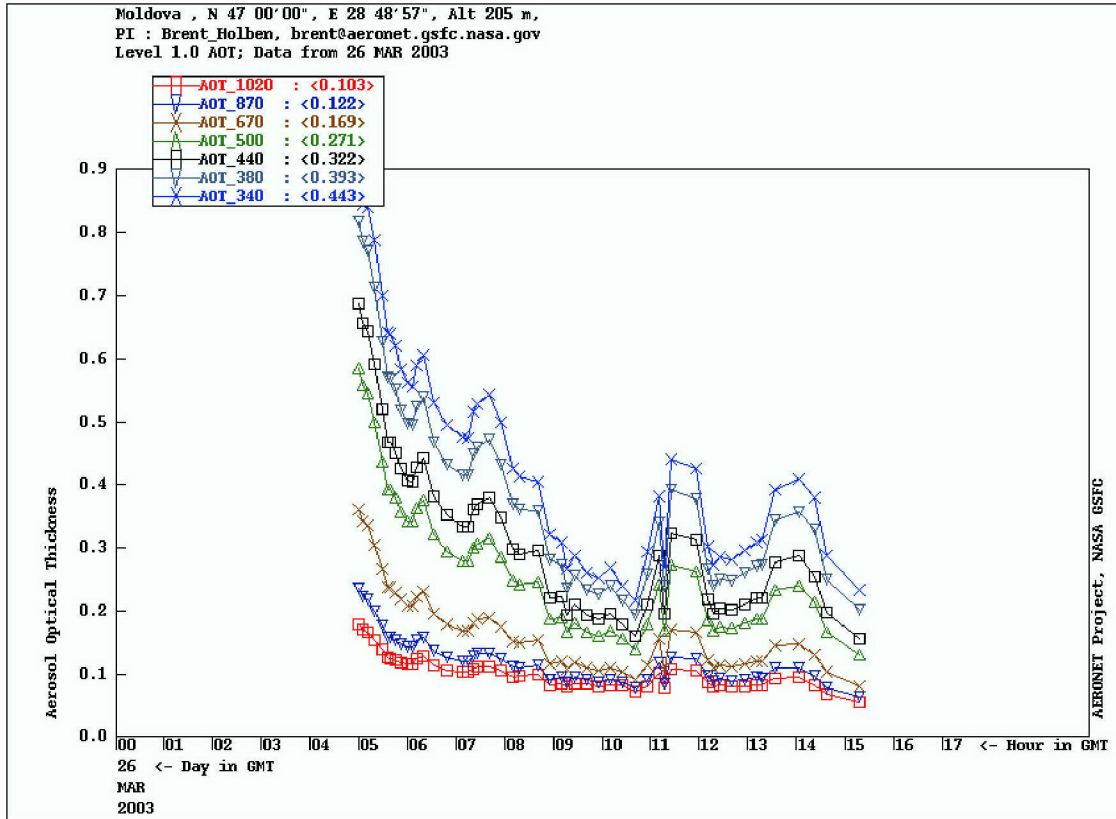
Figure 7.   AERONET Optical Thickness output for Moldova near the Black Sea
(from NASA GSFC, 2005a)

C.   SCATTERING

Radiation scatted from a particle is a function of particle size, particle shape, particle index of refraction, wavelength of radiation, and viewing geometry. For a spherical scatterer, the scattered radiation is a function of only the viewing angle, index of refraction, and the size parameter defined as:

$$\chi = \frac{2\pi r}{\lambda}$$

(1)

where r is the radius of the sphere (from Kidder and Vonder Haar, 1995). The size parameter can be used to divide scattering into three regimes: Geometric, Rayleigh, and Mie (Figure 8). The latter being the regime of interest for aerosols in the visible and near-infrared wavelengths.

13
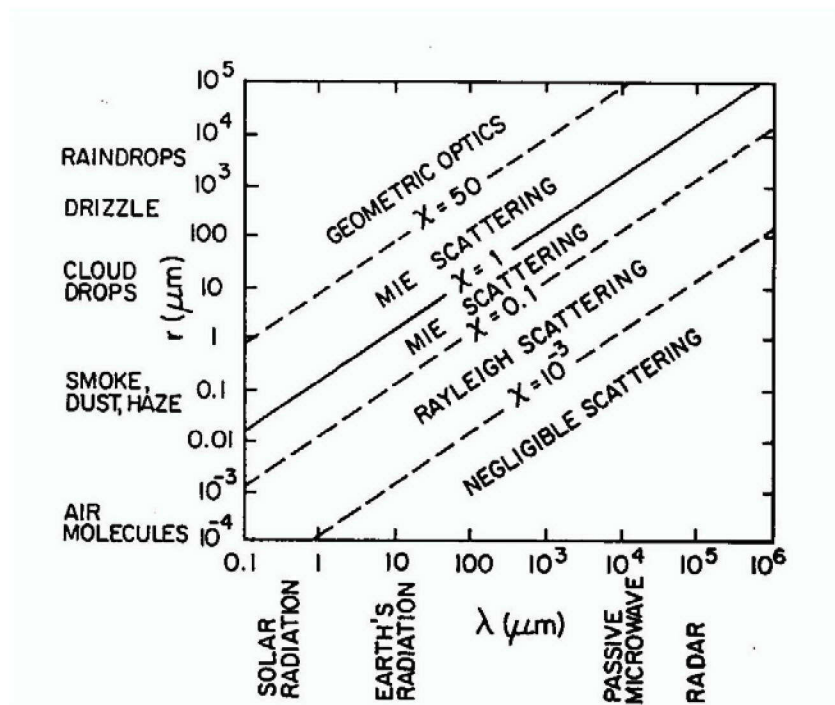
Figure 8.   Scattering Regimes
(from Wallace and Hobbs, 1977)

1.   Geometric

For χ greater than about 50, the sphere is large compared to the wavelength of radiation. In this regime, rays which are reflected and refracted at the surface of a scatterer can be traced. Sun glint reflected off of the surface of the water is an example of geometric optics. The water surface is somewhat rough therefore the solar reflection is blurred and larger than the sun.

2.   Rayleigh

For χ less than about 0.1, the particle is small compared to the wavelength of radiation. In this regime, atmospheric molecules act as Rayleigh scatterers for visible and ultraviolet radiation. Rayleigh scattering is insensitive to particle shape. Rayleigh particles scatter equally well in the forward as well as backward direction (Figure 9). Scattering is negligible for χ less than 10^{-3}.

3.   Mie

For χ in the range of 0.1-50, the particle size is comparable to the wavelength of radiation. It is in the Mie regime that aerosols interact with the

14

visible and near-infrared wavelengths. The scattering properties become very complicated in the Mie regime. The scattering phase function is dependent upon the angle of incident radiation to the aerosol. It can be seen in Figure 9 that there is a very strong forward scattering component that increases logarithmically as the χ-value increases. It is also noted that the backscattered radiation varies dramatically with the backscattering angle.
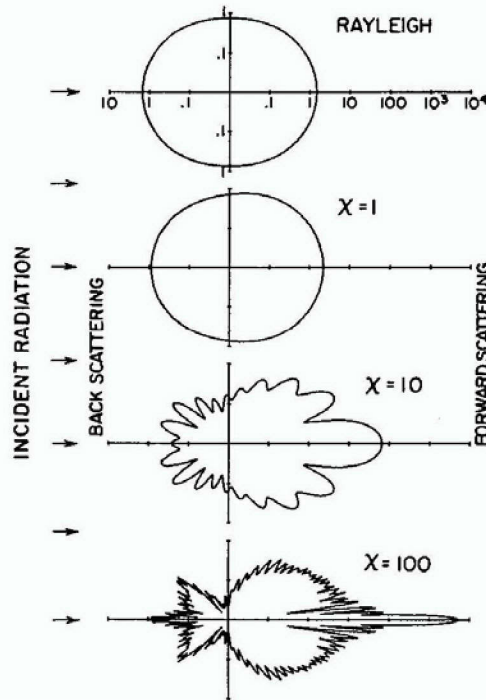
Figure 9. Polar plots of the scattering phase function for several size parameters (from Kidder and Vonder Haar, 1995)

D. ASSUMPTIONS

Some necessary assumptions had to be made in working with the satellite data. The total radiance reaching the satellite sensor can be broken down into the following expression (from Durkee et al., 1986):

$$L_t = L_o \tau_o + L_r + L_a \qquad (2)$$

where L_t is the total radiance reaching the sensor, L_o is the radiance leaving the surface, τ_o is the transmittance from the surface to the sensor, L_r is the radiance

15

from Rayleigh scattering by atmospheric molecules, and L_a is the radiance backscattered by the aerosol. An illustration of the radiance paths reaching the satellite can be seen in Figure 10.
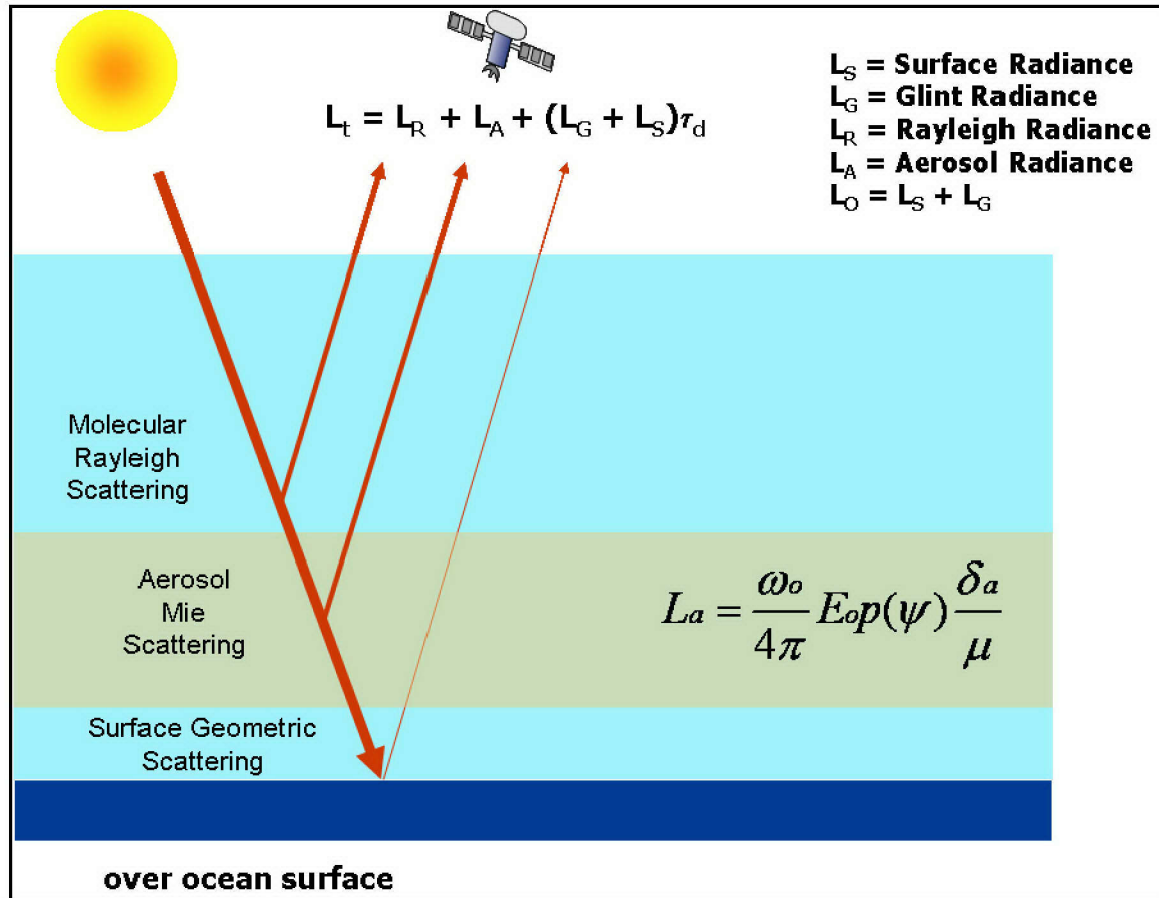
Figure 10. Breakdown of total radiance
(after Durkee, 2004)

It is assumed that the molecular Rayleigh scattering remains constant during the sample period. It can be seen in Figure 9 that the Rayleigh scattering is more nearly constant in all directions then for Mie scattering. It is also assumed that the surface radiance and transmittance do not change over the sample period. With these assumptions that leaves the radiance from the aerosol as the dominant contributor to the changes in the total radiance.

The procedures section that follows describes how the total radiance values were determined from the satellite data. The total radiance values vary form one satellite to the next because the Mie scattering from the aerosol is changing as the satellite and solar angles are changing. The procedures section describes the complete process for determining the backscattering angle and combining it with the radiance values to ultimately produce a scattering phase function for the aerosol.

THIS PAGE INTENTIONALLY LEFT BLANK

III. PROCEDURES

A. CASE SELECTION

Cases were selected based on the satellites' ability to visibly see aerosols and track their movement over water. Higher latitudes are better, since this increased the chance of getting overlapping passes on the subsequent orbit from a single satellite. The selection of a case required there to be a cloud free environment. Clouds would contaminate the radiance values backscattered from the aerosols. Sun glint also caused a problem with the radiance that reached the satellite sensor. It was therefore necessary to ensure that no sun glint was in the area of the aerosols being interrogated. Once a possible case was identified the raw satellite data was ordered from archives and then loaded into Terascan for viewing and processing.

B. TERASCAN

Terascan was used to display the raw satellite data from NOAA, EOS, and SeaWiFS. The Terascan software allowed for the retrieval of all pertinent data at any specific pixel. The values of interest for these cases were radiance values in the red-visible and near-IR wavelengths, solar zenith angle, solar azimuth angle, sensor zenith angle, and sensor azimuth angle. The radiance values for the aerosol were determined by sampling a 100-pixel area over the aerosol region. Standard statistical methods from Terascan were used to determine the mean and standard deviation of the radiance values in the sample area. This allowed for greater confidence in using the radiance value to determine the scattering phase function. The values at the center of the 100-pixel box were used for solar zenith, solar azimuth, sensor zenith, and sensor azimuth. It was necessary to obtain these radiance and angle values from a series of satellite images, each of which viewed the aerosol region of interest from different view angles.

C. DATA RETRIEVAL AND INTEROGATION

1. Radiance Values

For the red wavelength: Channel 1 ($0.620\text{-}0.670\,\mu m$) was used for MODIS, Channel 1 ($0.580\text{-}0.680\,\mu m$) was used for AVHRR, and Channel 6

(0.660-0.680 μm) was used for SeaWiFS. For the near-infrared wavelength: Channel 2 (0.841-0.876 μm) was used for MODIS, Channel 2 (0.725-1.0 μm) was used for AVHRR, and Channel 8 (0.845-0.885 μm) was used for SeaWiFS.

To determine the radiance values a 100-pixel sample was taken within the aerosol-laden regions of the scene. The radiance value for each channel was taken as the mean value of that 100-pixel sample (Figure 11).
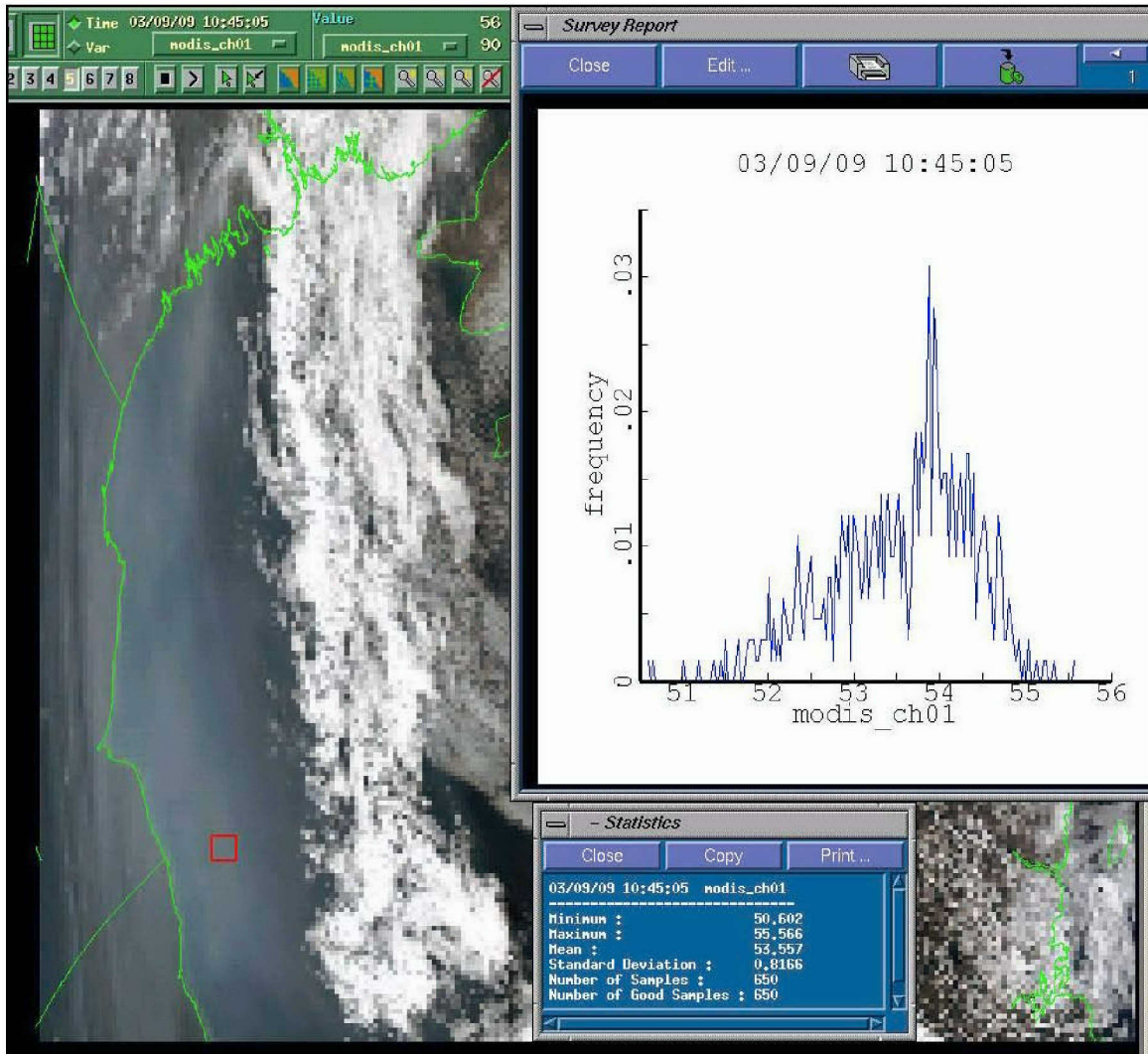
Figure 11.   Statistical Sample of radiances for MODIS Channel 1.

Various conversion factors were used to ensure all radiance outputs were in the same units (watts/m^2/μm). The MODIS data required no conversion while

20

the AVHRR and SeaWiFS data required some conversions. The AVHRR output was in albedo which required the following conversion:

$$(\text{Albedo})^* E_o / \pi = (\text{watts/m}^2 / \mu m), \tag{3}$$

where E_o is the solar constant at the centered effective wavelength. The values of E_o for AVHRR channel 1 and 2 were 1644 watts/m^2/μm and 1034 watts/m^2/μm respectively. The output for SeaWiFS was in radiance and only required a correction factor of 10 to be in the standard units:

$$(\text{SeaWiFS mW/cm}^2 / \mu m)^* 10 = (\text{watts/m}^2 / \mu m) \tag{4}$$

2.   Linear Extrapolation

A linear extrapolation was necessary to ensure that all the radiance values were being compared at the same wavelength. The wavelengths for the AVHRR on NOAA 14 were used in order to match the NPS aerosol model described below. For the red wavelength: MODIS Channel 1 has a centered effective wavelength at $0.645\,\mu m$; AVHRR Channel 1 has a centered effective wavelength at $0.6357\,\mu m$; and SeaWiFS Channel 6 has a centered effective wavelength at $0.670\,\mu m$. For the near-infrared wavelength: MODIS Channel 2 has a centered effective wavelength at $0.8585\,\mu m$; AVHRR Channel 2 has a centered effective wavelength at $0.85397\,\mu m$; and SeaWiFS Channel 8 has a centered effective wavelength at $0.865\,\mu m$ (NOAA, 2002). A linear extrapolation was accomplished for MODIS channels 1 and 2 by finding the slope of the radiance versus wavelength line between channels 1 and 2, then applying a linear extrapolation to the AVHRR center effective wavelength of $0.6357\,\mu m$ for the red wavelength and $0.85397\,\mu m$ for the near-infrared wavelength.

The following formula is an example of the linear extrapolation of the MODIS channel 1 radiance value to the radiance value at the AVHRR Channel 1 center effective wavelength:

$$L_{AC} = \frac{L_2 - L_1}{(\lambda_2 - \lambda_1)}(\lambda_1 - \lambda_{AC}) + L_1, \tag{5}$$

where L_1 and L_2 are the radiance values for MODIS channels 1 and 2; λ_1 and λ_2 are the wavelengths for MODIS channels 1 and 2; λ_{AC} is the center effective wavelength for AVHRR channel 1; and L_{AC} is the linear extrapolated radiance value for the red wavelength. A graphic illustration of the linear extrapolation can be seen in Figure 12.
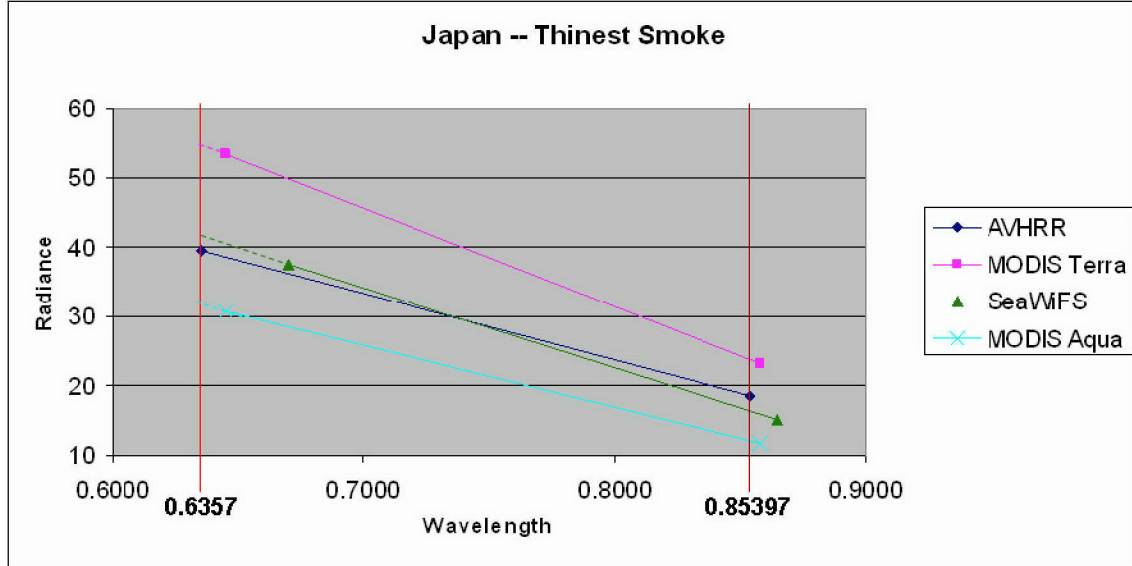
Figure 12.   Linear Extrapolation of radiance values to AVHRR red and NIR center effective wavelengths

The same procedures and similar formulas were used to extrapolate the radiance values for MODIS channel 2, SeaWiFS channels 6 and 8 to the radiance values of the center effective wavelengths of AVHRR channels 1 and 2. The net result is that all radiance values were extrapolated to radiance values centered at $0.6357 \, \mu m$ for the red wavelength and $0.85397 \, \mu m$ for the near-infrared wavelength.

3.   Phase Scattering Angle

The solar zenith (θ'), solar azimuth (ϕ'), sensor zenith (θ), and sensor azimuth (ϕ) angles obtained from Terrascan were used to determine the

22

backscattering angle (ψ). The values for the angles were taken from the center of the 100-pixel sample box and used in the following equations for the MODIS data.

$$\cos\psi' = \cos\theta\cos\theta' + \sin\theta\sin\theta'\cos(\phi - \phi') \qquad (6)$$

$$\psi = 180 - \psi' \qquad (7)$$

The backscattering angle (ψ) was obtained directly from equation seven for the AVHRR and SeaWiFS data, since the $\cos\psi'$ was one of the outputs in terascan.

4.   Plotting the Phase Scattering Function

The backscattering angles were used with the radiance values in plotting the scattering phase function. The following formula was used to convert the radiance values into a phase function as a function of the backscattering angle (from Durkee et al., 1986).

$$L_a = \frac{\omega_o}{4\pi} E_o p(\psi) \frac{\delta_a}{\mu} \qquad , \qquad (8)$$

and,

$$p(\psi) = \frac{L_a \mu 4\pi}{E_o \delta_a \omega_o} \qquad , \qquad (9)$$

where L_a is the aerosol radiance at the center effective wavelength, μ is the solar zenith angle, E_o is the aerosol solar constant at the center effective wavelength, δ_a is the aerosol optical depth, and ω_o is the single scattering albedo. All of the values at this point are known with the exception of the optical depth.

The aerosol optical depth was determined using the NPS aerosol model (Figure 13). The optical depths from the NPS model were compared against any AERONET observations in close proximity. This was to ensure the optical depth

values from the model were a reasonable comparison to the values observed throughout the day by the AERONET sensor. The AERONET optical depth data can be seen in Appendix C.
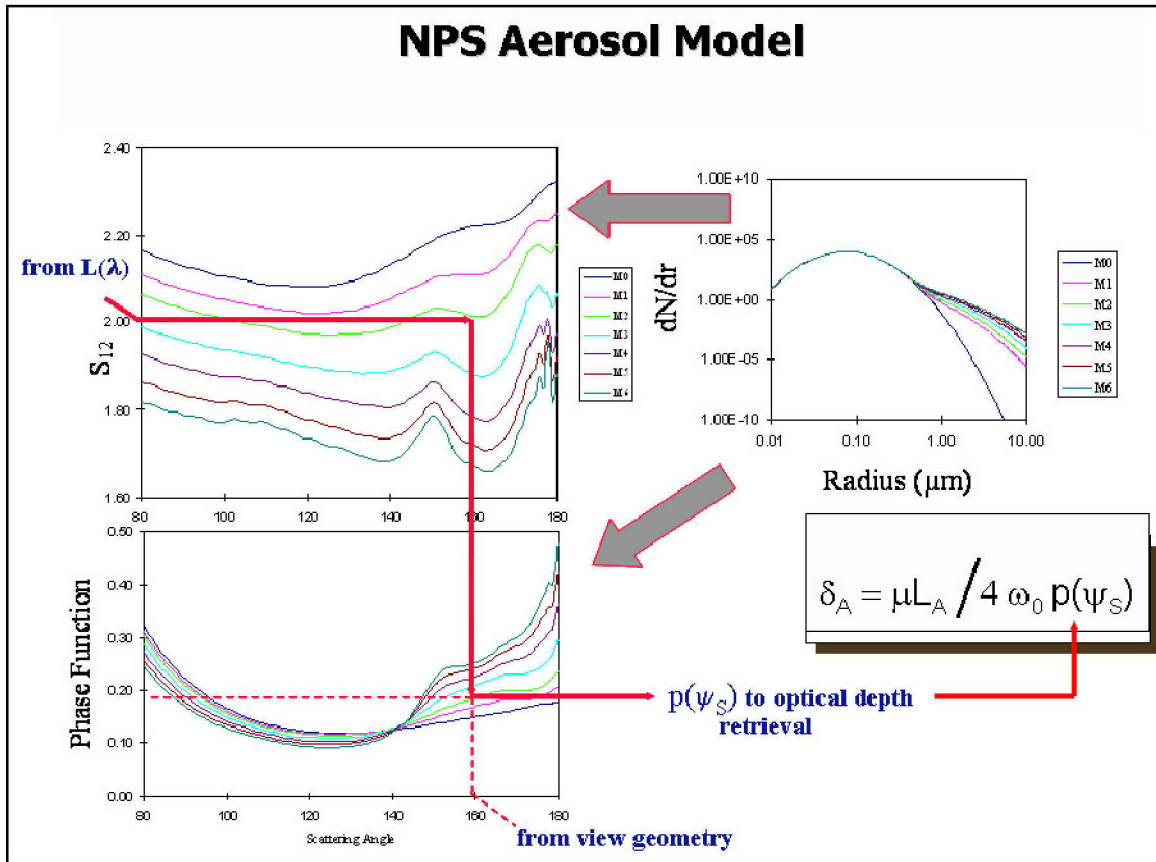
Figure 13.   NPS Aerosol Model
(from Durkee, 2004)

The NPS aerosol model starts with an assumed size and number distribution of the aerosol (Upper right of Figure 13). Based on that size and number distribution the ratio of the red to NIR aerosol radiances is determined. This is referred to as the S_{12} value. Based on the S_{12} value, the satellite angles and the solar angles, an aerosol model number is picked. Each aerosol model number has a predetermined phase function. The shape of the phase function is derived from the assumed aerosol size and number distribution.

In this thesis the calculated aerosol scattering phase function was retrieved by plotting the values of Equation (9) against its corresponding backscattering angle for the various satellite views of the aerosol region. A comparison of the calculated and model phase functions is done in the results section. The results section also contains the NPS model outputs for the 18 smoke aerosol and 15 dust aerosol cases.

THIS PAGE INTENTIONALLY LEFT BLANK

IV.   RESULTS

A.   SMOKE

A total of 18 smoke cases were observed. Each case had between four and seven satellite views over the aerosol region within a two to four hour time period. Each specific case can be seen in detail in Appendix A. The smoke cases were run on the NPS aerosol model and the S_{12} ratio computed. It was observed that the SeaWiFS sensor often produced the lowest S_{12} value (Figure 14). The tight grouping of the S_{12} values gives confidence in the multiple satellite technique. The tight grouping indicates that the satellites are viewing similar ratios of the red/NIR wavelengths. The tightest groupings occurred in cases 1-3 and 15-17, when the smoke optical depths were highest (Figures 15 and 16).
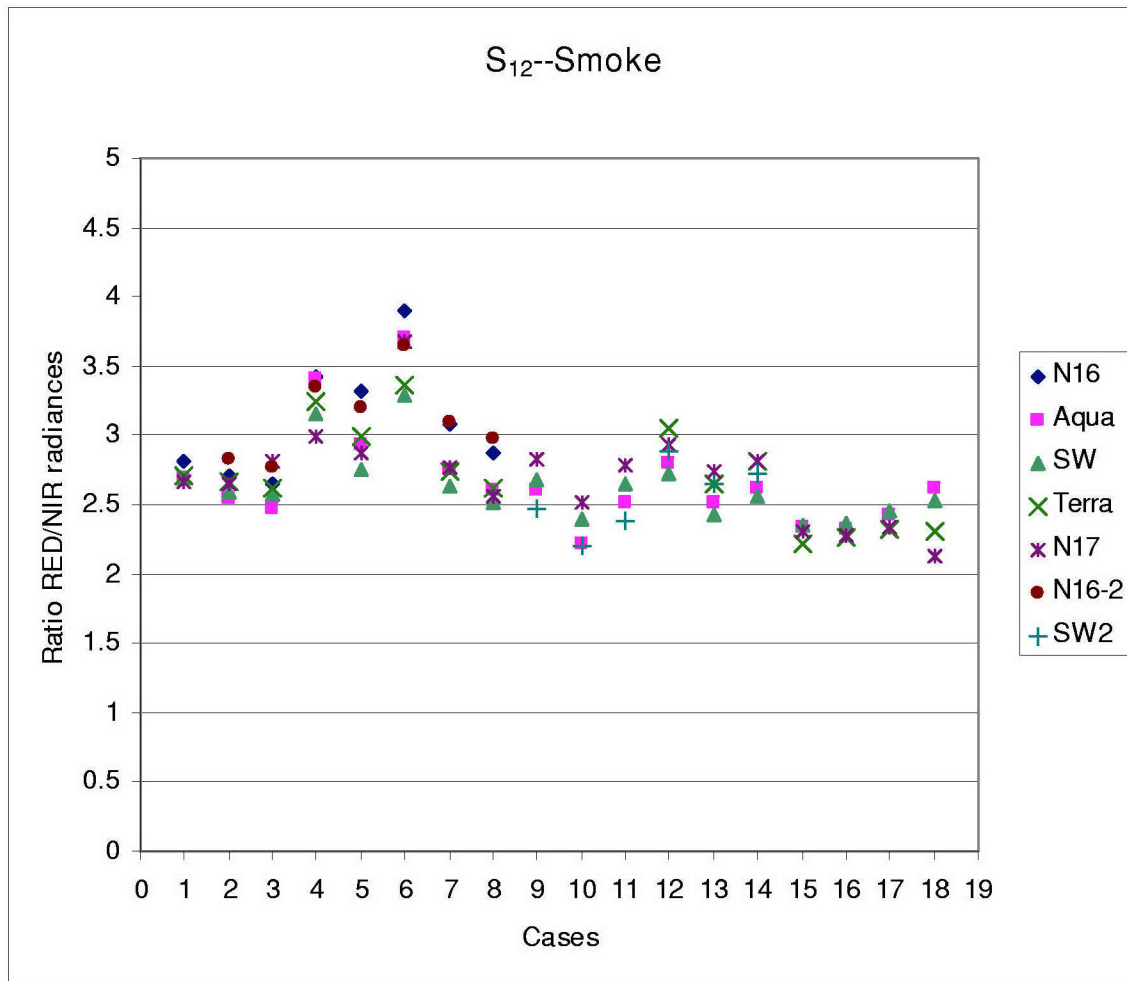
Figure 14. S_{12} Ratio for Smoke Cases

27
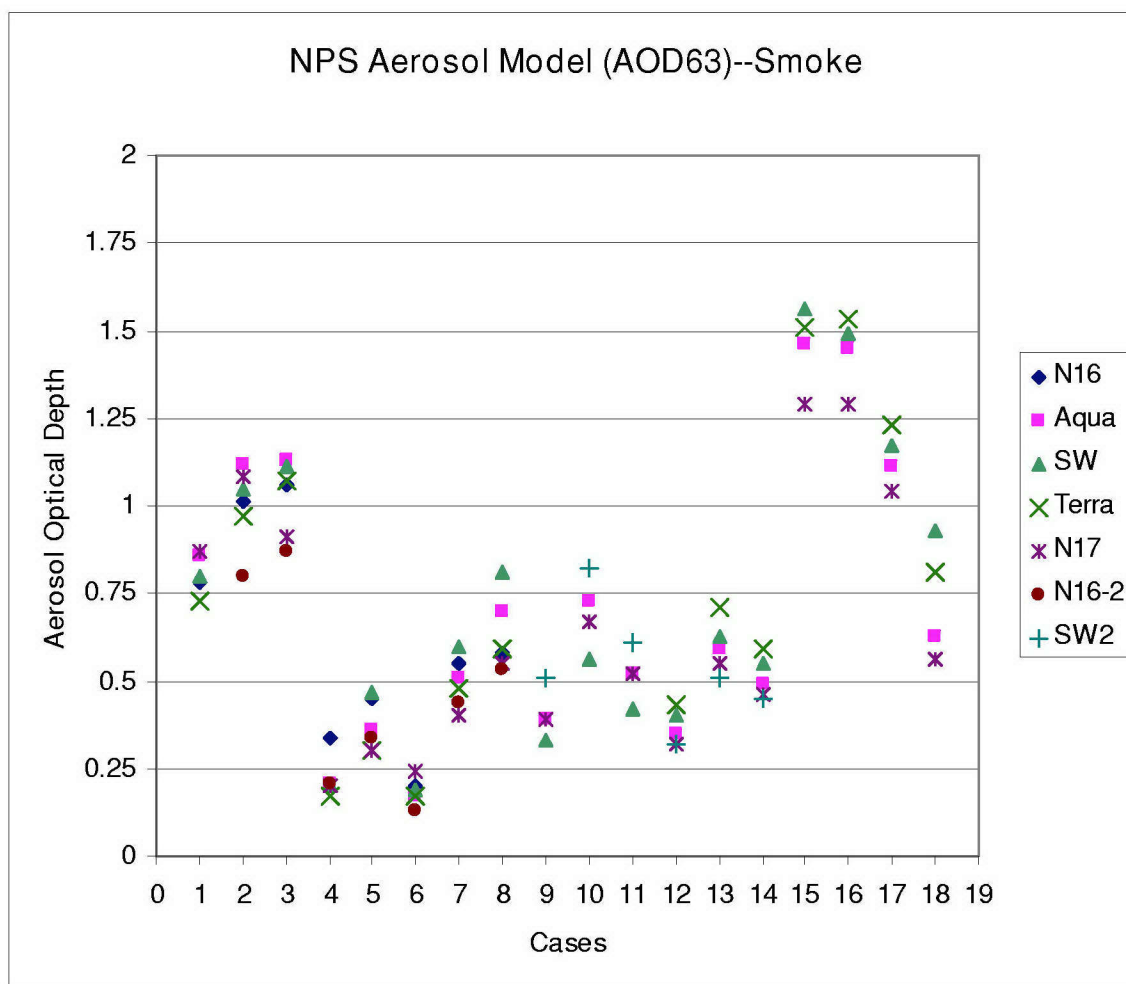
Figure 15.   NPS Aerosol Model Optical Depth (AOD63) for the Smoke Cases

The NPS aerosol model optical depth values for the red and NIR wavelengths are indicated in the AOD63 and AOD86 Figures 15 and 16 respectfully. The variability in the optical depth seen in Figure 15 is largest when the optical depth is higher. It is the most evident in the NIR wavelength (Figure 16) where the lower optical depths vary only slightly. The model optical depths are within the range of optical depth values observed, in a 24 hour period, by AERONET in-situ sensors.
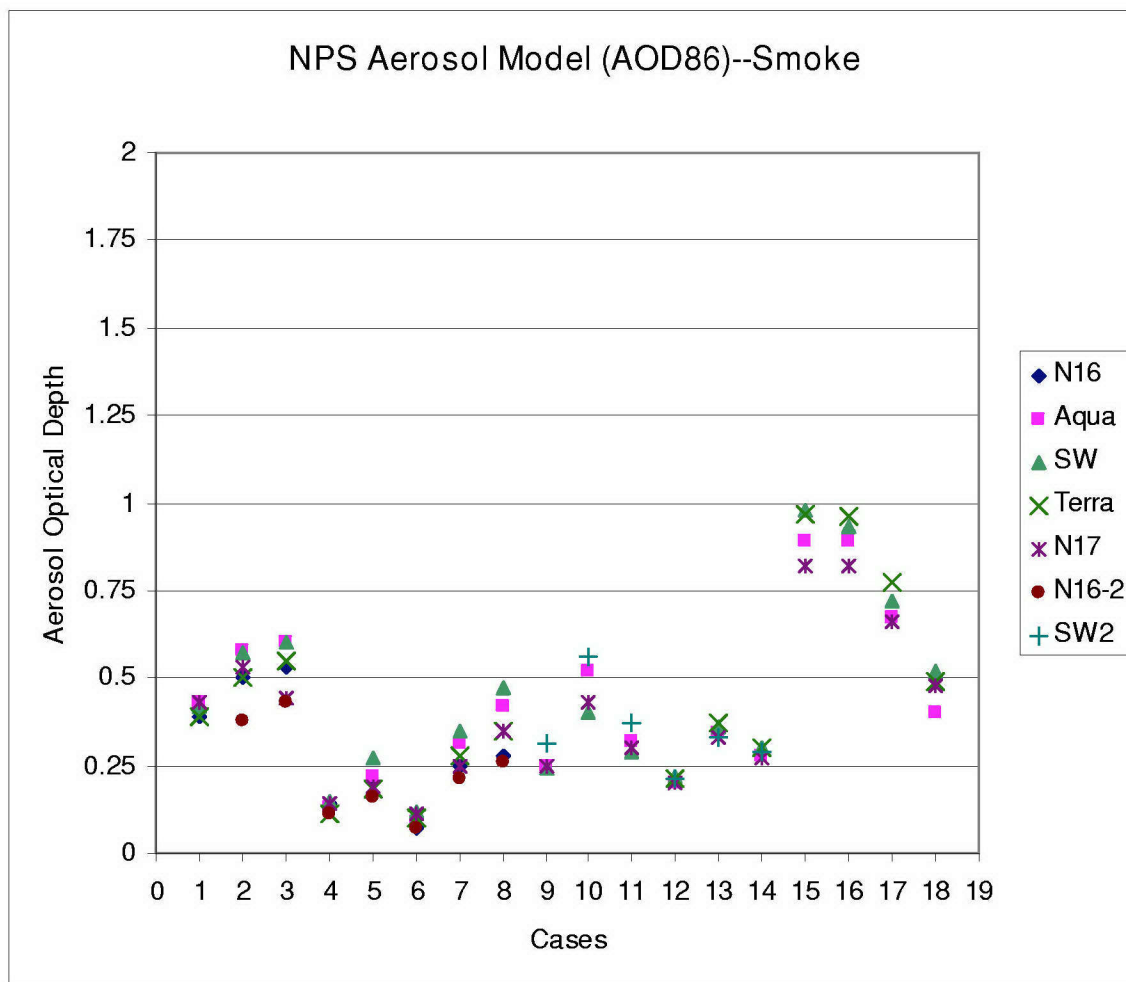
Figure 16.   NPS Aerosol Model Optical Depth (AOD86) for the Smoke Cases

The NPS aerosol model number is chosen based on what the model interprets the size of the aerosol particles to be. The smaller particles, like smoke, have a higher S_{12} value. A higher S_{12} value results in a higher model number. The NPS aerosol model most frequently picks model the highest model number, seven, for smoke cases. This is expected since model seven has the smallest particle size distribution. The model numbers shown in Figure 17 indicate that the model number from the SeaWiFS sensor is frequently lower than that of the other sensors. This could be an indication of a calibration issue for the SeaWiFS sensor.
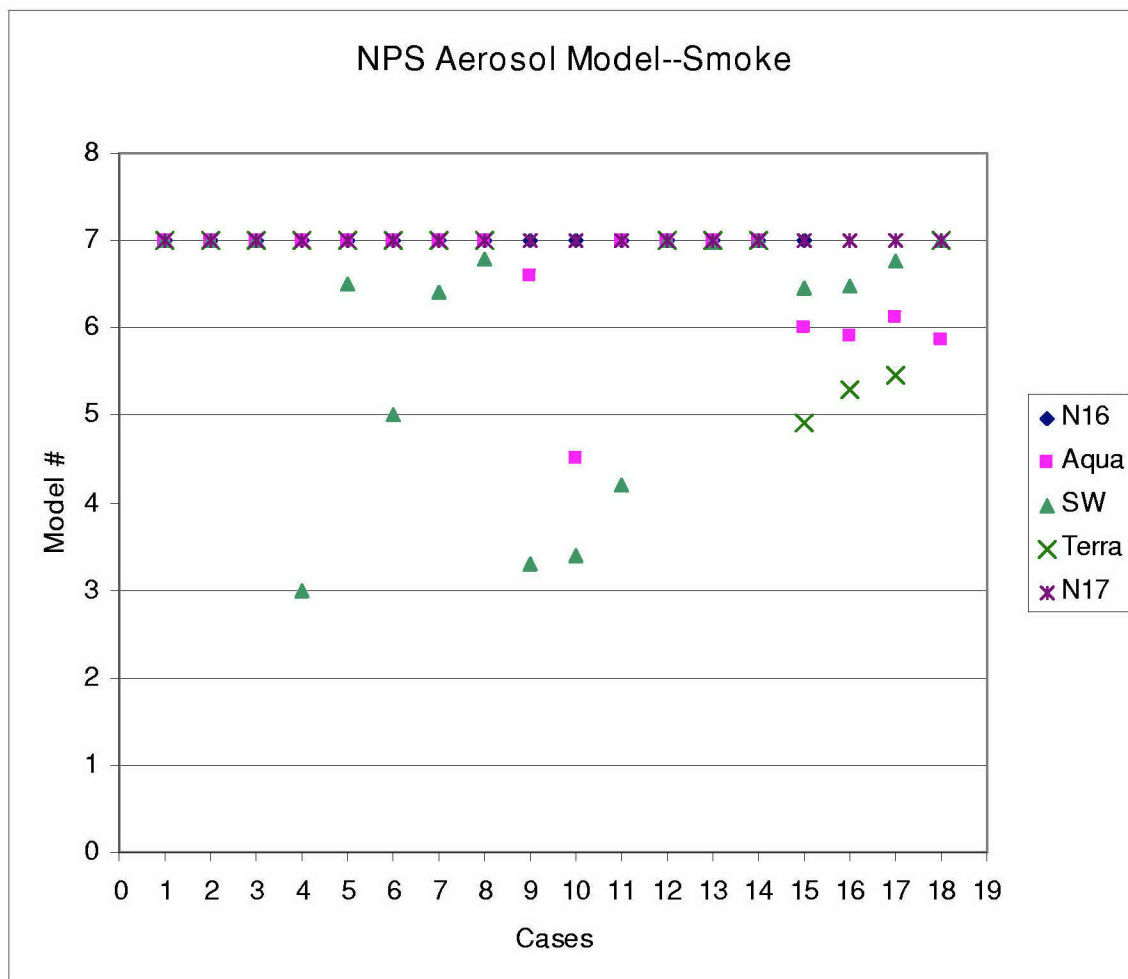
Figure 17.   NPS Aerosol Model Phase Function Pick for the 18 Smoke Cases

Figure 18 illustrates the retrieved phase function values from all satellites for the three smoke cases over Hudson Bay. It is apparent that the phase function is decreasing as the backscatter angle goes from 100°-140° and increasing for backscatter angles above 140°. As expected the calculated values for the phase function are higher than those of the model. The calculated values used total radiance instead of the aerosol radiance. Since the NPS model removes Rayleigh radiance and makes an ozone correction, its values are smaller. This difference is not important because the primary interest in this study is the comparison of the shape of the calculated vs. model phase functions. The phase functions vary somewhat in shape but trend toward increasing values after 140°. The comparative shape of the plotted phase function to that of the model leads to the conclusion that the actual size distribution of the aerosol particles is close to that indicated by the model. However, there are definitely some differences that indicate the actual size and number of aerosol particles are different from that of the model size and number distribution.
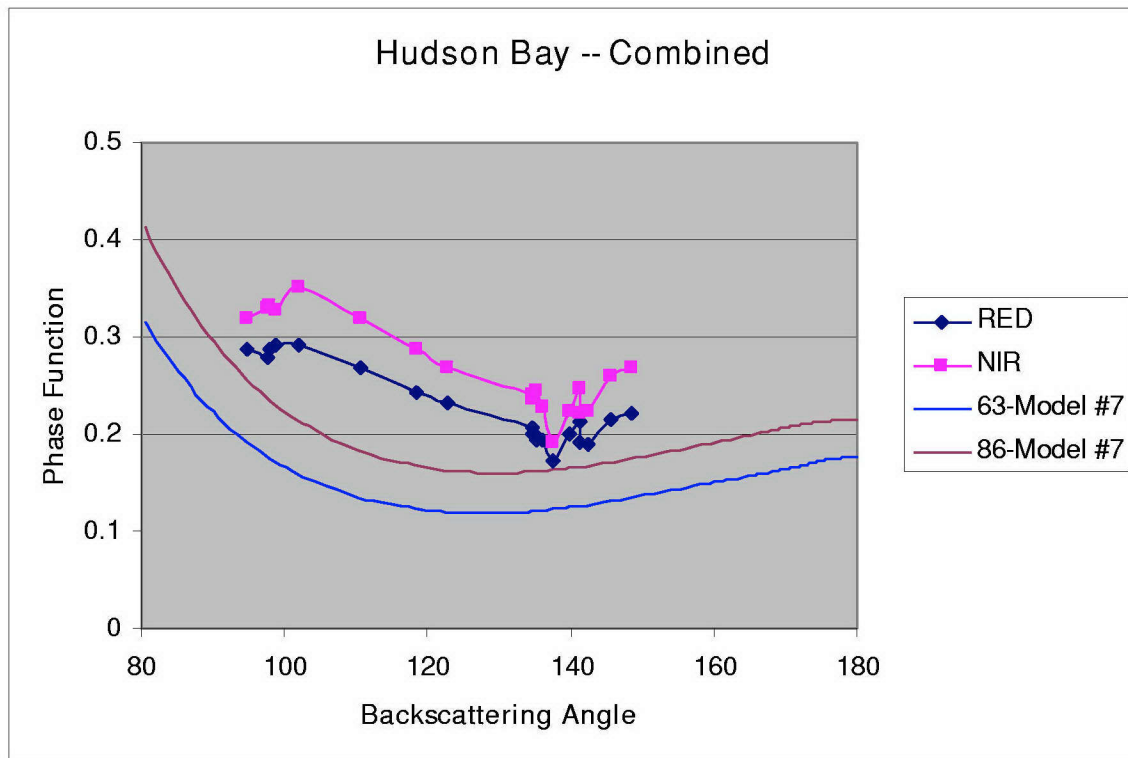
Figure 18.   Phase Function for Smoke Cases 1-3, over Hudson Bay, with NPS Aerosol Model #7 Phase Function

The retrieved phase functions for four smoke cases over the Black Sea are combined and displayed in Figure 19. Case 8 was not included in the combined phase function because it is believed the values were contaminated with either sunglint or shallow water color. For the remaining four cases the red and NIR wavelengths show a great deal of variability in the phase function plot. This variability could come from the fact that the samples for the four cases were taken a large distance from each other. The source regions for the smoke and the duration over water may account for a significant change in the shape of each individual phase function. This would account for a highly variable combined phase function. Each individual phase function can be seen in Appendix A. The combined phase function tends to be decreasing after 130°, while the model phase function is slowly increasing. This illustrates a difference between the actual and assumed aerosol size distribution.
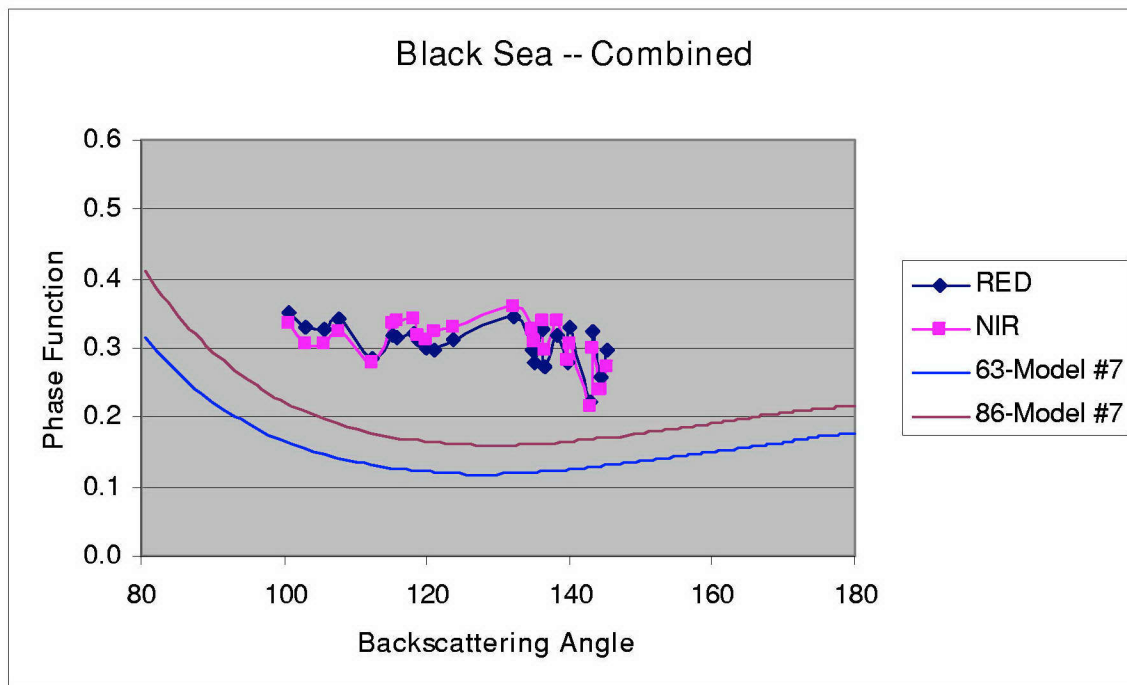
Figure 19.   Phase Function for Smoke Cases 4-7, over the Black Sea, with NPS Aerosol Model #7 Phase Function

Figure 20 shows the combined phase function retrieved for three smoke cases northwest of the United Kingdom over the North Atlantic. The general trend of the combined phase function is to decrease from 100°-120° and then nearly flat or slightly increasing above 120°. The points from each individual phase function fit together very well in the combined phase function to form a cohesive curve. This increases the confidence level that the phase function displayed is the true phase function and different from that of the model. It would be useful to have more data points at higher angles to see if the actual phase function continues to closely follow the shape of the model phase function. The smaller difference is the phase function from that of the model indicates that the actual aerosol size distribution is very close to that of the model. Note also that model five was selected as the mean model for this phase function and is plotted on Figure 20. This indicates the smoke particles have a size distribution with larger particles than in model seven.
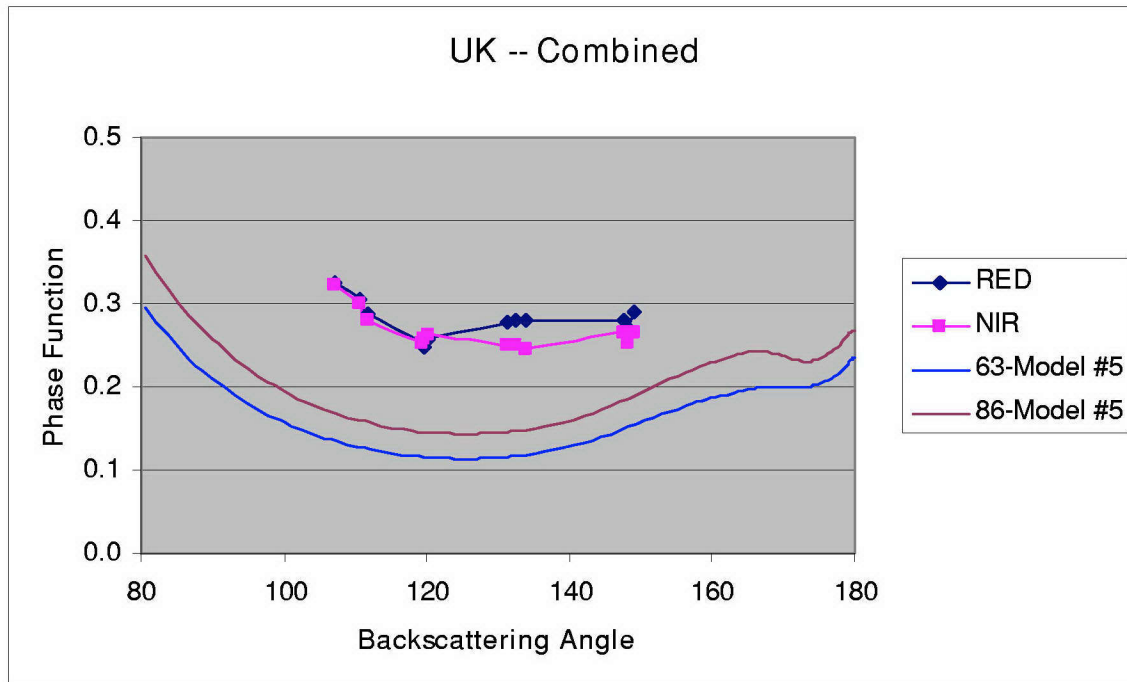
Figure 20.   Phase Function for Smoke Cases 9-11, northwest of the United Kingdom, with NPS Aerosol Model #5 Phase Function

Figure 21 shows the combined phase function retrieved for three smoke cases in a different area of the North Atlantic to the west of the United Kingdom. The general trend of the combined phase function is to decrease in value as the backscatter angle increases. There appears to be more irregularities in the phase function than in the previous United Kingdom case. The general shape of the phase function matches fairly well with the model phase function.
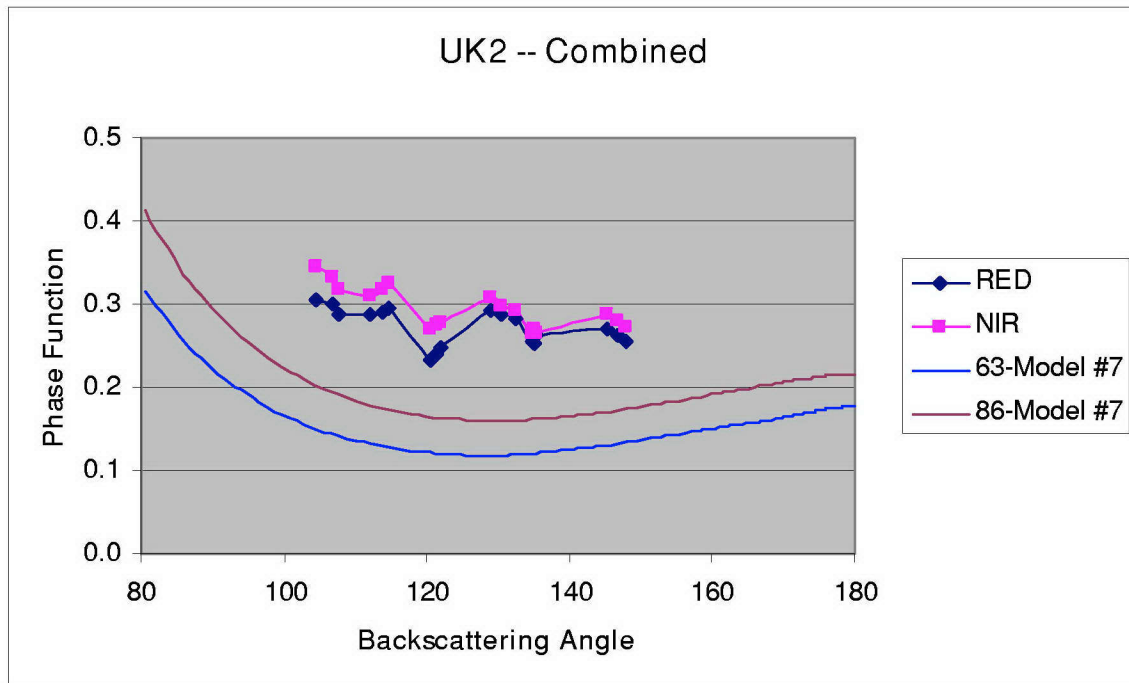
Figure 21.   Phase Function for Smoke Cases 12-14, west of the United Kingdom, with NPS Aerosol Model #7 Phase Function

Figure 22 illustrates the combined phase function retrieved from four smoke cases near mainland Japan. It depicts a very flat curve with only slightly increasing values at each end. This phase function had the largest optical depth values of all the smoke cases. It also had some of the highest backscattering angles. Model number six indicates that the smoke particles have a size distribution with larger particles than in model seven. The actual phase function is similar in shape to the model phase function. There are some inconsistencies in the values between the SeaWiFS and Terra satellites near the 150° angle. The three SeaWiFS values are quite a bit higher than the three Terra values in both the red and NIR phase functions. The relative high point near 135° is also a SeaWiFS data point. This also could be an indication of a SeaWiFS calibration issue. Figure 23 shows the same phase function without the SeaWiFS data. It is a much smoother curve that more closely matches the model phase function. .
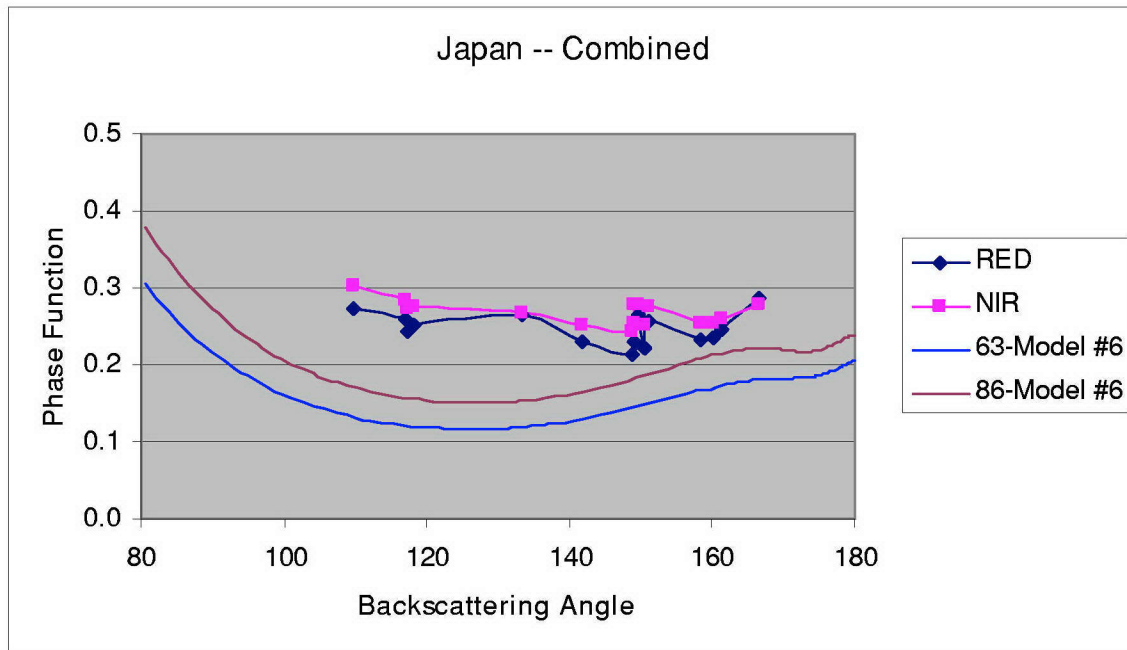
Figure 22.   Phase Function for Smoke Cases 15-18, near Mainland Japan, with NPS Aerosol Model #6 Phase Function
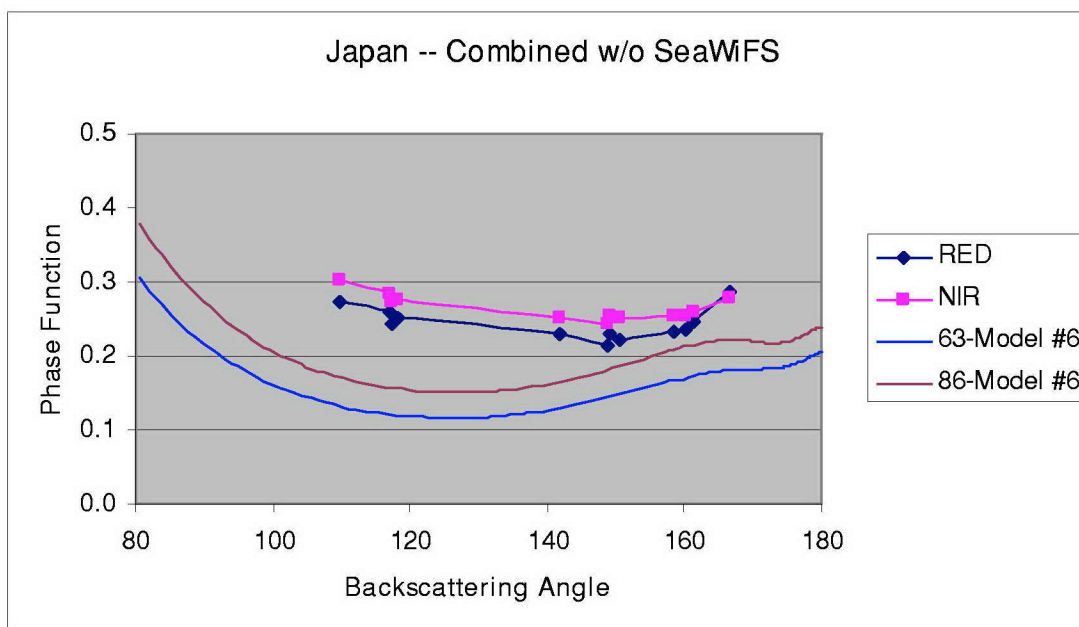
Figure 23.   Phase Function without SeaWiFS data, for Smoke Cases 15-18, near Mainland Japan, with NPS Aerosol Model #6 Phase Function

B.   DUST

A total of 15 dust cases were observed. Each case had four or five satellites over the aerosol within a two to four hour time period. Each specific case can be seen in detail in Appendix B. The dust cases were run on the NPS aerosol model and the S_{12} values are displayed in Figure 24. The tighter the grouping of the S_{12} values the greater the confidence in the multiple satellite technique. The tighter grouping indicates that the satellites are viewing similar ratios of the red/NIR wavelengths. All of the groupings had small variance among the values. Note that the NOAA-16 values were a little higher than the rest of the grouping in cases five through eight.

36
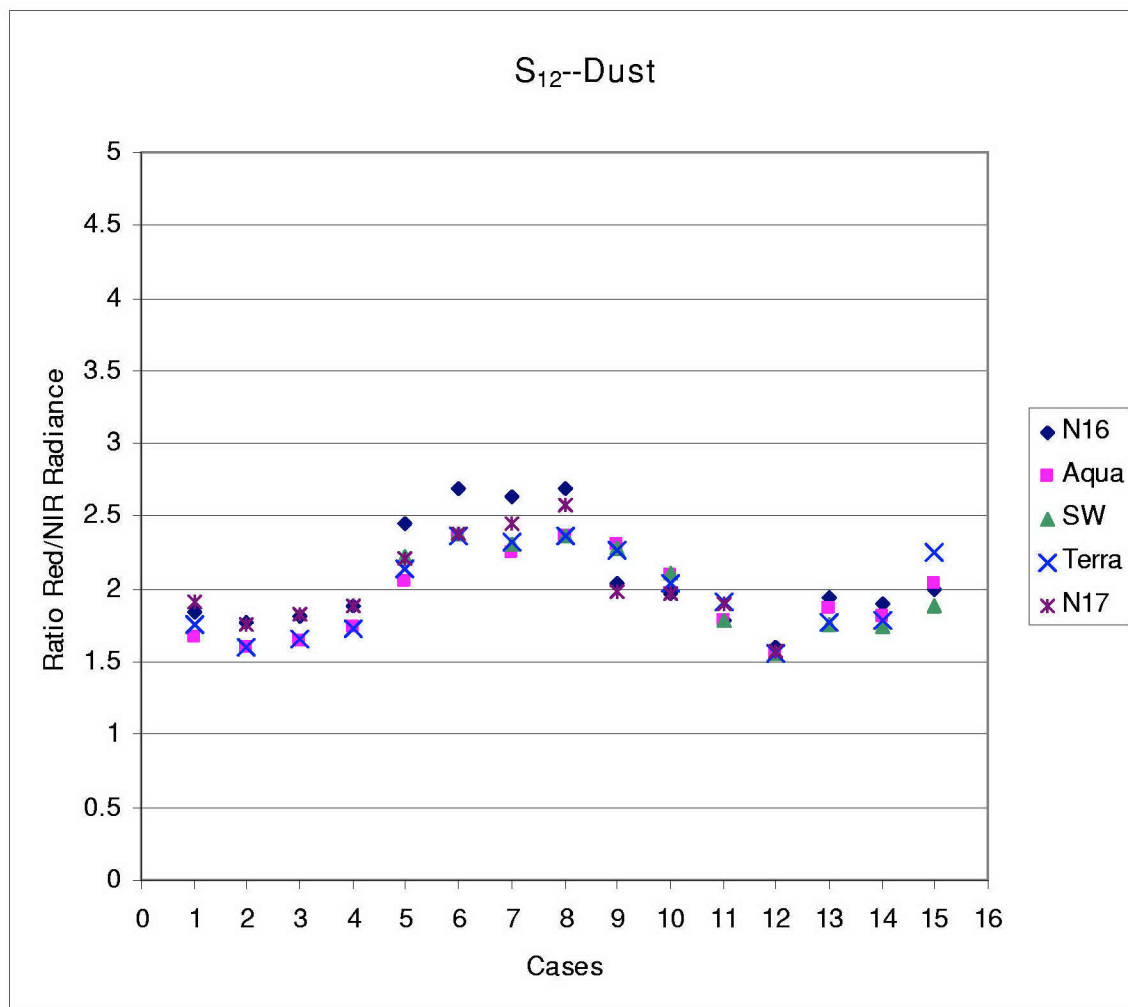
Figure 24. S_{12} Ratio for Dust Cases
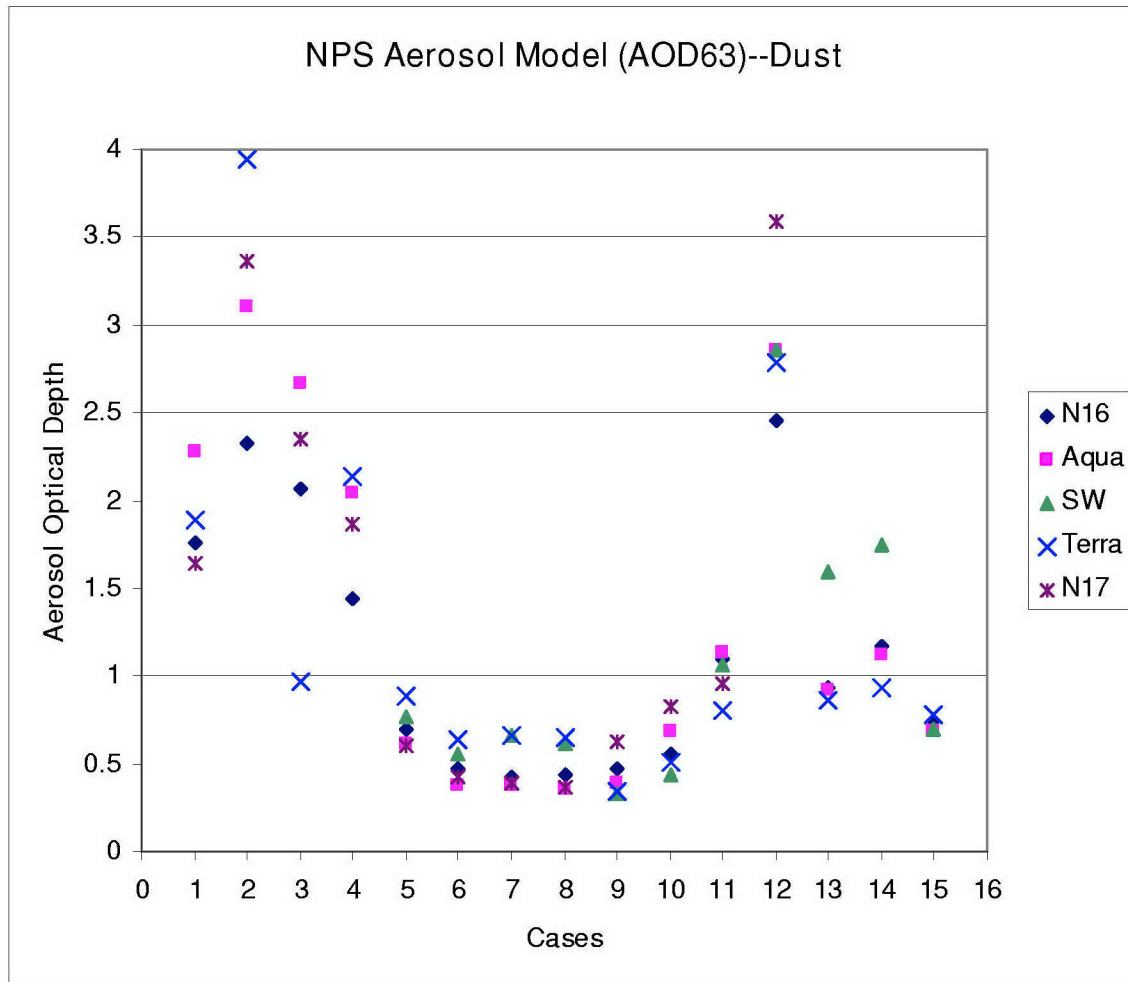
Figure 25.   NPS Aerosol Model Optical Depth (AOD63) for the Dust Cases

The aerosol optical depths shown in Figures 25 and 26 indicate a large variability in the values when the optical depths were large. The optical depth of an aerosol tends to change more rapidly when the values are high. The aerosol appears to be spreading out over the water and losing its constant large optical depth value. Another possible explanation is that the aerosol particles are undergoing hydration from being over the water for an extended period of time. In addition, it was harder to pinpoint and track a significant feature in the aerosol without its characteristics changing when the optical depths were very high.

None of the sensors seemed to have a bias relative to the other sensors. The highest optical depths in each case seemed to be distributed fairly evenly among the different sensors. This held true for the optical depths at both the red and NIR wavelengths.
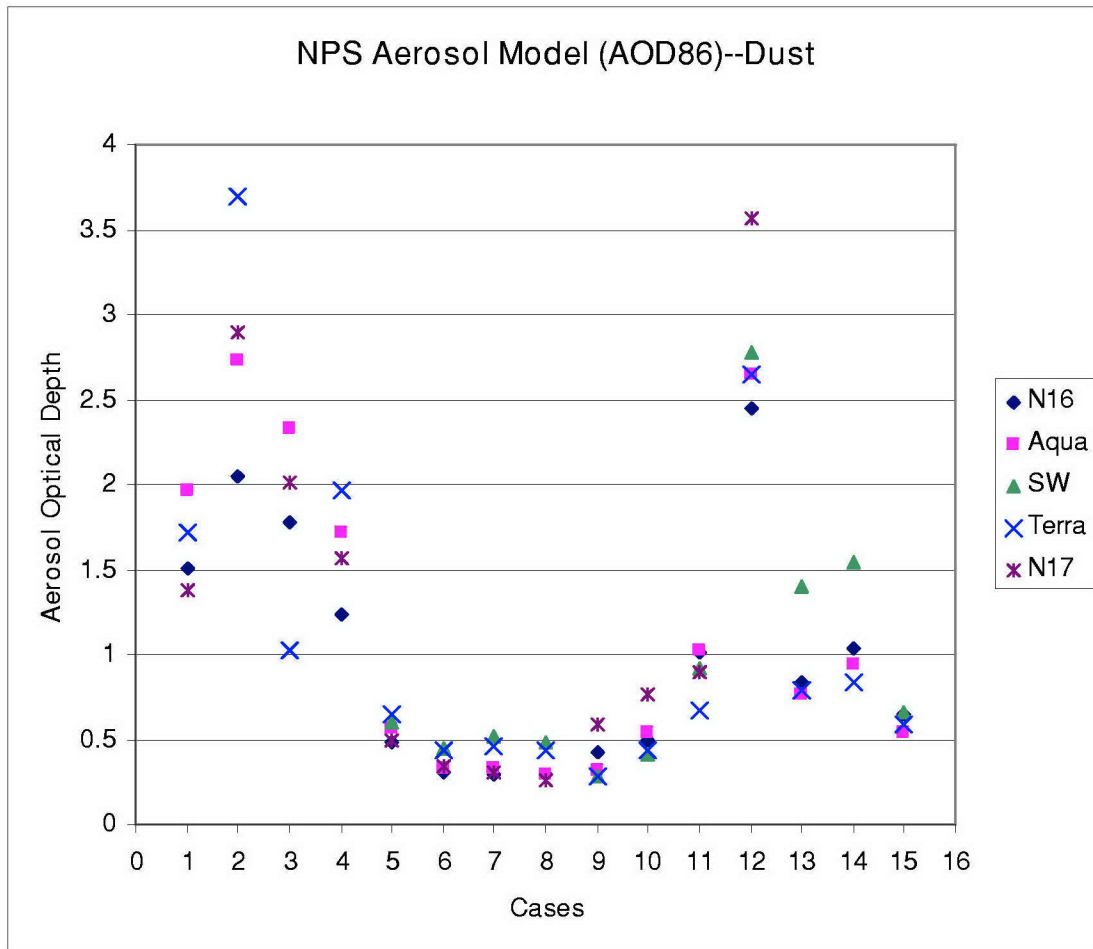
Figure 26.   NPS Aerosol Model Optical Depth (AOD86) for the Dust Cases

Figure 27 reveals a large variability in the model selection for cases five through eight. These are the dust cases where the optical depths were the lowest and the size distribution of the aerosol lies in the transition zone between models one and seven. The model selection for NOAA-16 is the highest for these cases as well as cases 13 and 14. The typical model selection for the dust cases was model one. This is expected since model number one has the largest particle sizes in its distribution. As seen in the smoke cases, when there was disagreement in the model selections, the SeaWiFS sensor had the lowest model value.
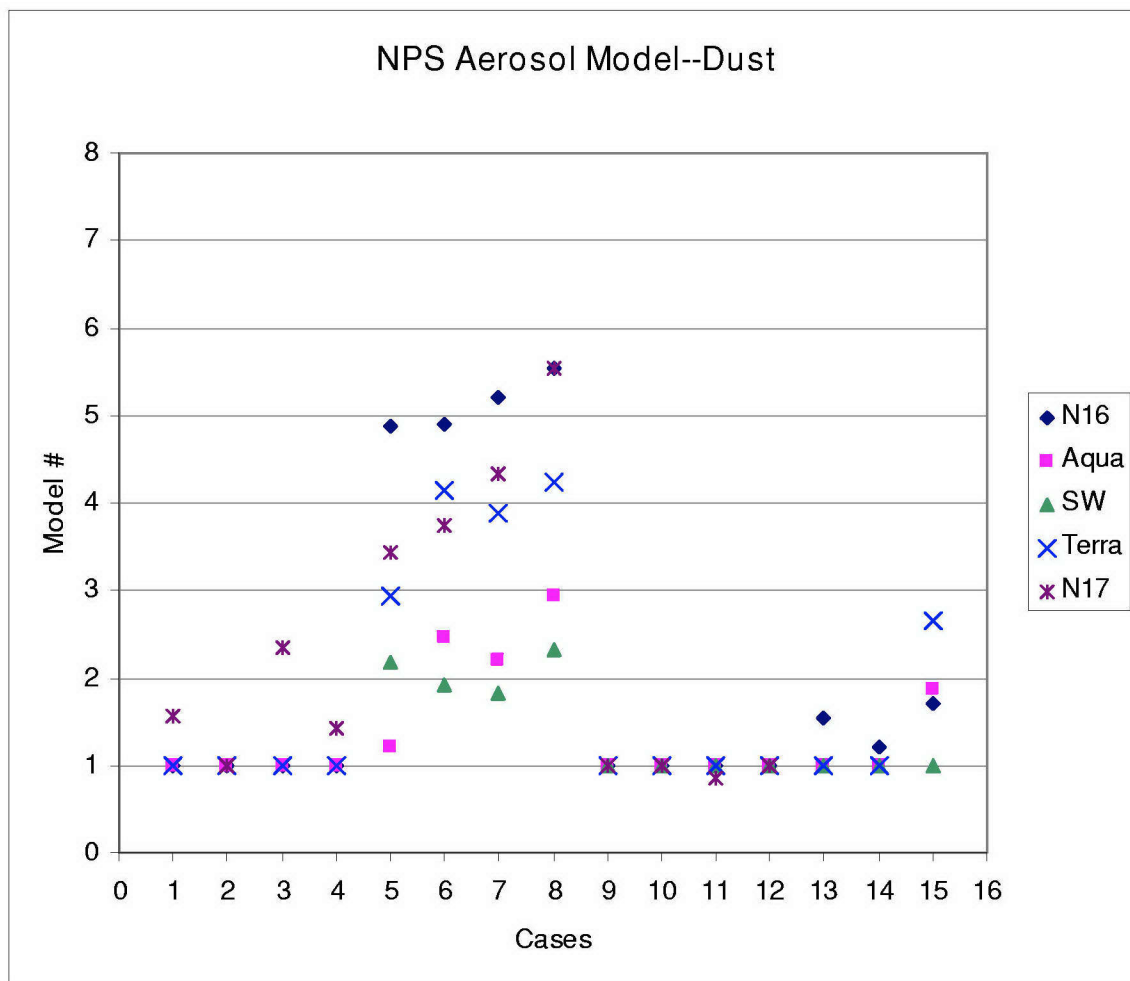
Figure 27.   NPS Aerosol Model Phase Function Pick for the 15 Dust Cases

Displayed in Figure 28 is the combined phase function retrieved for the four dust cases over the Straight of Hormuz near the Persian Gulf. The general trend of the phase function is to be relatively flat with a sharp rise after 140°. The increase in value after 140° is representative of what is seen in the model phase function. There are some differences between the shape of the actual and model phase function. This indicates that there are some differences between the actual aerosol size distribution and the size distribution in the model.
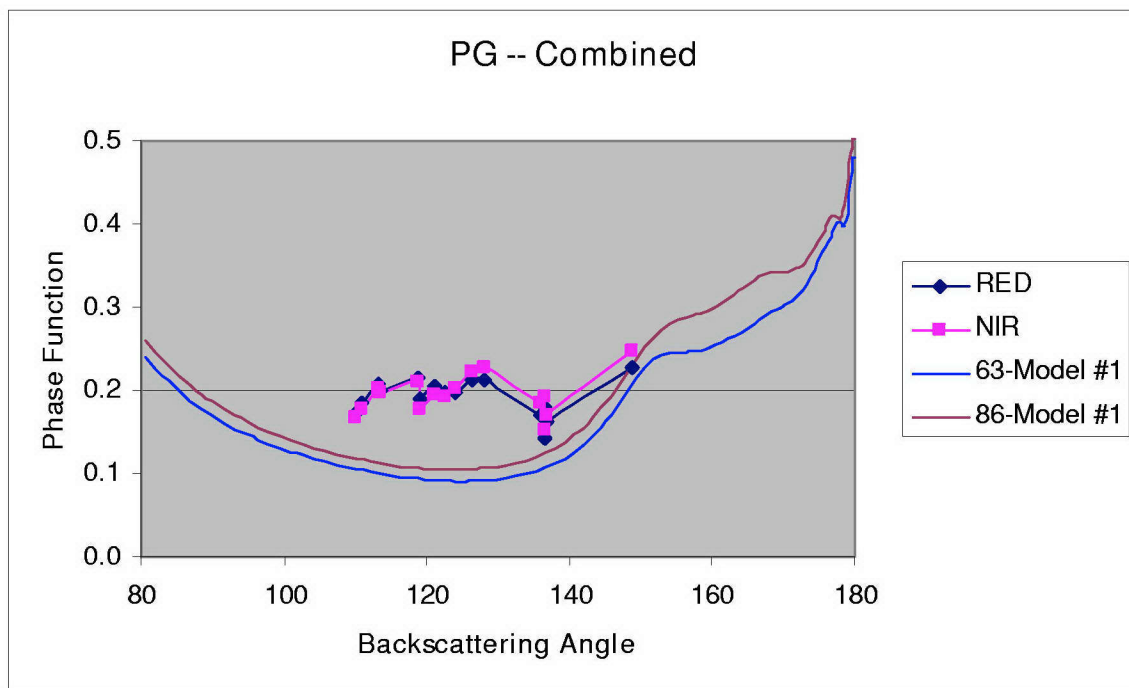
Figure 28. Phase Function for Dust Cases 1-4, near the Persian Gulf, with NPS Aerosol Model #1 Phase Function

Figure 29 shows the combined phase function retrieved for four dust cases off the southern coast of Pakistan. The combined phase function plot for the red and NIR wavelengths is very irregular and does not follow a smooth curve. The optical depths for these dust cases were relatively low. These were the cases where the NPS aerosol model had a difficult time also in determining an aerosol model number. The model number selected varied greatly with each satellite within each individual case (Figure 27). It is probable that this environment is changing over the four hour time period during the satellite passes. With the low optical depth values a small change in aerosol properties can quickly lead to a relatively large change in the model number selected. The individual cases that make up this phase function do not follow a smooth curve. Thus, when the four individual cases were combined the result is an exceptionally coarse graph. The individual cases can be seen in Appendix B. Of note is that model number three was the mean model selected for these cases. This indicates that the actual particles are smaller in size than in the other dust cases.
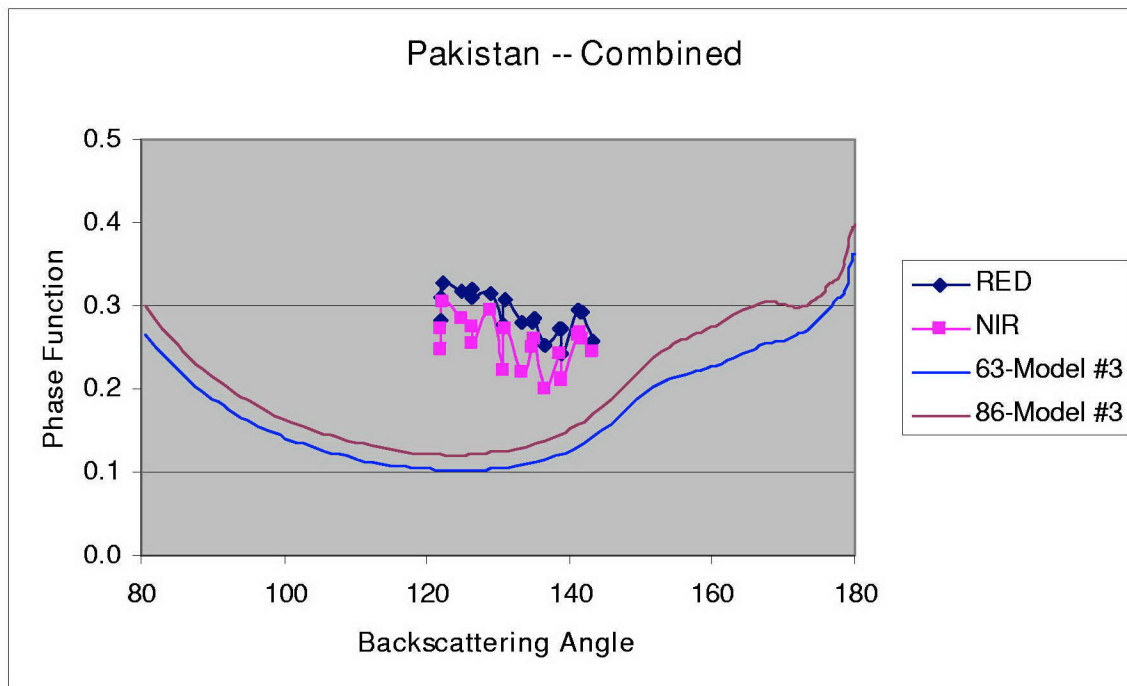
Figure 29. Phase Function for Dust Cases 5-8, near Pakistan, with NPS Aerosol Model #3 Phase Function

Figure 30 shows the combined phase function retrieval for four dust cases off the coast of Libya. This graph had some unexpected features. Some of the values seemed extremely high while others appeared low. The four points that create a ridge in the graph near 120° all came from the AVHRR sensor on NOAA-17. It is possible that these data values were contaminated by sunglint, causing an unusually high value. Sunglint could not be ruled out based on the geometry between the satellite zenith, solar zenith, and their relative azimuth. The visible indication of the sunglint could be masked by the heavy dust over the water. It could also be that the optical depth was not remaining constant from one satellite pass to the next. This would also account for the significant amount of fluctuation in the curve above 140°.
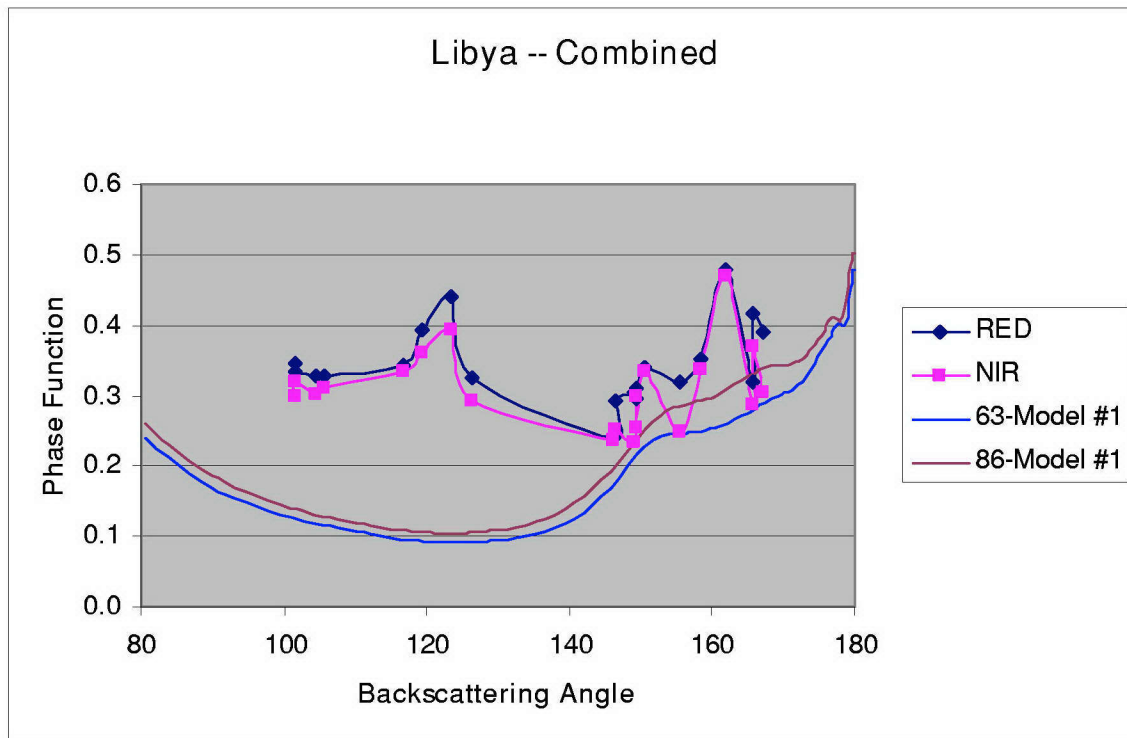
Figure 30.   Phase Function for Dust Cases 9-12, near Libya, with NPS Aerosol Model #1 Phase Function

43

Figure 31 shows the combined phase function retrieved for three dust cases over the Red Sea. The function is fairly flat until about 160° then the values have a significant jump for the last three points. From looking at the model phase function we would expect a rapid increase in the actual phase function after 140°. There are some definite inconsistencies in the shape of the actual phase function compared to the model phase function. This is most likely due to differences in the aerosol size distribution from the model size distribution. The individual phase functions for this case as well as the thirteen other dust cases can be seen in Appendix B.
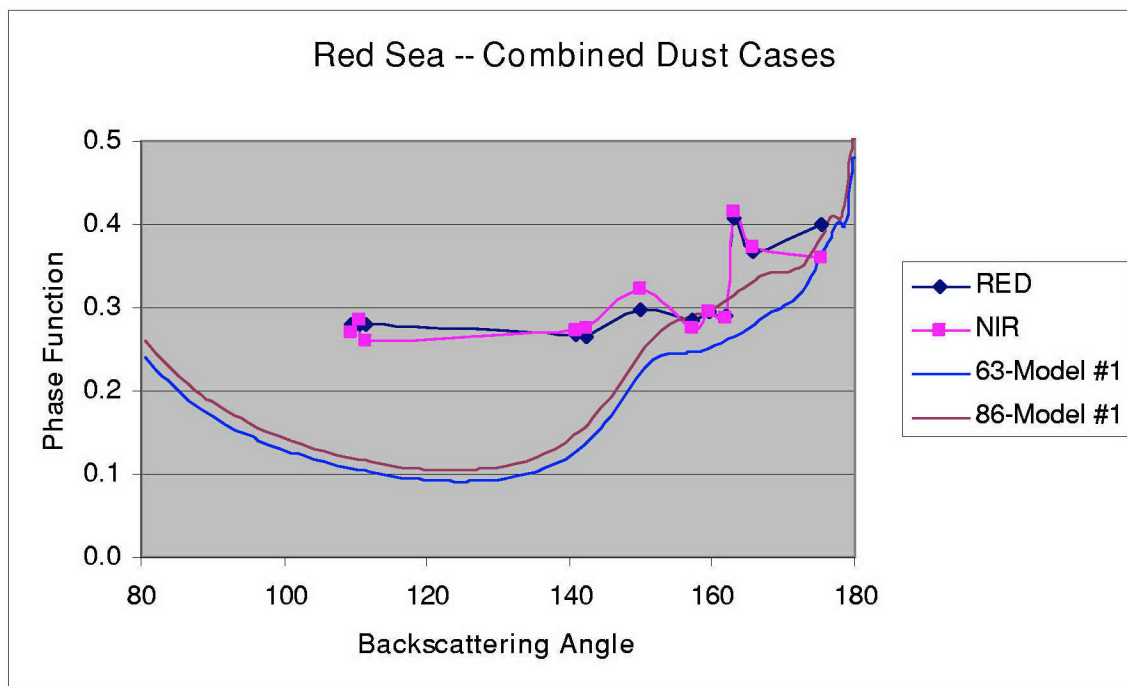
Figure 31.   Phase Function of Dust Cases 13-15, over the Red Sea, with NPS Aerosol Model #1 Phase Function

V. CONCLUSIONS AND RECOMMENDATIONS

A. CONCLUSIONS

The retrieval of an aerosol scattering phase function from multiple polar orbiting satellites proved to be a difficult but attainable task. A total of 33 phase functions were derived, 18 of which had smoke aerosol and the remaining 15 were for dust aerosol. Each of the cases was viewed by four to nine satellite passes within a two to four hour time frame. The red and NIR radiance values were used along with the aerosol backscattering angles to determine the phase function.

The optical depths necessary for plotting the phase functions were primarily retrieved from the NPS aerosol model. The optical depths from the model grouped nicely within each case study. The greatest variability among the satellites occurred when the optical depths were the largest. The S_{12} ratios also grouped together well within each of the smoke and dust cases. The smaller aerosols, like smoke, had a larger S_{12} ratio than the dust particles. The higher S_{12} ratio led to a higher model selection for the smoke cases. The model selected most often was seven for the smoke cases and one for the dust cases.

The phase function from the NPS model selected was compared to the phase function retrieved from the multiple satellite technique. Having a similar phase function to that of the model indicates the size distribution used in the model is similar to that of the actual aerosol. When the phase functions were different than that of the model it indicated the aerosol size distribution was different than that of the model or that the aerosol was not maintaining constant properties between each satellite pass. The phase functions from the smoke cases tended to match the model phase functions more closely than the dust cases. Although the phase functions for the smoke cases were similar to those of the model, they were not identical. This suggests that the actual aerosol size distribution is close but not identical to the model size distribution.

45

The phase functions for the dust cases did not match the model phase functions very well. Some of the phase functions appeared very irregular and did not follow a smooth curve; this implies a rapidly changing aerosol. The aerosol did not maintain consistent properties between each satellite pass. Its optical depth was most likely changing due to a spreading out of the aerosol or the hydration of the aerosol particles. The Pakistan and Libya cases had the most irregularities, while the Persian Gulf and Red Sea cases had the least.

Finally, there seems to be some inconsistencies with the SeaWiFS sensor. There is possibly a calibration issue similar to that of the AVHRR sensor on board the NOAA satellites. Further examination is required to conclusively determine if a problem exists.

B.   RECOMMENDATIONS

There are several follow-on recommendations that would enhance the value of this study. Now that a representative phase function of the actual aerosol has been retrieved, the next logical step would be to determine the aerosol size and number distribution necessary to produce that phase function. With a more accurate picture of the aerosol size distribution and composition a more complete awareness of the battlespace will exist. With that knowledge comes a better understanding of what the impacts will be to the warfighter.

Another recommendation is to measure aerosols that are not as concentrated and interrogate areas that have low optical depths. Thin dust and smoke cases may behave quite differently than the thick cases examined here. Diverse areas of the world have very different aerosol issues. The yellow wind from the Loess Plateau and the Brown Wind from China are several worthy of study. Determining the phase function of the background environment with no aerosol would also prove useful.

In the future the number of satellites in orbit will increase and the quality of sensors onboard will improve. With the introduction of systems like the National Polar-orbiting Operational Environmental Satellite System (NPOESS) the number of data points in each phase function can be increased. The more precise the phase function retrieval the more exact the information will be about that aerosol.

THIS PAGE INTENTIONALLY LEFT BLANK

APPENDIX A. GRAPHS OF INDIVIDUAL SMOKE CASES

A. HUDSON BAY SMOKE CASES
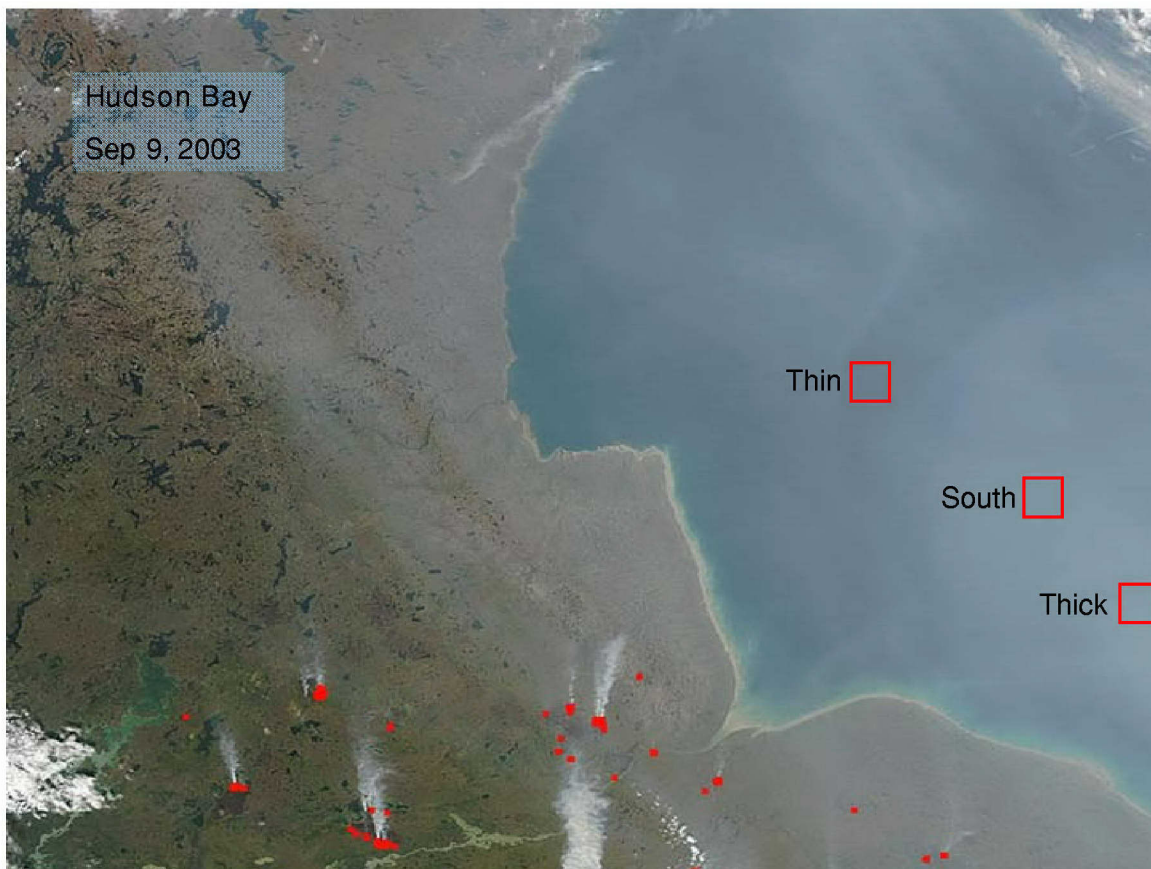
Figure 32.   Three smoke cases over Hudson Bay
(from NASA GSFC, 2005b)

Avg Optical Depth	Eo	K	Red Phase	NIR Phase	Linear Extrap times Cos(Sat Z) sorted by angle				
0.8033	1644	0.009515	0.0000	0.0000	90.00	1636 N15	0.00	0.00	0.00
0.405	1034	0.030008	0.0000	0.0000	90.00	1111 N16	0.00	0.00	0.00
			0.0000	0.0000	90.00	506 N15	0.00	0.00	0.00
			0.2867	0.3323	98.04	1045 A1	30.13	11.08	44.69
			0.2311	0.2685	122.77	1035 T1	24.29	8.95	39.15
			0.2062	0.2413	134.63	1220 A1	21.67	8.04	35.19
			0.1999	0.2365	134.67	911 N17	21.01	7.88	0.00
			0.1992	0.2233	139.92	1252 N16	20.93	7.44	0.00
			0.2119	0.2475	141.20	1154 SW	22.27	8.25	35.76

Smoke Case 1

AOD 63	AOD 86
0.78	0.39
0.86	0.43
0.8	0.42
0.78	0.37
0.73	0.39
0.87	0.43
0.80333	0.405
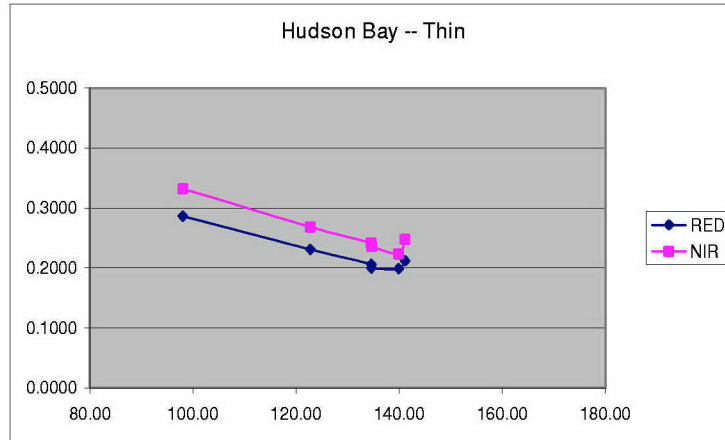
Figure 33.   Smoke case 1 over Hudson Bay

Avg Optical Depth	Eo	K	Red Phase	NIR Phase	Linear Extrap times Cos(Sat Z) sorted by angle				
0.9943	1644	0.007687597	0.0799	0.1161	88.37	1636 N15	10.39	4.80	0.00
0.5029	1034	0.024166162	0.2862	0.3185	94.84	1111 N16	37.23	13.18	0.00
			0.2780	0.3308	97.60	1045 A1	36.16	13.69	52.10
			0.2431	0.2873	118.48	1035 T1	31.62	11.89	48.94
			0.1981	0.2453	135.25	1220 A1	25.76	10.15	39.95
			0.1928	0.2286	136.00	911 N17	25.08	9.46	0.00
			0.1907	0.2218	141.27	1252 N16	24.80	9.18	0.00
			0.2150	0.2605	145.60	1154 SW	27.96	10.78	42.93
			0.0607	0.0835	162.61	506 N15	7.90	3.46	0.00

Smoke Case 2

AOD 63	AOD 86
1.01	0.5
1.12	0.58
1.05	0.57
0.8	0.38
0.93	0.46
0.97	0.5
1.08	0.53
0.99429	0.502857
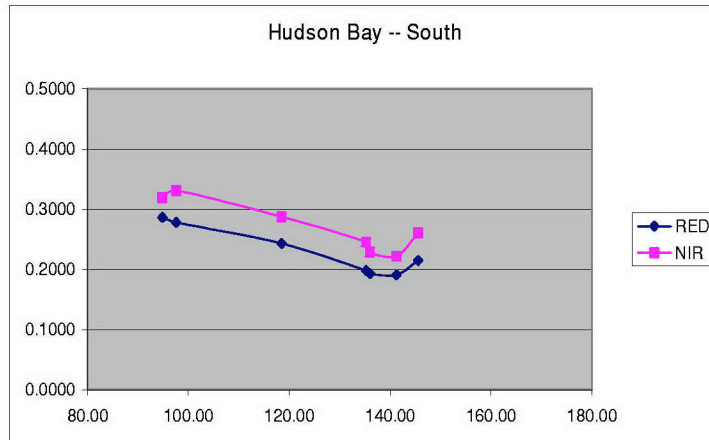
Figure 34.   Smoke case 2 over Hudson Bay

Avg Optical Depth	Eo	K	Red Phase	NIR Phase	Linear Extrap times Cos(sat Z) sorted by angle					
1.0314	1644	0.00741107	0.0491	0.0705	97.13	1636	N15	6.62	3.06	0.00
0.5271	1034	0.023056655	0.2881	0.3242	98.70	1111	N16	38.88	14.06	0.00
			0.2889	0.3461	101.86	1045	A1	38.98	15.01	55.87
			0.2651	0.3149	110.53	1035	T1	35.77	13.66	53.29
			0.1906	0.2404	135.31	1220	A1	25.72	10.43	39.04
			0.1702	0.1884	137.65	911	N17	22.96	8.17	0.00
			0.1880	0.2211	142.31	1252	N16	25.37	9.59	0.00
			0.2183	0.2644	148.43	1154	SW	29.46	11.47	44.62
			0.0734	0.0879	158.14	506	N15	9.90	3.81	0.00

Smoke Case 3

AOD 63	AOD 86
1.06	0.53
1.13	0.6
1.11	0.6
0.87	0.43
1.07	0.54
1.07	0.55
0.91	0.44
1.03143	0.527143
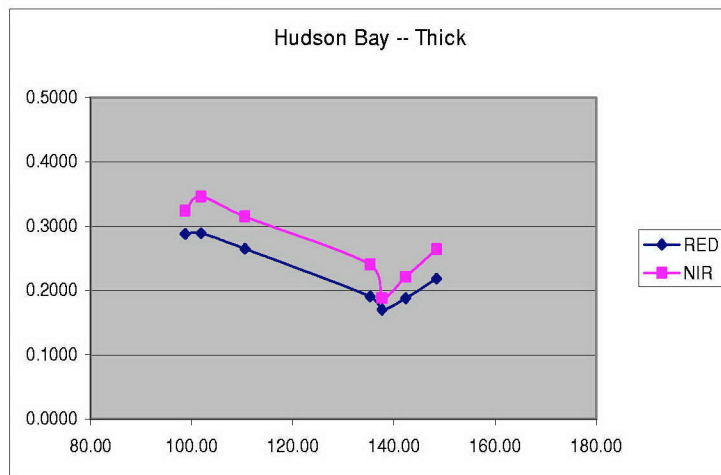
Figure 35.   Smoke case 3 over Hudson Bay

B.   BLACK SEA SMOKE CASES
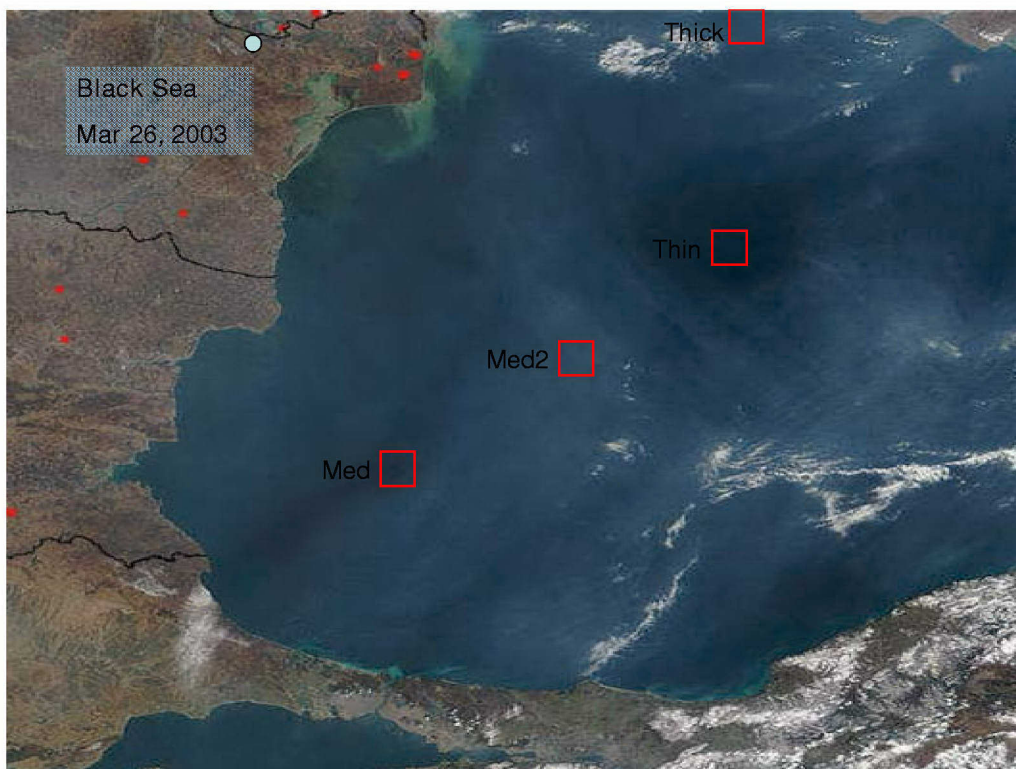
Figure 36.   Four smoke cases over the Black Sea, the fifth case was north of image (from NASA GSFC, 2005b)

Avg Optical Depth	Eo	K	Red Phase	NIR Phase	Linear Extrap times Cos(Sat Z) sorted by angle					
0.2217	1644	0.034478	0.0000	0.0000	90.00		N15	0.00	0.00	0.00
0.13	1034	0.093486	0.0000	0.0000	90.00		N15	0.00	0.00	0.00
			0.4610	0.3739	107.76	0243	N16	13.37	4.00	0.00
			0.3843	0.3210	112.39	0120	T1	11.15	3.43	21.03
			0.4341	0.3936	118.05	0056	N17	12.59	4.21	0.00
			0.3788	0.3258	139.91		SW	10.99	3.49	22.05
			0.4462	0.3544	139.98	0255	A1	12.94	3.79	25.13
			0.4375	0.3459	143.32	0425	N16	12.69	3.70	0.00
			0.0000	0.0000	180.00		A1	0.00	0.00	0.00

Smoke Case 4

AOD 63	AOD 86
0.34	0.14
0.2	0.15
0.21	0.11
0.21	0.13
0.17	0.11
0.2	0.14
0.22167	0.13
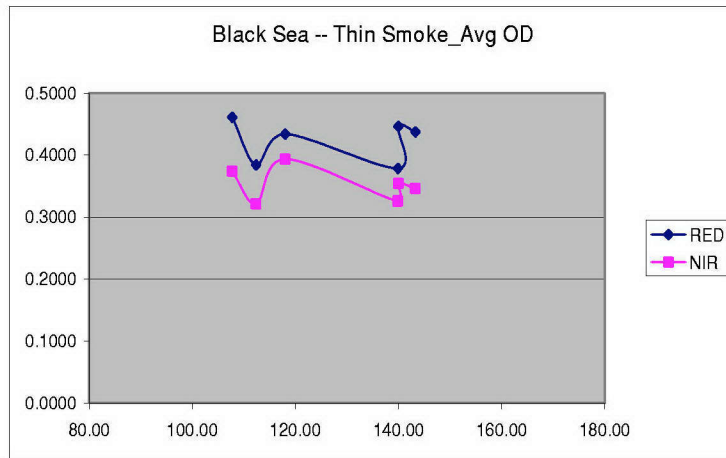
Figure 37.   Smoke case 4 over the Black Sea

Avg Optical Depth	Eo	K	Red Phase	NIR Phase	Linear Extrap times Cos(Sat Z) sorted by angle					
0.37	1644	0.020659	0.0000	0.0000	90.00		N15	0.00	0.00	0.00
0.2033	1034	0.059779	0.0000	0.0000	90.00		N15	0.00	0.00	0.00
			0.3699	0.3352	100.64	0243	N16	17.91	5.61	0.00
			0.3278	0.3179	118.66	0120	T1	15.87	5.32	27.63
			0.3281	0.3300	123.60	0056	N17	15.88	5.52	0.00
			0.3640	0.3597	132.14	0255	A1	17.62	6.02	30.72
			0.3123	0.3274	134.68		SW	15.12	5.48	26.84
			0.3125	0.2729	145.19	0425	N16	15.13	4.57	0.00
			0.0000	0.0000	180.00		A1	0.00	0.00	0.00

Smoke Case 5

AOD 63	AOD 86
0.45	0.2
0.47	0.27
0.34	0.16
0.36	0.22
0.3	0.18
0.3	0.19
0.37	0.20333333
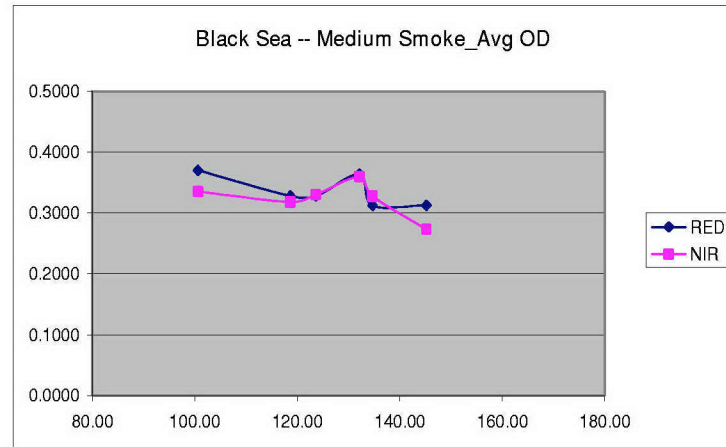
Figure 38.   Smoke case 5 over the Black Sea

Avg Optical Depth	Eo	K	Red Phase	NIR Phase	Linear Extrap times Cos(Sat Z) sorted by angle					
0.4967	1644	0.015389	0.0000	0.0000	90.00		N15	0.00	0.00	0.00
0.275	1034	0.044193	0.0000	0.0000	90.00		N15	0.00	0.00	0.00
			0.3302	0.3062	102.90	0243	N16	21.45	6.93	0.00
			0.3186	0.3347	115.31	0120	T1	20.70	7.57	33.52
			0.3015	0.3129	120.07	0056	N17	19.59	7.08	0.00
			0.3258	0.3402	136.13	0255	A1	21.17	7.70	35.34
			0.2732	0.2972	136.46		SW	17.75	6.73	30.28
			0.2572	0.2400	144.55	0425	N16	16.71	5.43	0.00
			0.0000	0.0000	180.00		A1	0.00	0.00	0.00

Smoke Case 6

AOD 63	AOD 86
0.55	0.25
0.6	0.35
0.44	0.21
0.51	0.31
0.48	0.28
0.4	0.25
0.49667	0.275
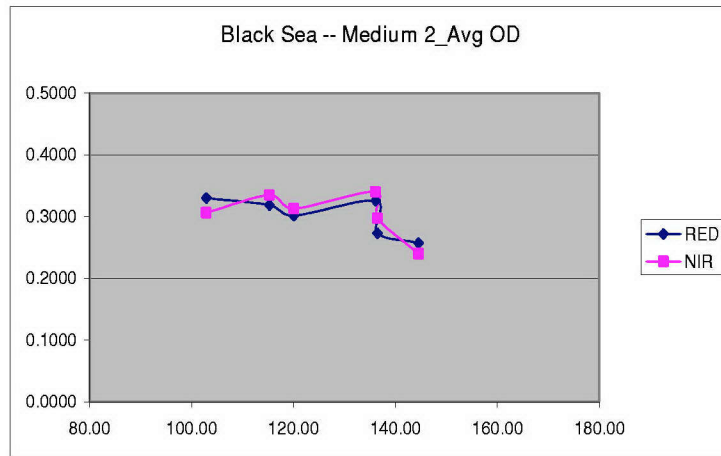
Figure 39.   Smoke case 6 over the Black Sea

Avg Optical Depth	Eo	K	Red Phase	NIR Phase	Linear Extrap times Cos(Sat Z) sorted by angle					
0.6267	1644	0.012197	0.0000	0.0000	90.00		N15	0.00	0.00	0.00
0.355	1034	0.034234	0.0000	0.0000	90.00		N15	0.00	0.00	0.00
			0.3014	0.2842	105.79	0243	N16	24.71	8.30	0.00
			0.2927	0.3142	115.97	0120	T1	24.00	9.18	37.75
			0.2753	0.3019	121.23	0056	N17	22.57	8.82	0.00
			0.2578	0.2877	135.20	0205	SW	21.13	8.41	33.95
			0.2943	0.3164	138.23	0255	A1	24.13	9.24	38.84
			0.2054	0.2006	142.87	0425	N16	16.84	5.86	0.00
			0.0000	0.0000	180.00		A1	0.00	0.00	0.00

Smoke Case 7

AOD 63	AOD 86
0.58	0.28
0.81	0.47
0.53	0.26
0.7	0.42
0.59	0.35
0.55	0.35
0.62667	0.355
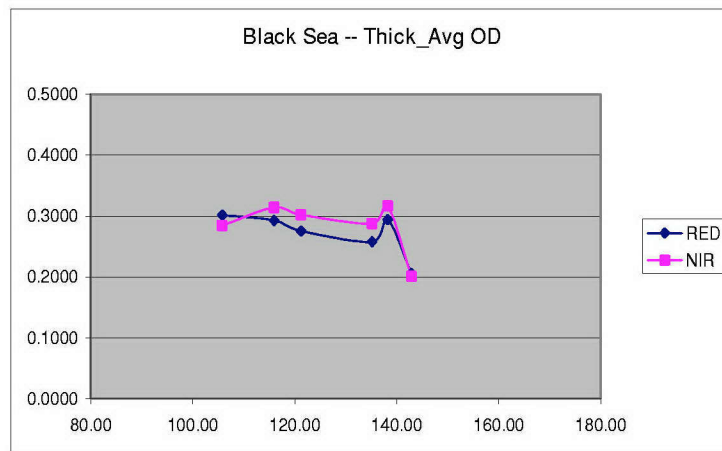
Figure 40.   Smoke case 7 over the Black Sea

Avg Optical Depth	Eo	K	Red Phase	NIR Phase	Linear Extrap times Cos(Sat Z) sorted by angle					
0.1833	1644	0.041701	0.0000	0.0000	90.00		N15	0.00	0.00	0.00
0.0933	1034	0.130259	0.0000	0.0000	90.00		N15	0.00	0.00	0.00
			0.4283	0.3647	107.42	0243	N16	10.27	2.80	0.00
			0.4632	0.4310	114.97	0120	T1	11.11	3.31	21.66
			0.5776	0.6096	119.63	0056	N17	13.85	4.68	0.00
			0.4329	0.4104	136.14		SW	10.38	3.15	21.35
			0.4887	0.4123	138.61	0255	A1	11.72	3.17	23.70
			0.4178	0.3335	141.96	0425	N16	10.02	2.56	0.00
			0.0000	0.0000	180.00		A1	0.00	0.00	0.00

Smoke Case 8

AOD 63	AOD 86
0.2	0.07
0.19	0.12
0.13	0.07
0.17	0.09
0.17	0.1
0.24	0.11
0.18333	0.09333333

Black Sea -- Thin BG_Avg OD
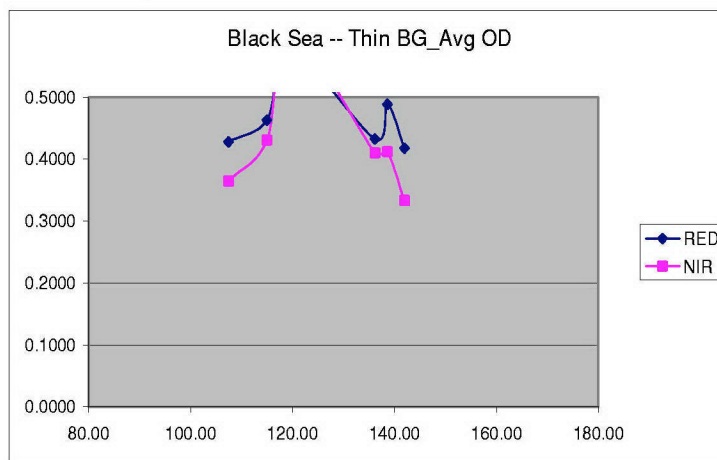
Figure 41.   Smoke case 8 over the Black Sea

C.   UNITED KINGDOM SMOKE CASES

UK

Apr 18, 2003

Med

Thin

Thick
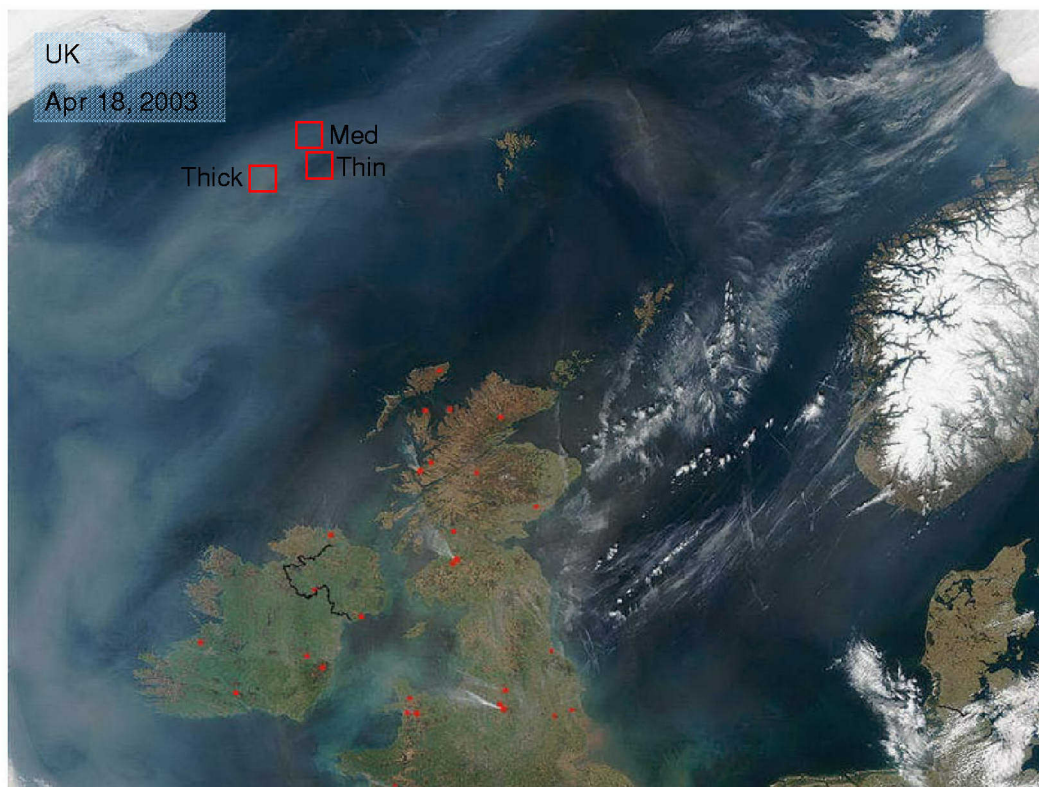
Figure 42.   Three smoke cases northwest of the United Kingdom
(from NASA GSFC, 2005b)

Avg Optical Depth	Eo	K	Red Phase	NIR Phase	Linear Extrap times Cos(Sat Z) sorted by angle					
0.405	1644	0.018874	0.0000	0.0000	90.00		N16	0.00	0.00	0.00
0.2625	1034	0.046298	0.0000	0.0000	90.00		N15	0.00	0.00	0.00
			0.0000	0.0000	111.77		N15	0.00	0.00	0.00
			0.3043	0.2872	111.77	0545	A1	16.12	6.20	26.33
			0.2721	0.2697	120.30	0533	SW	14.42	5.82	23.20
			0.2946	0.2565	131.21	0456	N17	15.61	5.54	0.00
			0.2977	0.2721	147.65	0710	SW	15.77	5.88	28.06
			0.0000	0.0000	180.00		A1	0.00	0.00	0.00
			0.0000	0.0000	180.00		T1	0.00	0.00	0.00

Smoke Case 9

AOD 63	AOD 86
0.33	0.24
0.51	0.31
0.39	0.25
0.39	0.25
0.405	0.2625
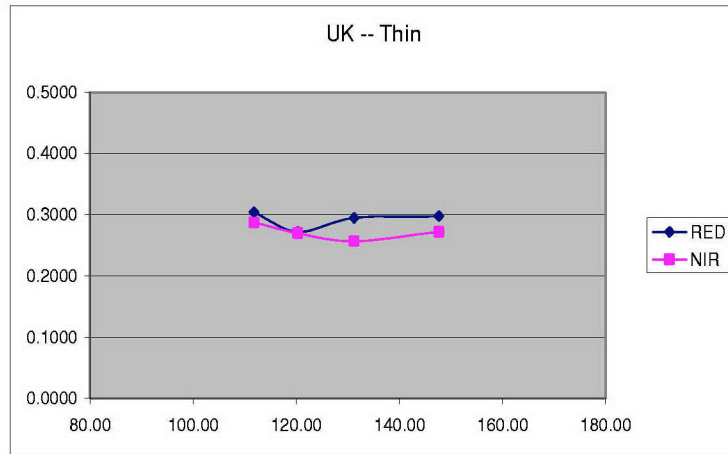
Figure 43.   Smoke case 9 northwest of the United Kingdom

Avg Optical Depth	Eo	K	Red Phase	NIR Phase	Linear Extrap times Cos(Sat Z) sorted by angle					
0.5175	1644	0.014771	0.0000	0.0000	90.00		N15	0.00	0.00	0.00
0.32	1034	0.037979	0.0000	0.0000	90.00		N16	0.00	0.00	0.00
			0.0000	0.0000	90.00		N15	0.00	0.00	0.00
			0.2938	0.3008	110.71	0545	A1	19.89	7.92	30.96
			0.2389	0.2578	119.64	0533	SW	16.18	6.79	25.49
			0.2704	0.2503	132.36	0456	N17	18.31	6.59	0.00
			0.2602	0.2531	148.28	0710	SW	17.62	6.66	30.56
			0.0000	0.0000	180.00		A1	0.00	0.00	0.00
			0.0000	0.0000	180.00		T1	0.00	0.00	0.00

Smoke Case 10

AOD 63	AOD 86
0.42	0.29
0.61	0.37
0.52	0.32
0.52	0.3
0.5175	0.32
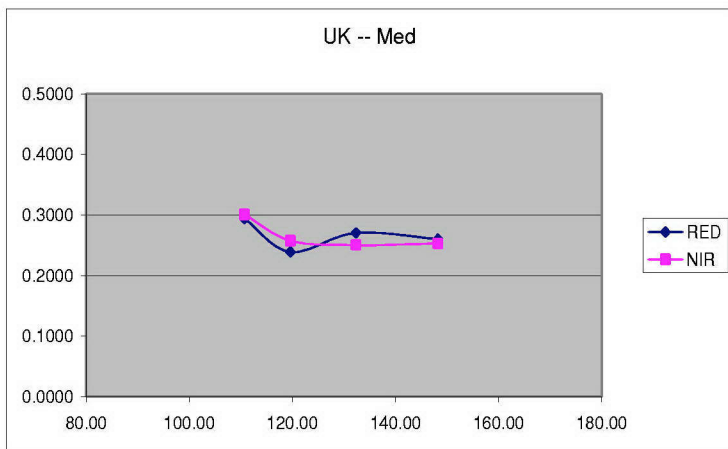
Figure 44.   Smoke case 10 northwest of the United Kingdom

Avg Optical Depth	Eo	K	Red Phase	NIR Phase	Linear Extrap times Cos(Sat Z) sorted by angle					
0.695	1644	0.010998	0.0000	0.0000	90.00		N15	0.00	0.00	0.00
0.4775	1034	0.025452	0.0000	0.0000	90.00		N16	0.00	0.00	0.00
			0.0000	0.0000	90.00		N15	0.00	0.00	0.00
			0.2717	0.2834	107.25	0545	A1	24.70	11.13	35.61
			0.2107	0.2221	119.25	0533	SW	19.16	8.73	27.95
			0.2338	0.2148	133.93	0456	N17	21.26	8.44	0.00
			0.2421	0.2336	149.01	0710	SW	22.02	9.18	35.30
			0.0000	0.0000	180.00		A1	0.00	0.00	0.00
			0.0000	0.0000	180.00		T1	0.00	0.00	0.00

Smoke Case 11

AOD 63	AOD 86
0.56	0.4
0.82	0.56
0.73	0.52
0.67	0.43
0.695	0.4775
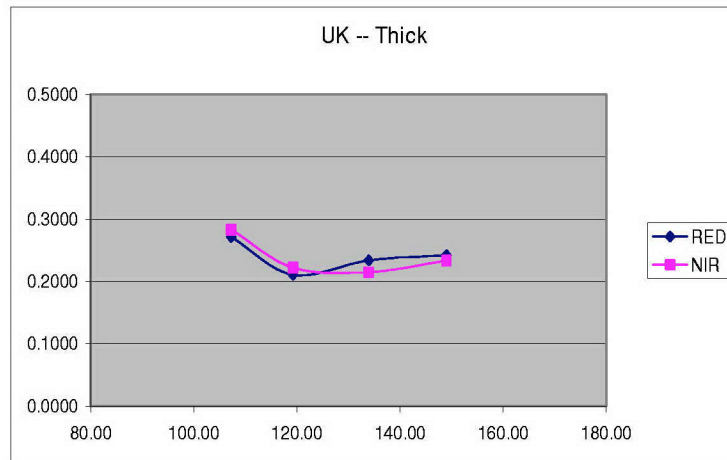
Figure 45. Smoke case 11 northwest of the United Kingdom

D. UNITED KINGDOM SECOND SET OF SMOKE CASES

Figure 46. Three smoke cases west of the United Kingdom
(from NASA GSFC, 2005b)

56

Optical Depth	Eo	K	Red Phas	NIR Phase	Linear Extrap times Cos(Sat Z) sorted by angle					
0.36	1644	0.021233	0.0000	0.0000	90.00			0.00	0.00	0.00
0.2067	1034	0.058796	0.0000	0.0000	90.00		N16	0.00	0.00	0.00
			0.0000	0.0000	90.00		N15	0.00	0.00	0.00
			0.3208	0.3168	107.72	0545	A1	15.11	5.39	25.29
			0.3188	0.3107	111.95	0540	T1	15.01	5.28	25.48
			0.2746	0.2785	121.95	0533	SW	12.93	4.74	22.23
			0.3238	0.3063	129.01	0456	N17	15.25	5.21	0.00
			0.2926	0.2661	135.39	0400	T1	13.78	4.53	24.56
			0.2995	0.2872	145.34	0710	SW	14.11	4.88	26.27

Smoke Case 12

| Model	AOD 63	AOD 86
7	0.34	0.2
7	0.4	0.22
4.58	0.32	0.21
7	0.35	0.2
7	0.43	0.21
7	0.32	0.2
	0.36	0.20667
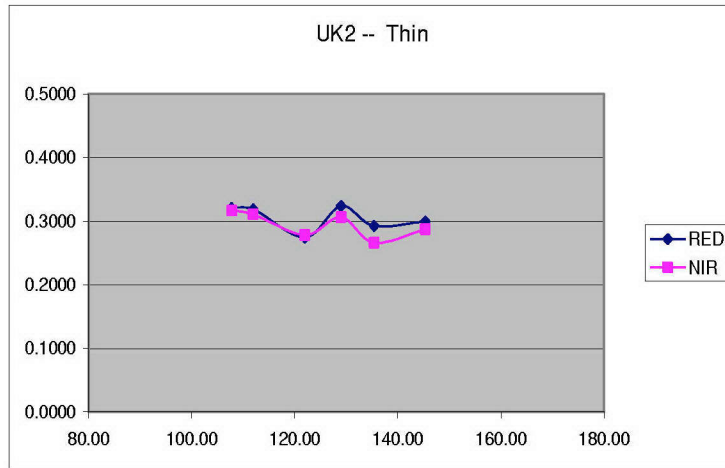
Figure 47.   Smoke case 12 west of the United Kingdom

Optical Depth	Eo	K	Red Phas	NIR Phase	Linear Extrap times Cos(Sat Z) sorted by angle					
0.5033	1644	0.015187	0.0000	0.0000	90.00			0.00	0.00	0.00
0.2867	1034	0.04239	0.0000	0.0000	90.00		N16	0.00	0.00	0.00
			0.0000	0.0000	90.00		N15	0.00	0.00	0.00
			0.2951	0.3142	106.70	0545	A1	19.43	7.41	30.44
			0.2848	0.2983	113.82	0540	T1	18.75	7.04	30.20
			0.2369	0.2590	121.32	0533	SW	15.60	6.11	25.05
			0.2822	0.2802	130.42	0456	N17	18.58	6.61	0.00
			0.2507	0.2488	134.83	0400	T1	16.51	5.87	27.78
			0.2583	0.2641	146.69	0710	SW	17.01	6.23	30.05

Smoke Case 13

| Model	AOD 63	AOD 86
7	0.48	0.28
7	0.55	0.3
5.04	0.45	0.29
7	0.49	0.28
7	0.59	0.3
7	0.46	0.27
	0.50333333	0.28667
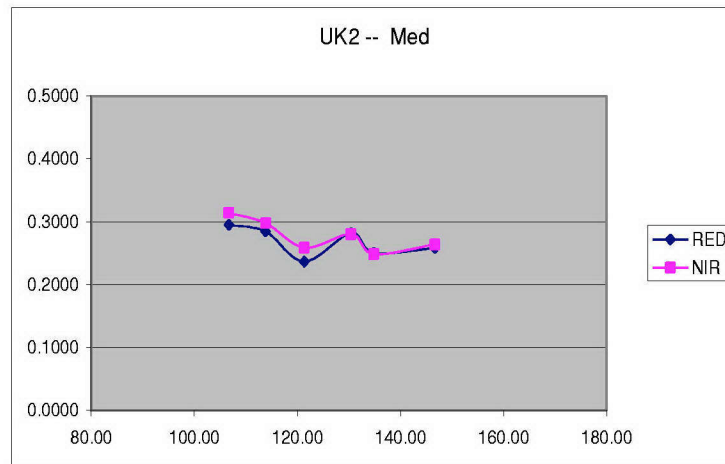
Figure 48.   Smoke case 13 west of the United Kingdom

Optical Depth	Eo	K	Red Phase	NIR Phase	Linear Extrap times Cos(Sat Z) sorted by angle					
0.595	1644	0.012847	0.0000	0.0000	90.00			0.00	0.00	0.00
0.3467	1034	0.035054	0.0000	0.0000	90.00	N16		0.00	0.00	0.00
			0.0000	0.0000	90.00	N15		0.00	0.00	0.00
			0.2880	0.3129	104.44	0545	A1	22.42	8.93	33.79
			0.2779	0.2945	114.72	0540	T1	21.63	8.40	33.92
			0.2188	0.2457	120.56	0533	SW	17.03	7.01	26.96
			0.2652	0.2647	132.35	0456	N17	20.64	7.55	0.00
			0.2372	0.2448	135.17	0400	T1	18.47	6.98	29.85
			0.2404	0.2478	148.05	0710	SW	18.71	7.07	32.28

Smoke Case 14

Model	AOD 63	AOD 86
7	0.58	0.35
6.98	0.63	0.36
4.93	0.51	0.33
7	0.59	0.34
7	0.71	0.37
7	0.55	0.33
	0.595	0.34667

UK2 -- Thick
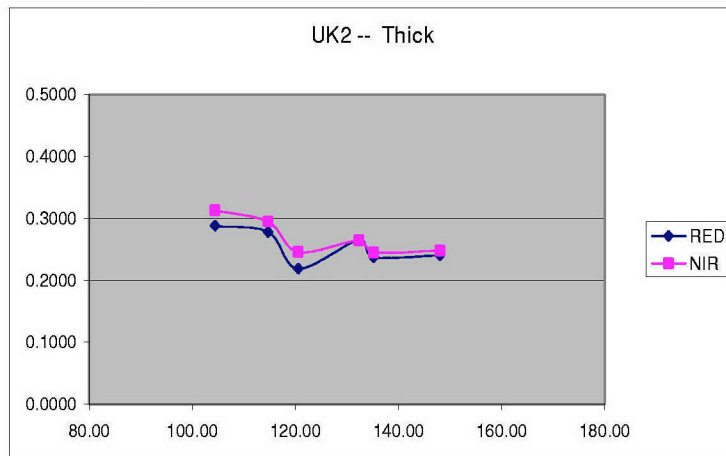
Figure 49.   Smoke case 14 west of the United Kingdom

E.   JAPAN SMOKE CASES

Japan
May 23, 2003

Figure 50.   Four smoke cases near mainland Japan

Optical Depth	Eo	K	Red Phase	NIR Phase	Linear Extrap times Cos(Sat Z) sorted by angle					
1.455	1644	0.005253	0.0000	0.0000	90.00			0.00	0.00	0.00
0.915	1034	0.013282	0.0000	0.0000	90.00		N16	0.00	0.00	0.00
			0.0000	0.0000	90.00		SW	0.00	0.00	0.00
			0.0000	0.0000	90.00		N15	0.00	0.00	0.00
			0.2506	0.2749	118.29	1843	N17	47.70	20.70	0.00
			0.2145	0.2440	148.88	1750	T1	40.84	18.37	58.27
			0.2576	0.2778	149.11	1942	SW	49.03	20.92	69.49
			0.2355	0.2552	160.07	2100	A1	44.82	19.22	65.52
			0.0000	0.0000	180.00		T1	0.00	0.00	0.00

Smoke Case 15

Model	AOD 63	AOD 86
4.91	1.51	0.97
6.46	1.56	0.98
6.01	1.46	0.89
7	1.29	0.82
	1.455	0.915
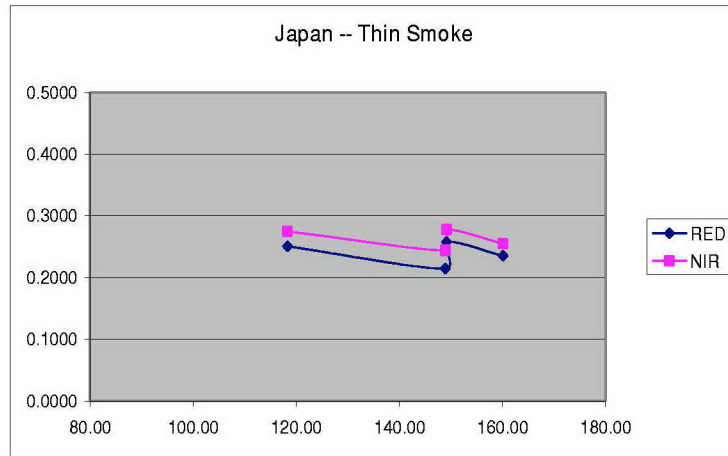
Figure 51.   Smoke case 15 near mainland Japan

Optical Depth	Eo	K	Red Phase	NIR Phase	Linear Extrap times Cos(Sat Z) sorted by angle					
1.44	1644	0.005308	0.0000	0.0000	90.00			0.00	0.00	0.00
0.9	1034	0.013504	0.0000	0.0000	90.00		N16	0.00	0.00	0.00
			0.0000	0.0000	90.00		SW	0.00	0.00	0.00
			0.0000	0.0000	90.00		N15	0.00	0.00	0.00
			0.2443	0.2729	117.28	1843	N17	46.03	20.21	0.00
			0.2228	0.2512	150.43	1745	T1	41.96	18.60	60.15
			0.2564	0.2758	151.15	1942	SW	48.30	20.42	68.58
			0.2315	0.2532	158.35	2100	A1	43.61	18.75	63.89
			0.0000	0.0000	180.00		T1	0.00	0.00	0.00

Smoke Case 16

Model	AOD 63	AOD 86
5.3	1.53	0.96
6.48	1.49	0.93
5.92	1.45	0.89
7	1.29	0.82
	1.44	0.9
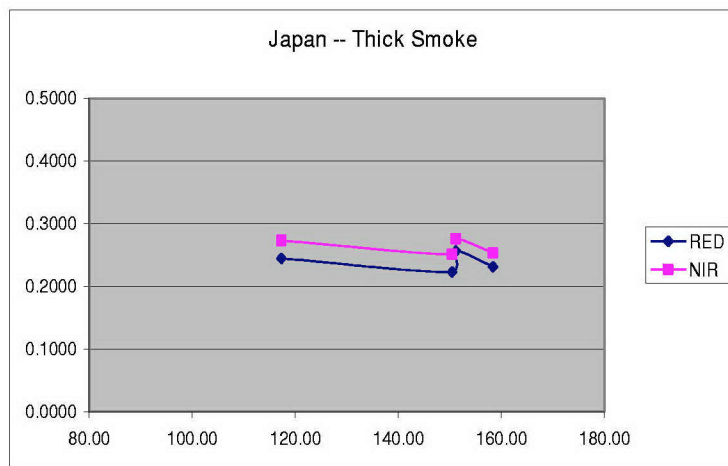
Figure 52.   Smoke case 16 near mainland Japan

Optical Depth	Eo	K	Red Phas	NIR Phase	Linear Extrap times Cos(Sat Z) sorted by angle					
1.1375	1644	0.00672	0.0000	0.0000	90.00			0.00	0.00	0.00
0.705	1034	0.017239	0.0000	0.0000	90.00		N16	0.00	0.00	0.00
			0.0000	0.0000	90.00		SW	0.00	0.00	0.00
			0.0000	0.0000	90.00		N15	0.00	0.00	0.00
			0.2597	0.2843	117.15	1843	N17	38.64	16.49	0.00
			0.2300	0.2541	149.18	1750	T1	34.22	14.74	50.88
			0.2651	0.2777	149.69	1942	SW	39.44	16.11	58.32
			0.2461	0.2600	161.24	2100	A1	36.63	15.08	56.03
			0.0000	0.0000	180.00		T1	0.00	0.00	0.00

Smoke Case 17

Model	AOD 63	AOD 86
5.45	1.23	0.77
6.76	1.17	0.72
6.12	1.11	0.67
7	1.04	0.66
	1.1375	0.705

Japan -- Med Smoke
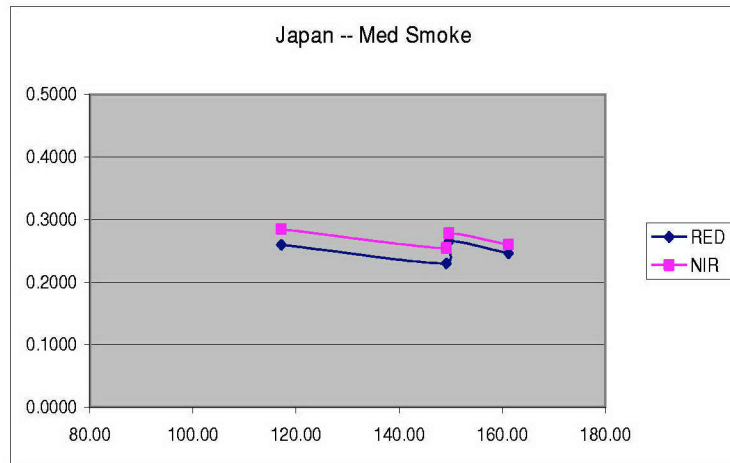
Figure 53.   Smoke case 17 near mainland Japan

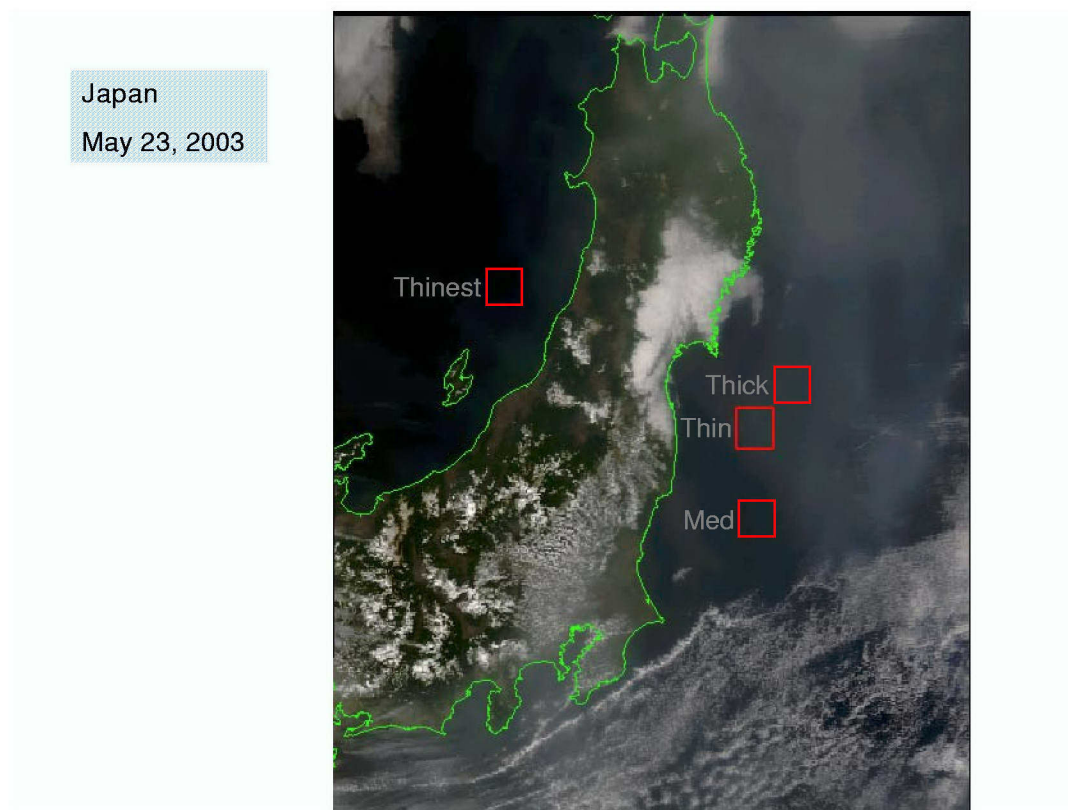| Optical Depth	Eo	K	Red Phas	NIR Phase	Linear Extrap times Cos(Sat Z) sorted by angle					
0.754	1644	0.010138	0.0000	0.0000	90.00			0.00	0.00	0.00
0.486	1034	0.025007	0.0000	0.0000	90.00		N16	0.00	0.00	0.00
			0.0000	0.0000	90.00		SW	0.00	0.00	0.00
			0.0000	0.0000	90.00		N15	0.00	0.00	0.00
			0.2728	0.2919	109.84	1925	T1	26.91	11.67	38.60
		Sunglint?	0.3483	0.4051	131.65	1843	N17	34.36	16.20	0.00
			0.2660	0.2588	133.23	1942	SW	26.24	10.35	39.59
			0.2310	0.2440	141.81	1750	T1	22.79	9.76	34.66
			0.2872	0.2700	166.62	2100	A1	28.33	10.80	46.01

Smoke Case 18

Model	AOD 63	AOD 86
4.9	0.84	0.54
7	0.93	0.52
5.87	0.63	0.4
7	0.81	0.49
7	0.56	0.48
	0.754	0.486

Japan -- Thinest Smoke
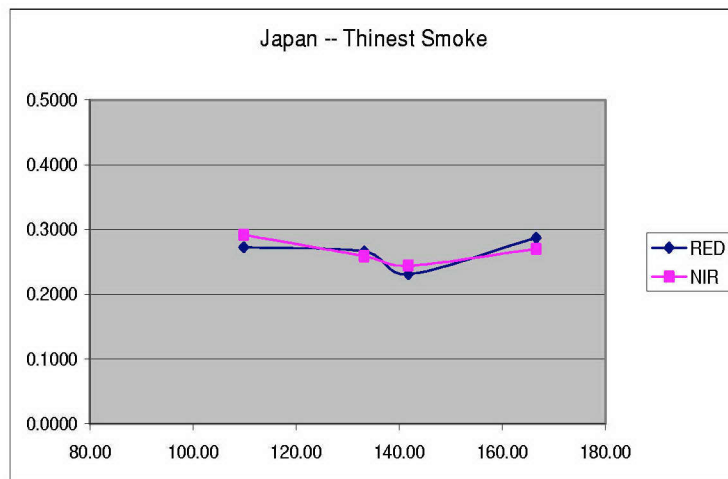
Figure 54.   Smoke case 18 near mainland Japan

APPENDIX B.   GRAPHS OF INDIVIDUAL DUST CASES

A.   PERSIAN GULF DUST CASES
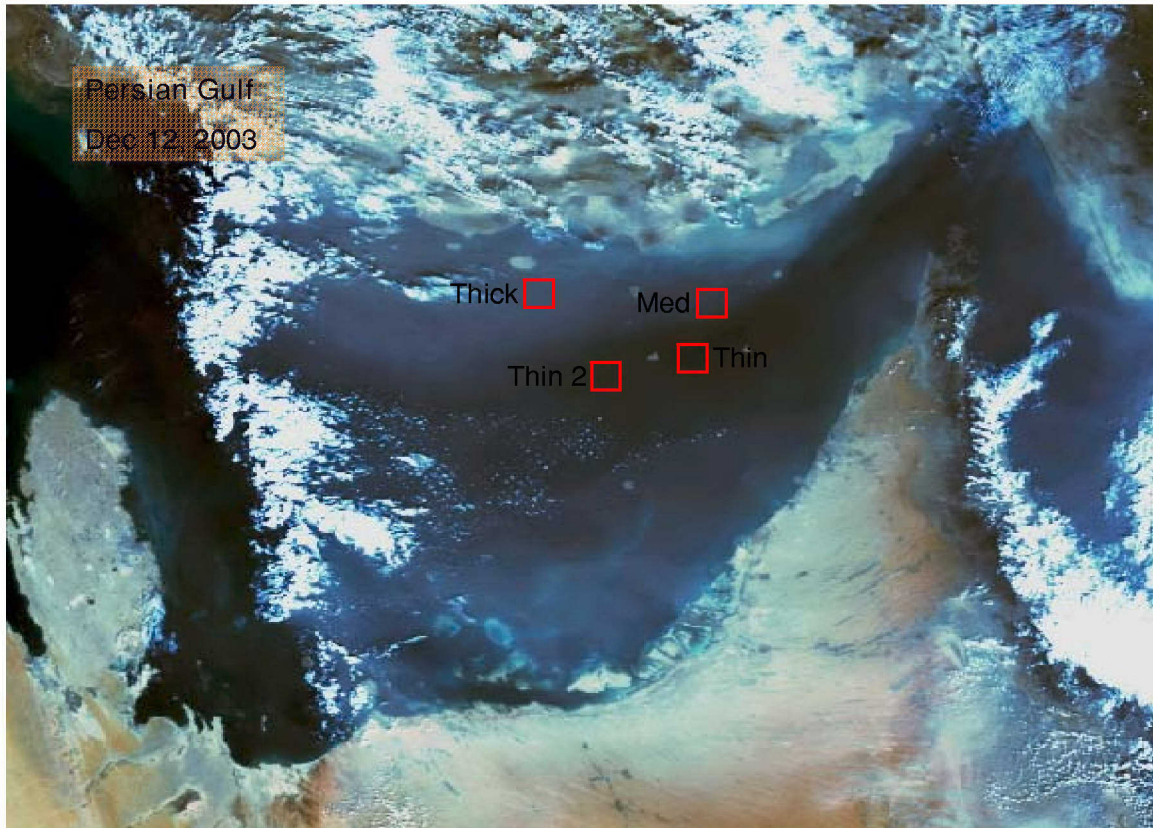
Figure 55.   Four dust near the Persian Gulf

Optical Depth	Eo	K	Red Phase	NIR Phase	Linear Extrap times Cos(Sat Z) sorted by angle					
1.8925	1644	0.004039	0.0000	0.0000	90.00		A1	0.00	0.00	0.00
1.645	1034	0.007388	0.0000	0.0000	90.00		SW	0.00	0.00	0.00
			0.0000	0.0000	90.00		SW	0.00	0.00	0.00
			0.0000	0.0000	90.00		N15	0.00	0.00	0.00
			0.1867	0.1852	113.29	13/0201	N16	46.23	25.07	0.00
			0.1697	0.1625	119.01	2303	N17	42.02	22.00	0.00
			0.1772	0.1852	123.95	2310	T1	43.86	25.07	56.17
			0.1606	0.1751	136.52	13/0215	A1	39.77	23.69	0.00
			0.0000	0.0000	180.00		A1	0.00	0.00	0.00

Dust Case 1

Model	AOD 63	AOD 86
1	1.76	1.51
1	2.28	1.97
1	1.89	1.72
1.57	1.64	1.38
	1.8925	1.645
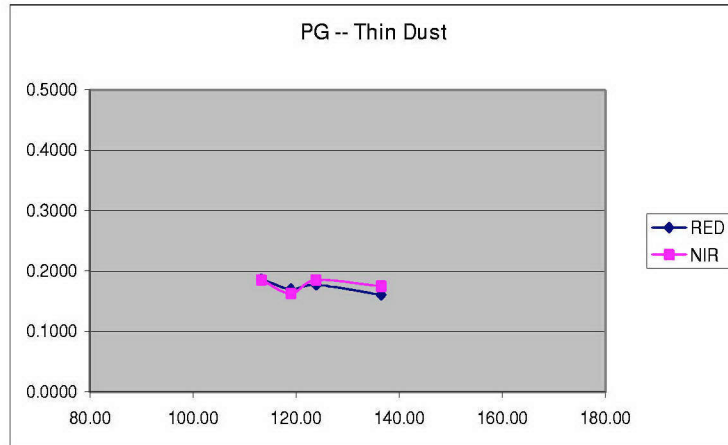
Figure 56.   Dust case 1 near the Persian Gulf

Optical Depth	Eo	K	Red Phase	NIR Phase	Linear Extrap times Cos(Sat Z) sorted by angle					
3.18	1644	0.002404	0.0000	0.0000	90.00		A1	0.00	0.00	0.00
2.84	1034	0.004279	0.0000	0.0000	90.00		SW	0.00	0.00	0.00
			0.0000	0.0000	90.00		SW	0.00	0.00	0.00
			0.0000	0.0000	90.00		N15	0.00	0.00	0.00
			0.1529	0.1541	109.97	13/0201	N16	63.59	36.01	0.00
			0.1742	0.1760	122.54	2303	N17	72.46	41.12	0.00
			0.1871	0.2079	127.96	2310	T1	77.82	48.59	88.38
			0.1249	0.1385	136.68	13/0215	A1	51.96	32.36	31.95
			0.0000	0.0000	180.00		A1	0.00	0.00	0.00

Dust Case 2

Model	AOD 63	AOD 86
1	2.32	2.05
1	3.1	2.73
1	3.94	3.69
1	3.36	2.89
	3.18	2.84
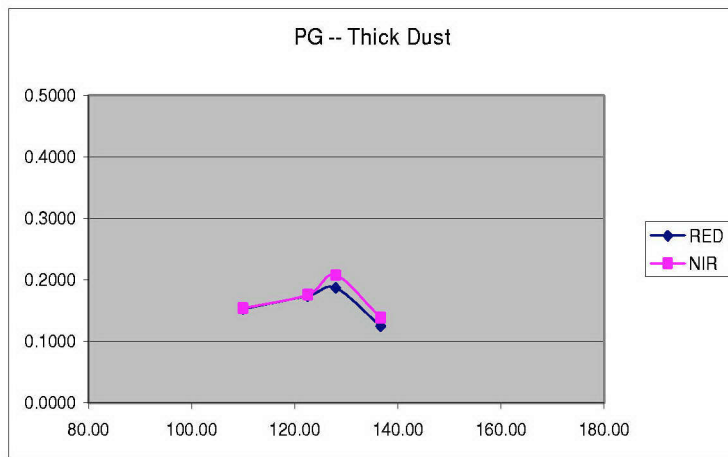
Figure 57.   Dust case 2 near the Persian Gulf

Optical Depth	Eo	K	Red Phase	NIR Phase	Linear Extrap times Cos(Sat Z) sorted by angle					
2.0125	1644	0.003798	0.0000	0.0000	90.00		A1	0.00	0.00	0.00
1.785	1034	0.006808	0.0000	0.0000	90.00		SW	0.00	0.00	0.00
			0.0000	0.0000	90.00		SW	0.00	0.00	0.00
			0.0000	0.0000	90.00		N15	0.00	0.00	0.00
			0.2004	0.1980	113.40	13/0201	N16	52.76	29.08	0.00
			0.2141	0.2100	118.90	2303	N17	56.37	30.84	0.00
			0.1691	0.1850	135.95	13/0215	A1	44.52	27.17	52.71
			0.2274	0.2466	148.90	2310	T1	59.87	36.22	71.42
			0.0000	0.0000	180.00		A1	0.00	0.00	0.00

Dust Case 3

| Model	AOD 63	AOD 86
1	2.06	1.78
1	2.67	2.33
1	0.97	1.02
2.35	2.35	2.01
	2.0125	1.785
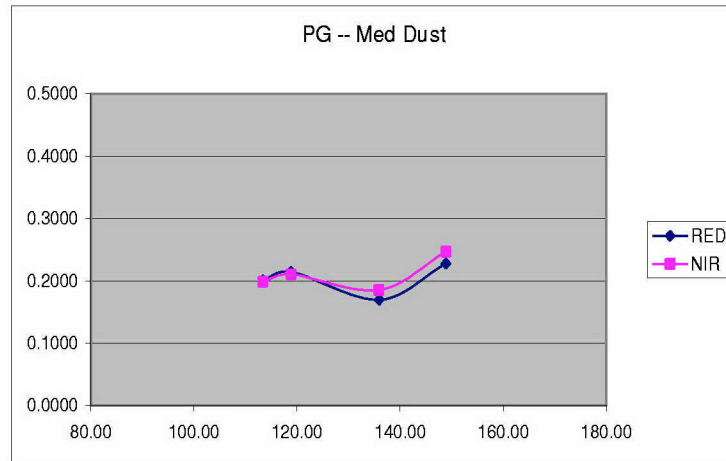
Figure 58.   Dust case 3 near the Persian Gulf

Optical Depth	Eo	K	Red Phase	NIR Phase	Linear Extrap times Cos(Sat Z) sorted by angle					
1.8725	1644	0.004082	0.0000	0.0000	90.00		A1	0.00	0.00	0.00
1.62	1034	0.007502	0.0000	0.0000	90.00		SW	0.00	0.00	0.00
			0.0000	0.0000	90.00		SW	0.00	0.00	0.00
			0.0000	0.0000	90.00		N15	0.00	0.00	0.00
			0.1679	0.1639	110.79	13/0201	N16	41.14	21.85	0.00
			0.1853	0.1806	121.02	2303	N17	45.39	24.07	0.00
			0.1932	0.2052	126.30	2310	T1	47.32	27.35	60.06
			0.1479	0.1564	136.96	13/0215	A1	36.23	20.84	46.03
			0.0000	0.0000	180.00		A1	0.00	0.00	0.00

Dust Case 4

Model	AOD 63	AOD 86
1	1.44	1.23
1	2.04	1.72
1	2.14	1.96
1.41	1.87	1.57
	1.8725	1.62
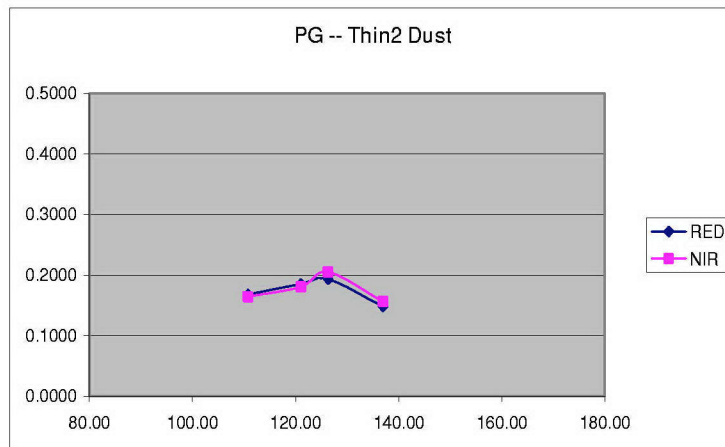
Figure 59.   Dust case 4 near the Persian Gulf

B. PAKISTAN DUST CASES
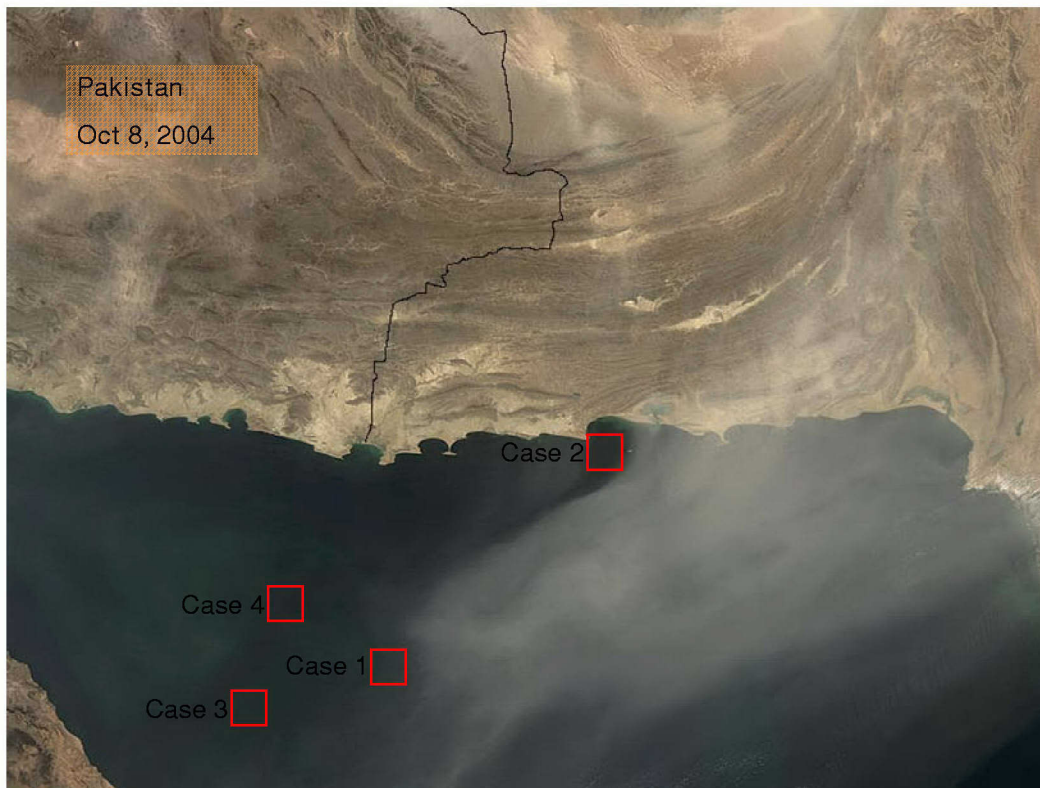
Figure 60. Four dust cases near Pakistan
(from NASA GSFC, 2005b)

Optical Depth	Eo	K	Red Phas	NIR Phase		Linear Extrap times Cos(Sat Z) sorted by angle					
0.712	1644	0.010736	0.0000	0.0000	90.00			0.00	0.00	0.00
0.556	1034	0.021858	0.0000	0.0000	90.00		SW	0.00	0.00	0.00
			0.0000	0.0000	90.00		N15	0.00	0.00	0.00
			0.2743	0.2527	122.07	7/2348	N17	25.55	11.56	0.00
			0.3059	0.3037	128.94	0200	A1	28.49	13.89	43.36
			0.2454	0.2039	136.59	0310	N16	22.86	9.33	0.00
			0.2347	0.2144	138.85	0103	SW	21.86	9.81	35.90
			0.2580	0.2452	143.24		T1	24.03	11.22	35.75
			0.0000	0.0000	180.00		T1	0.00	0.00	0.00

Dust Case 5

Model	AOD 63	AOD 86
4.88	0.7	0.48
2.18	0.77	0.6
1.21	0.61	0.56
2.93	0.88	0.65
3.44	0.6	0.49
	0.712	0.556
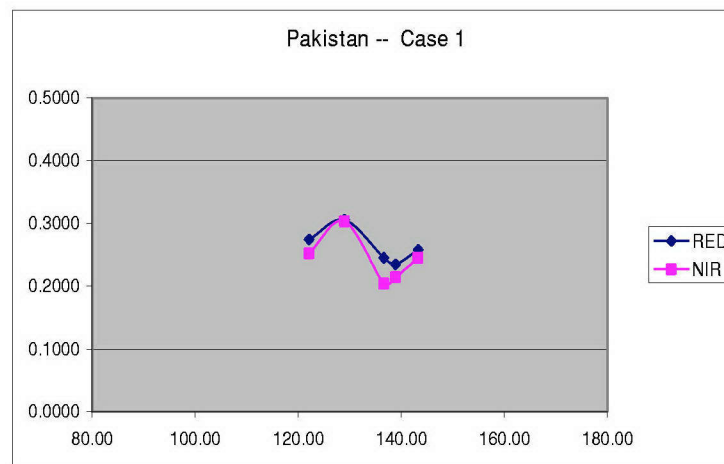
Figure 61. Dust case 5 near Pakistan

64

Optical Depth	Eo	K	Red Phase	NIR Phase	\multicolumn{Linear Extrap times Cos(Sat Z) sorted by angle}					

Optical Depth	Eo	K	Red Phase	NIR Phase	Linear Extrap times Cos(Sat Z) sorted by angle					
0.494	1644	0.015473	0.0000	0.0000	90.00			0.00	0.00	0.00
0.374	1034	0.032495	0.0000	0.0000	90.00		SW	0.00	0.00	0.00
			0.0000	0.0000	90.00		N15	0.00	0.00	0.00
			0.3093	0.2730	121.96	7/2348	N17	19.99	8.40	0.00
			0.3077	0.2731	131.14	0200	A1	19.88	8.41	31.94
			0.2736	0.2414	138.50	0103	SW	17.68	7.43	29.58
			0.2728	0.2128	138.79	0310	N16	17.63	6.55	0.00
			0.2925	0.2591	141.91	7/2255	T1	18.90	7.98	29.84
			0.0000	0.0000	180.00		T1	0.00	0.00	0.00

Dust Case 6

Model	AOD 63	AOD 86
4.91	0.47	0.31
1.92	0.56	0.45
2.46	0.38	0.33
4.15	0.64	0.44
3.75	0.42	0.34
	0.494	0.374
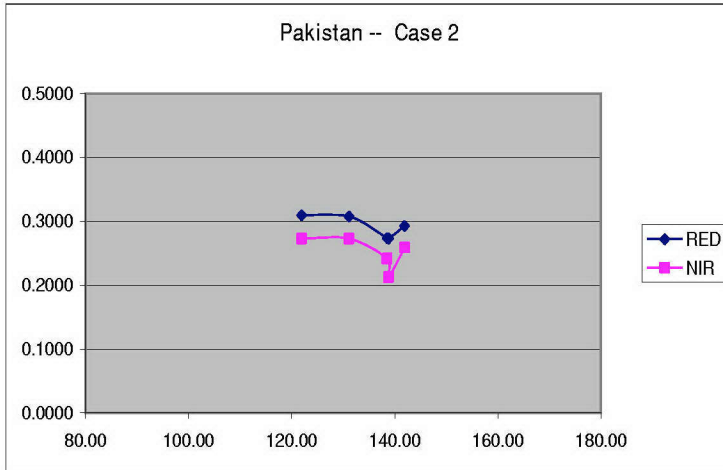
Figure 62.   Dust case 6 near Pakistan

Optical Depth	Eo	K	Red Phase	NIR Phase	Linear Extrap times Cos(Sat Z) sorted by angle					
0.504	1644	0.015166	0.0000	0.0000	90.00			0.00	0.00	0.00
0.384	1034	0.031649	0.0000	0.0000	90.00		SW	0.00	0.00	0.00
			0.0000	0.0000	90.00		N15	0.00	0.00	0.00
			0.3176	0.2934	122.41	0200	A1	20.94	9.27	34.42
			0.3111	0.2652	126.36	7/2348	N17	20.51	8.38	0.00
			0.2706	0.2139	130.82	0310	N16	17.84	6.76	0.00
			0.2778	0.2516	135.04	0103	SW	18.32	7.95	31.24
			0.2855	0.2568	141.42	7/2255	T1	18.83	8.11	30.09
			0.0000	0.0000	180.00		T1	0.00	0.00	0.00

Dust Case 7

Model	AOD 63	AOD 86
5.2	0.43	0.3
1.82	0.66	0.52
2.21	0.38	0.33
3.87	0.66	0.46
4.33	0.39	0.31
	0.504	0.384
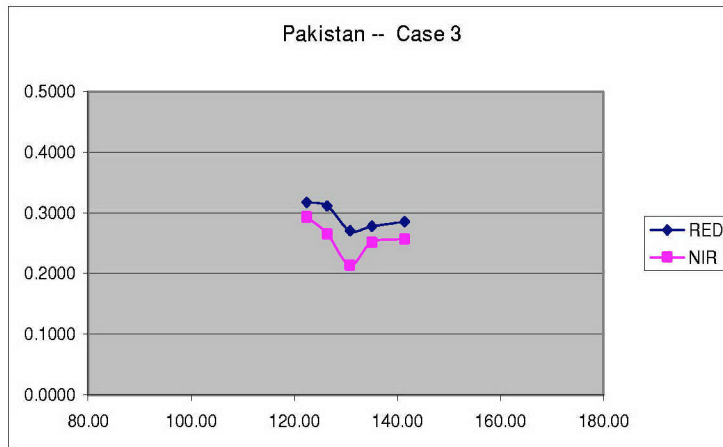
Figure 63.   Dust case 7 near Pakistan

Optical Depth	Eo	K	Red Phase	NIR Phase	Linear Extrap times Cos(Sat Z) sorted by angle					
0.4925	1644	0.01552	0.0000	0.0000	90.00			0.00	0.00	0.00
0.37	1034	0.032846	0.0000	0.0000	90.00		SW	0.00	0.00	0.00
			0.0000	0.0000	90.00		N15	0.00	0.00	0.00
			0.3103	0.2784	124.77	0200	A1	19.99	8.48	32.91
			0.3030	0.2486	126.46	7/2348	N17	19.52	7.57	0.00
			0.2733	0.2151	133.35	0310	N16	17.61	6.55	0.00
			0.2727	0.2434	134.71	0103	SW	17.57	7.41	29.92
			0.2884	0.2587	141.16	7/2255	T1	18.58	7.87	29.69
			0.0000	0.0000	180.00		T1	0.00	0.00	0.00

Dust Case 8

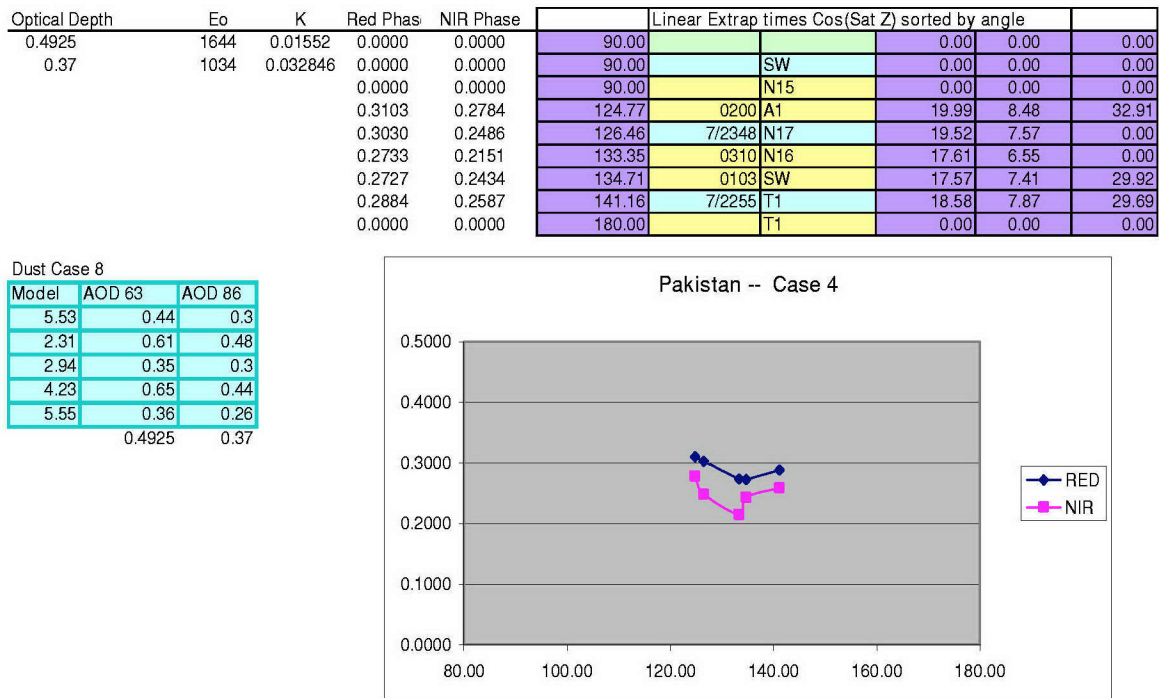| Model	AOD 63	AOD 86
5.53	0.44	0.3
2.31	0.61	0.48
2.94	0.35	0.3
4.23	0.65	0.44
5.55	0.36	0.26
	0.4925	0.37

Figure 64.   Dust case 8 near Pakistan
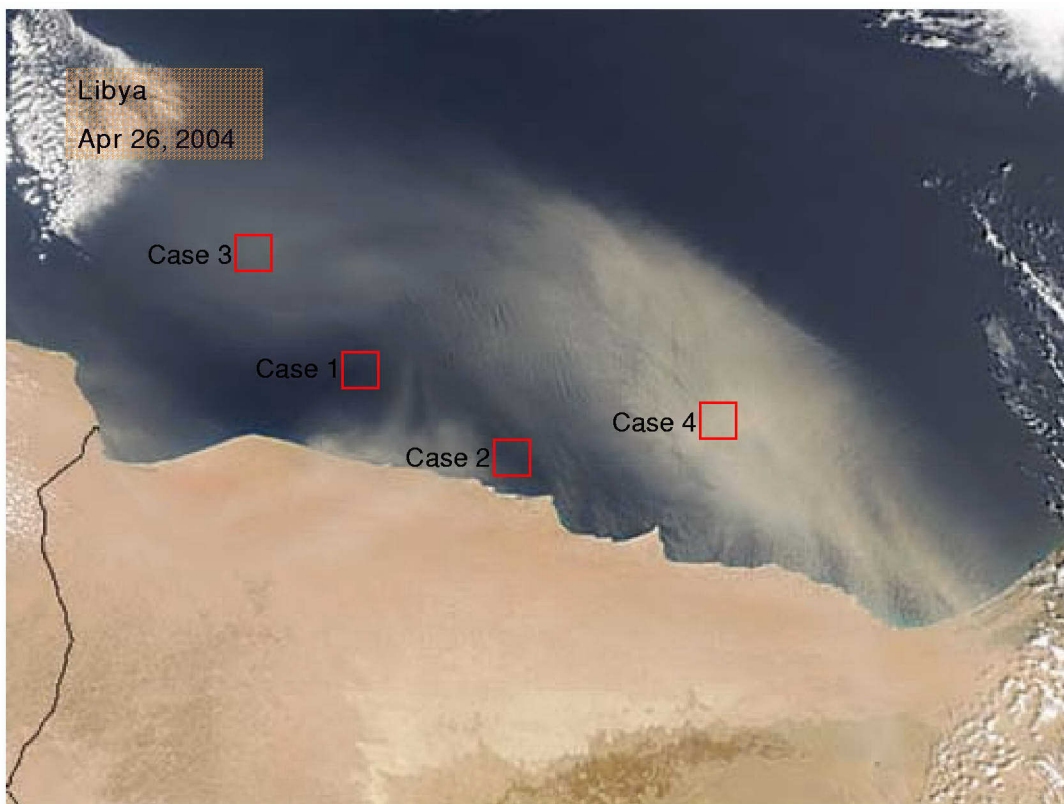
C.   LIBYA DUST CASES

Figure 65.   Four dust cases near Libya
(from NASA GSFC, 2005b)

Optical Depth	Eo	K	Red Phase	NIR Phase	Linear Extrap times Cos(Sat Z) sorted by angle					
0.43	1644	0.017776	0.0000	0.0000	90.00			0.00	0.00	0.00
0.378	1034	0.032151	0.0000	0.0000	90.00		SW	0.00	0.00	0.00
			0.0000	0.0000	90.00		N15	0.00	0.00	0.00
			0.3847	0.3411	101.52	0422	N16	21.64	10.61	0.00
			0.4920	0.4482	123.31	0219	N17	27.68	13.94	0.00
			0.3407	0.2666	148.95	0500	A1	19.17	8.29	30.22
			0.3565	0.2824	155.47	0405	SW	20.06	8.78	32.98
			0.4342	0.3456	167.27	0150	T1	24.42	10.75	38.77
			0.0000	0.0000	180.00		T1	0.00	0.00	0.00

Dust Case 9

Model	AOD 63	AOD 86
1	0.47	0.42
1	0.33	0.28
1	0.39	0.32
1	0.34	0.28
1	0.62	0.59
	0.43	0.378
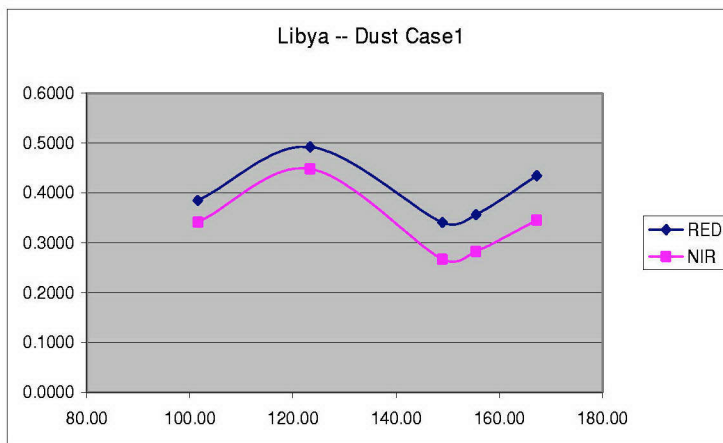
Libya -- Dust Case1

Figure 66.   Dust case 9 near Libya

Optical Depth	Eo	K	Red Phase	NIR Phase	Linear Extrap times Cos(Sat Z) sorted by angle					
0.602	1644	0.012697	0.0000	0.0000	90.00			0.00	0.00	0.00
0.528	1034	0.023017	0.0000	0.0000	90.00		SW	0.00	0.00	0.00
			0.0000	0.0000	90.00		N15	0.00	0.00	0.00
			0.3275	0.3027	104.47	0422	N16	25.79	13.15	0.00
			0.3931	0.3616	119.50	0219	N17	30.96	15.71	0.00
			0.2914	0.2524	146.34	0500	A1	22.95	10.96	33.67
			0.2956	0.2538	149.53	0405	SW	23.28	11.02	35.96
			0.4163	0.3690	165.83	0150	T1	32.79	16.03	47.80
			0.0000	0.0000	180.00		T1	0.00	0.00	0.00

Dust Case 10

Model	AOD 63	AOD 86
1	0.55	0.5
1	0.44	0.41
1	0.68	0.54
1	0.51	0.43
1	0.83	0.76
	0.602	0.528
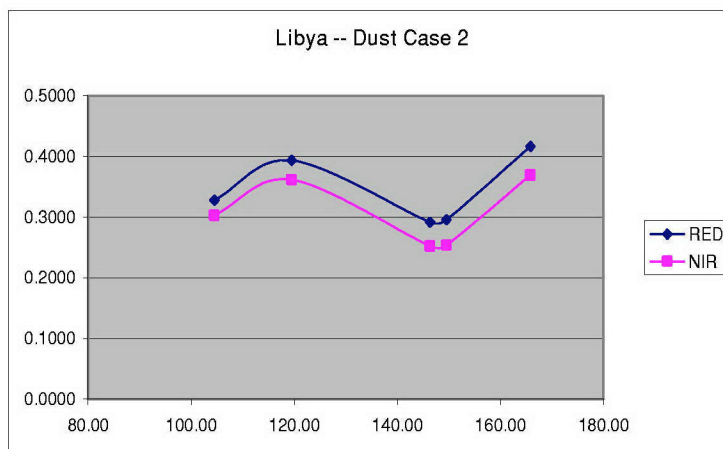
Libya -- Dust Case 2

Figure 67.   Dust case 10 near Libya

Optical Depth		Eo	K	Red Phase	NIR Phase		Linear Extrap times Cos(Sat Z) sorted by angle				
1.01		1644	0.007568	0.0000	0.0000	90.00			0.00	0.00	0.00
0.904		1034	0.013444	0.0000	0.0000	90.00		SW	0.00	0.00	0.00
				0.0000	0.0000	90.00		N15	0.00	0.00	0.00
				0.3336	0.3314	101.66	0422	N16	44.08	24.65	0.00
				0.3242	0.3037	126.23	0219	N17	42.84	22.59	0.00
				0.3111	0.3100	149.35	0500	A1	41.10	23.06	52.61
				0.3509	0.3499	158.57	0405	SW	46.36	26.02	60.65
				0.3197	0.2975	165.81	0150	T1	42.25	22.13	57.64
				0.0000	0.0000	180.00		T1	0.00	0.00	0.00

Dust Case 11

Model	AOD 63	AOD 86
1	1.1	1.01
1	1.06	0.92
1	1.13	1.02
1	0.8	0.67
0.85	0.96	0.9
	1.01	0.904
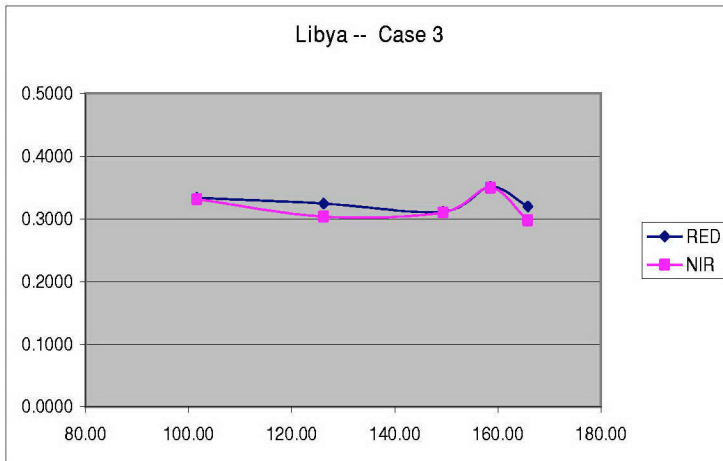
Figure 68. Dust case 11 near Libya

Optical Depth		Eo	K	Red Phase	NIR Phase		Linear Extrap times Cos(Sat Z) sorted by angle				
2.906		1644	0.00263	0.0000	0.0000	90.00			0.00	0.00	0.00
2.82		1034	0.00431	0.0000	0.0000	90.00		SW	0.00	0.00	0.00
				0.0000	0.0000	90.00		N15	0.00	0.00	0.00
				0.2597	0.2649	105.63	0422	N16	98.72	61.47	0.00
				0.2719	0.2834	116.84	0219	N17	103.38	65.76	0.00
				0.1899	0.2023	146.11	0500	A1	72.19	46.93	78.75
				0.2695	0.2847	150.57	0405	SW	102.45	66.05	110.77
				0.3798	0.4011	161.83	0150	T1	144.39	93.06	152.87
				0.0000	0.0000	180.00		T1	0.00	0.00	0.00

Dust Case 12

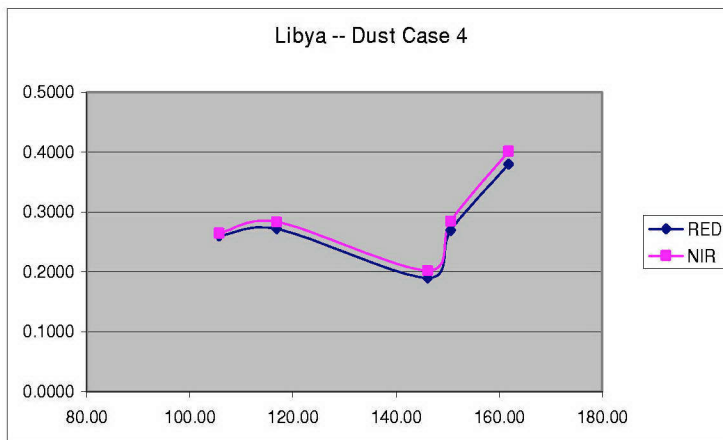| Model	AOD 63	AOD 86
1	2.45	2.45
1	2.85	2.78
1	2.85	2.65
1	2.79	2.65
1	3.59	3.57
	2.906	2.82

Figure 69. Dust case 12 near Libya
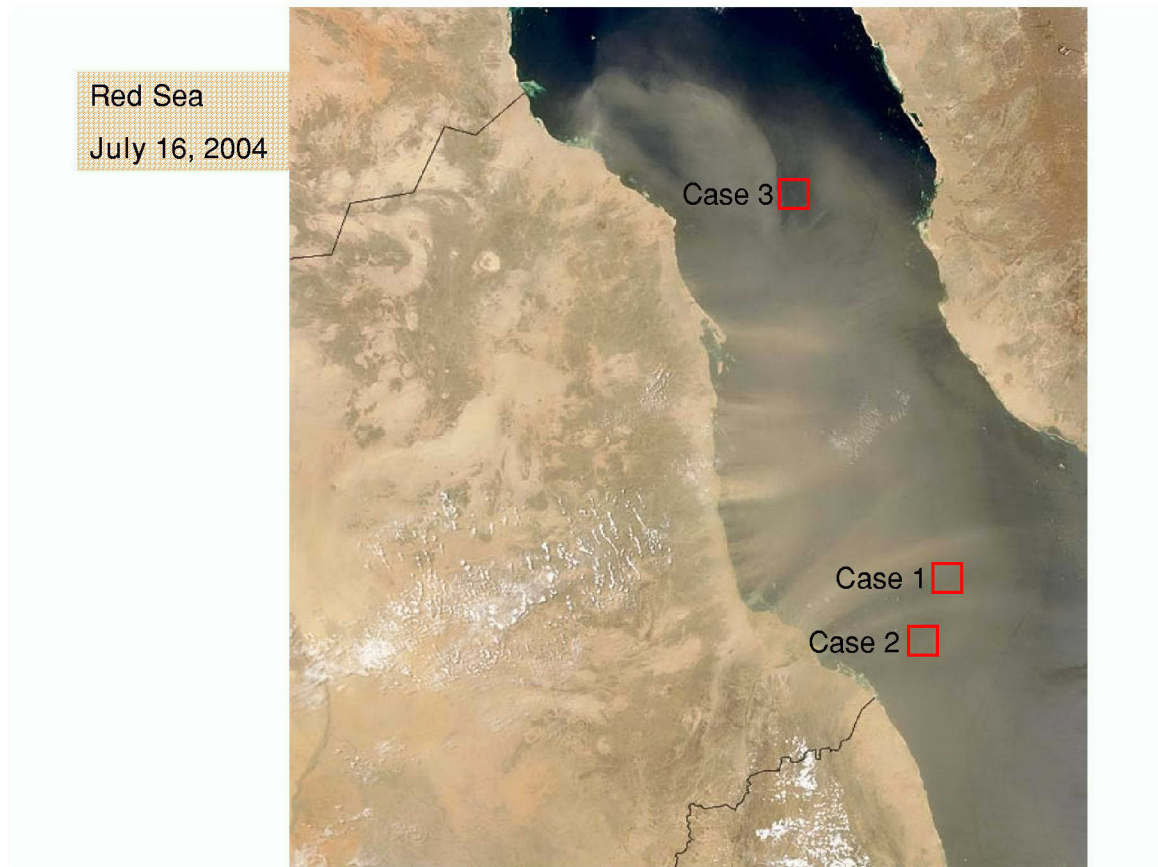
D.   RED SEA DUST CASES

Figure 70.   Three dust cases over the Red Sea
(from NASA GSFC, 2005b)

Optical Depth	Eo	K	Red Phase	NIR Phase	Linear Extrap times Cos(Sat Z) sorted by angle					
1.075	1644	0.00711	0.0000	0.0000	90.00			0.00	0.00	0.00
0.9475	1034	0.012827	0.0000	0.0000	90.00		SW	0.00	0.00	0.00
			0.0000	0.0000	90.00		N17	0.00	0.00	0.00
			0.0000	0.0000	90.00		N15	0.00	0.00	0.00
			0.2800	0.2611	111.49	0357	N16	39.38	20.36	0.00
			0.2664	0.2730	140.87	0313	SW	37.47	21.28	47.65
			0.2838	0.2745	157.35	0405	A1	39.91	21.40	52.10
			0.4084	0.4150	163.03	0100	T1	57.44	32.36	71.53
			0.0000	0.0000	180.00		T1	0.00	0.00	0.00

Dust Case 13

Model	AOD 63	AOD 86
1.54	0.93	0.83
1	0.86	0.79
1	1.59	1.4
1	0.92	0.77
	1.075	0.9475

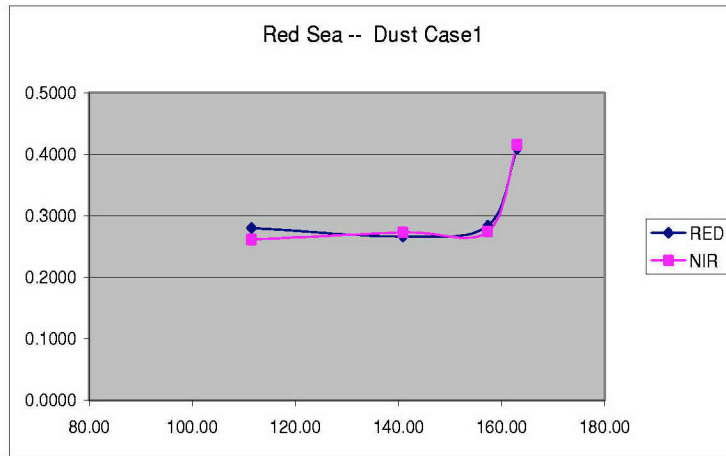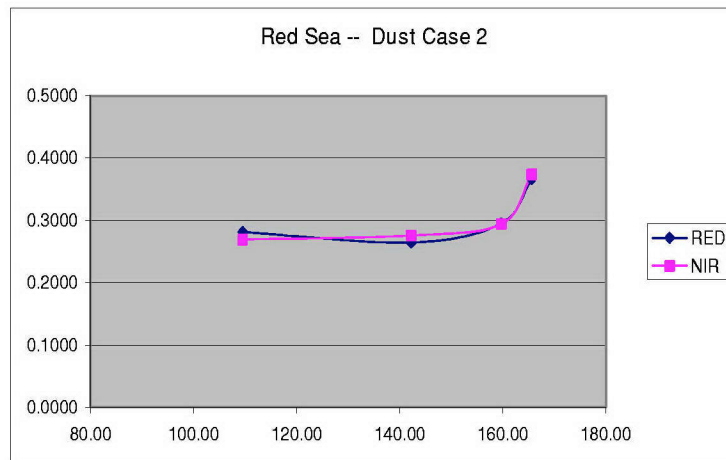

Figure 71.   Dust case 13 over the Red Sea

Optical Depth	Eo	K	Red Phase	NIR Phase	Linear Extrap times Cos(Sat Z) sorted by angle					
1.2425	1644	0.006152	0.0000	0.0000	90.00			0.00	0.00	0.00
1.09	1034	0.01115	0.0000	0.0000	90.00		SW	0.00	0.00	0.00
			0.0000	0.0000	90.00		N17	0.00	0.00	0.00
			0.0000	0.0000	90.00		N15	0.00	0.00	0.00
			0.2810	0.2690	109.56	0357	N16	45.68	24.13	0.00
			0.2644	0.2757	142.25	0313	SW	42.97	24.73	53.59
			0.2951	0.2939	159.74	0405	A1	47.98	26.36	60.42
			0.3664	0.3733	165.62	0100	T1	59.56	33.49	73.87
			0.0000	0.0000	180.00		T1	0.00	0.00	0.00

Dust Case 14

Model	AOD 63	AOD 86
1.21	1.17	1.04
1	0.93	0.84
1	1.75	1.54
1	1.12	0.94
	1.2425	1.09

Figure 72.   Dust case 14 over the Red Sea

70

Optical Depth	Eo	K	Red Phase	NIR Phase	Linear Extrap times Cos(Sat Z) sorted by angle				
0.725	1644	0.010543	0.0000	0.0000	90.00			0.00	0.00	0.00
0.61	1034	0.019923	0.0000	0.0000	90.00		SW	0.00	0.00	0.00
			0.0000	0.0000	90.00		N17	0.00	0.00	0.00
			0.0000	0.0000	90.00		N15	0.00	0.00	0.00
			0.3360	0.3188	110.56	0357	N16	31.87	16.00	0.00
			0.3576	0.3584	150.01	0313	SW	33.92	17.99	46.26
			0.3476	0.3209	161.83	0405	A1	32.97	16.11	46.64
			0.4786	0.4008	175.37	0100	T1	45.40	20.12	54.06
			0.0000	0.0000	180.00		T1	0.00	0.00	0.00

Dust Case 15

Model	AOD 63	AOD 86
1.71	0.74	0.65
2.65	0.78	0.59
1	0.7	0.66
1.86	0.68	0.54
	0.725	0.61

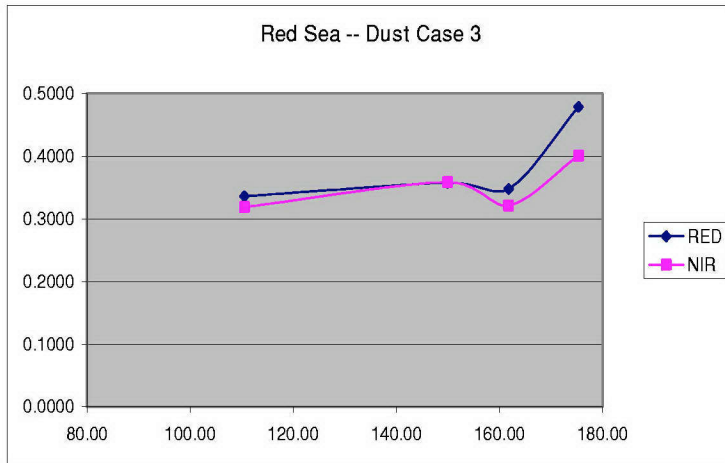Red Sea -- Dust Case 3

Figure 73.   Dust case 15 over the Red Sea

E.   NAMIBIA DUST CASE

It can be seen in Figure 74 that there is dust blowing off the coast of Namibia. This however, is a case where the dust spread out quickly as it left the coast. The aerosol properties of the dust plume tracked in the box did not remain constant for each satellite image. The optical depth has most assuredly changed as the dust has spread out. Therefore, this case was not able to be used for evaluation and represents a specific limitation to this method.
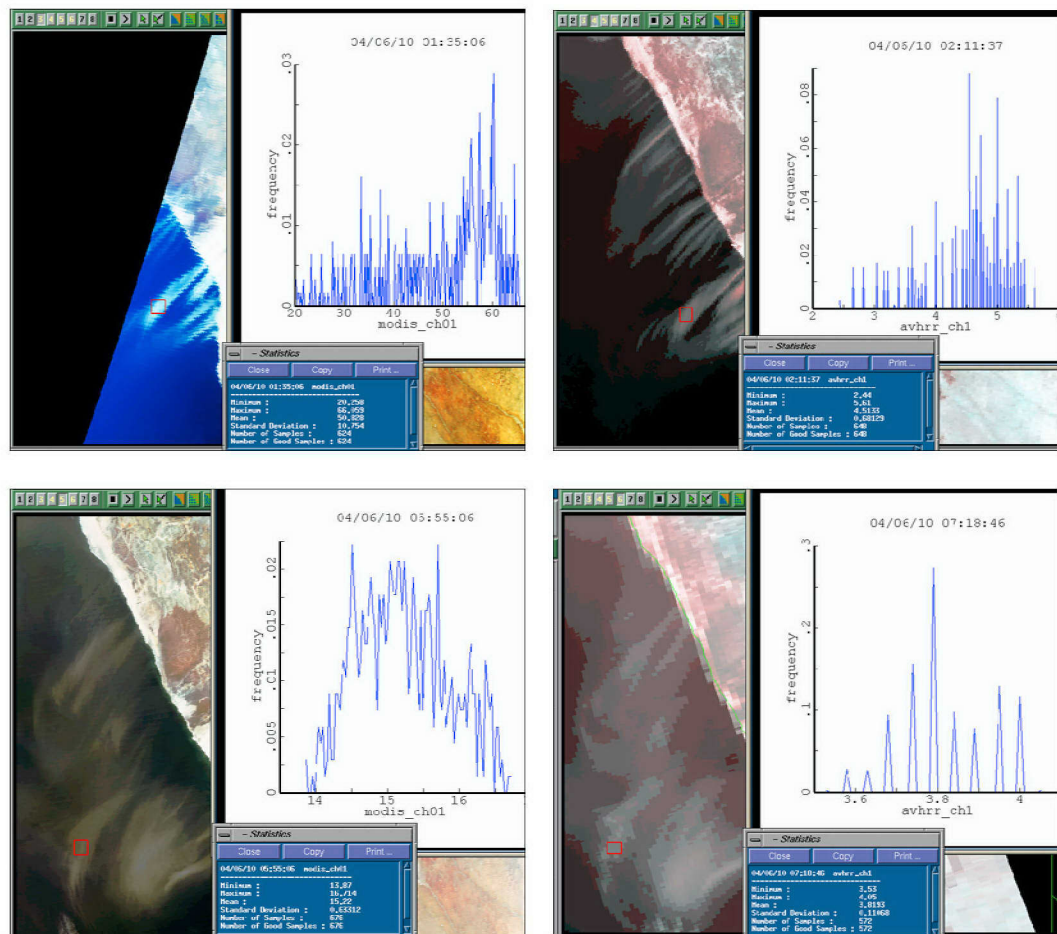

Figure 74.   Sequence of satellite images showing a dust feature changing too rapidly to be used a case study

APPENDIX C.   AERONET OBSERVATIONS

All of the graphics in this appendix were generated at the NASA, Goddard Space Flight Center web site (http://aeronet.gsfc.nasa.gov/data_menu.html)
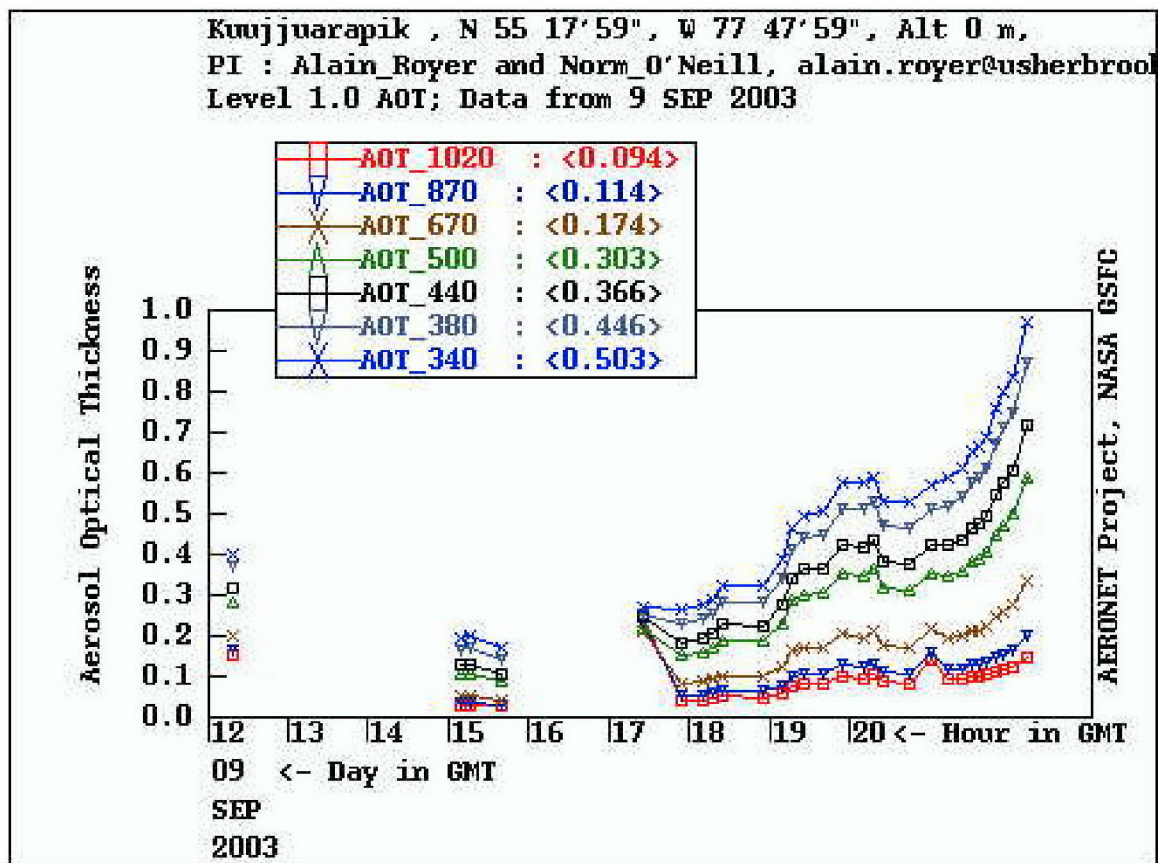

Figure 75.   AERONET data from Kuujjuarapik, south of Hudson Bay
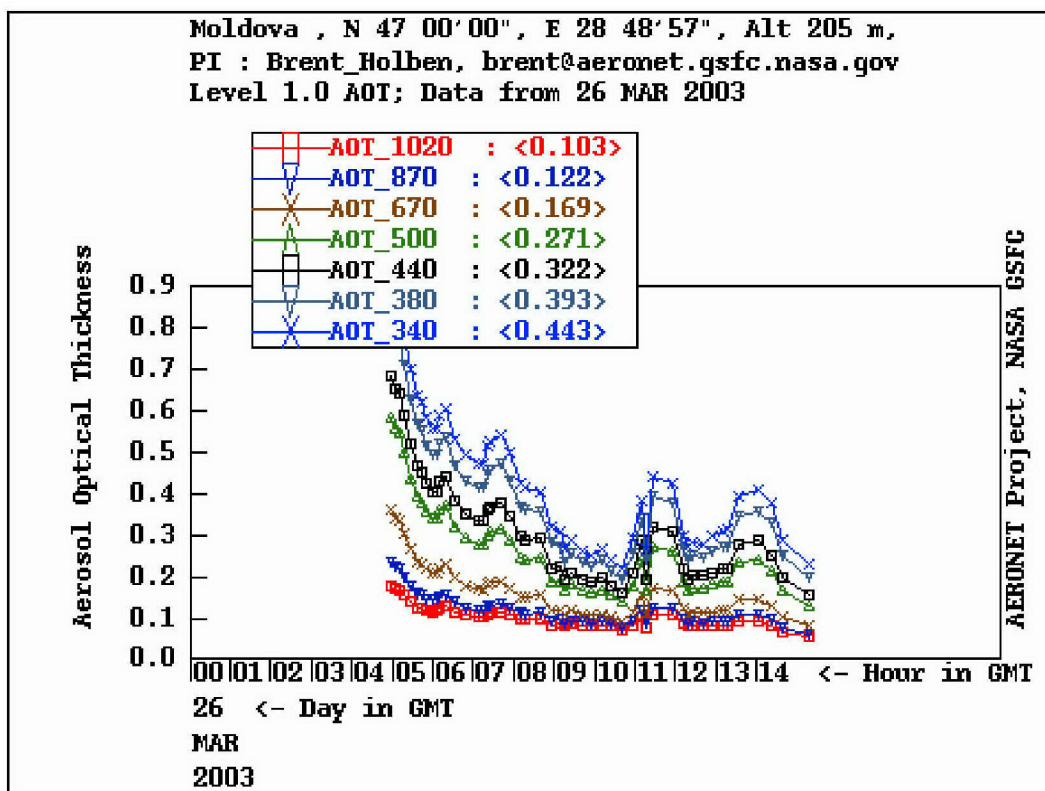
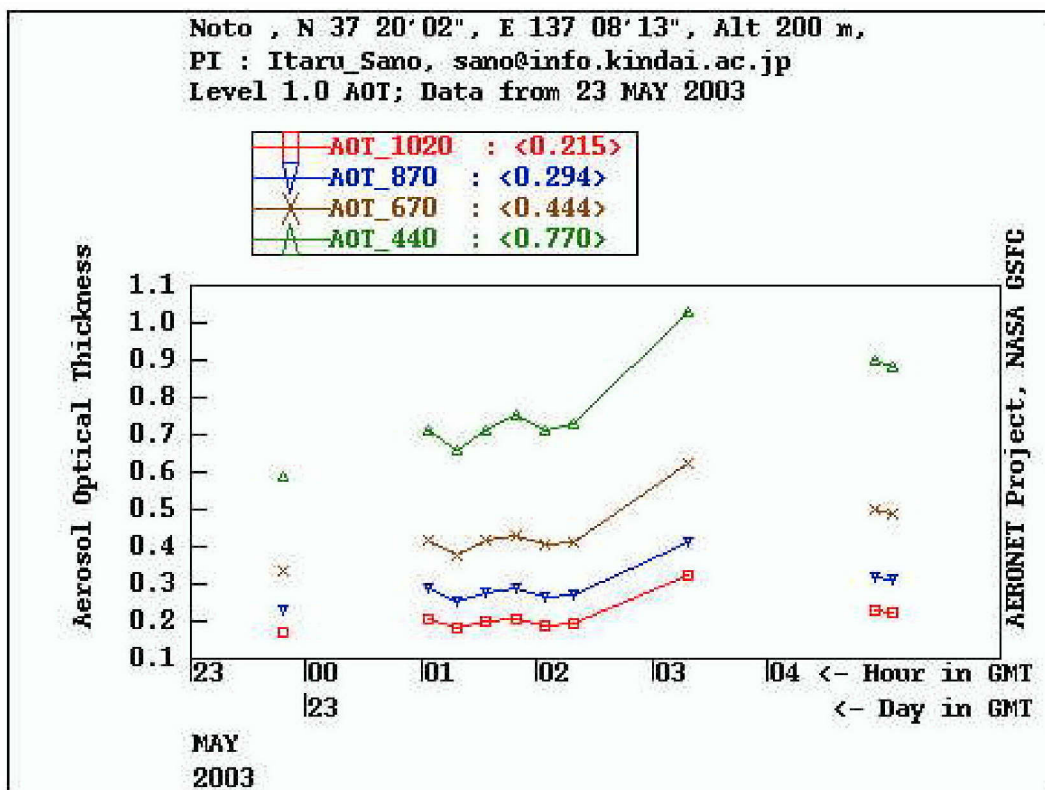Figure 76.   AERONET data from Moldova, west of Black Sea

Figure 77.   AERONET data from Noto, on mainland Japan
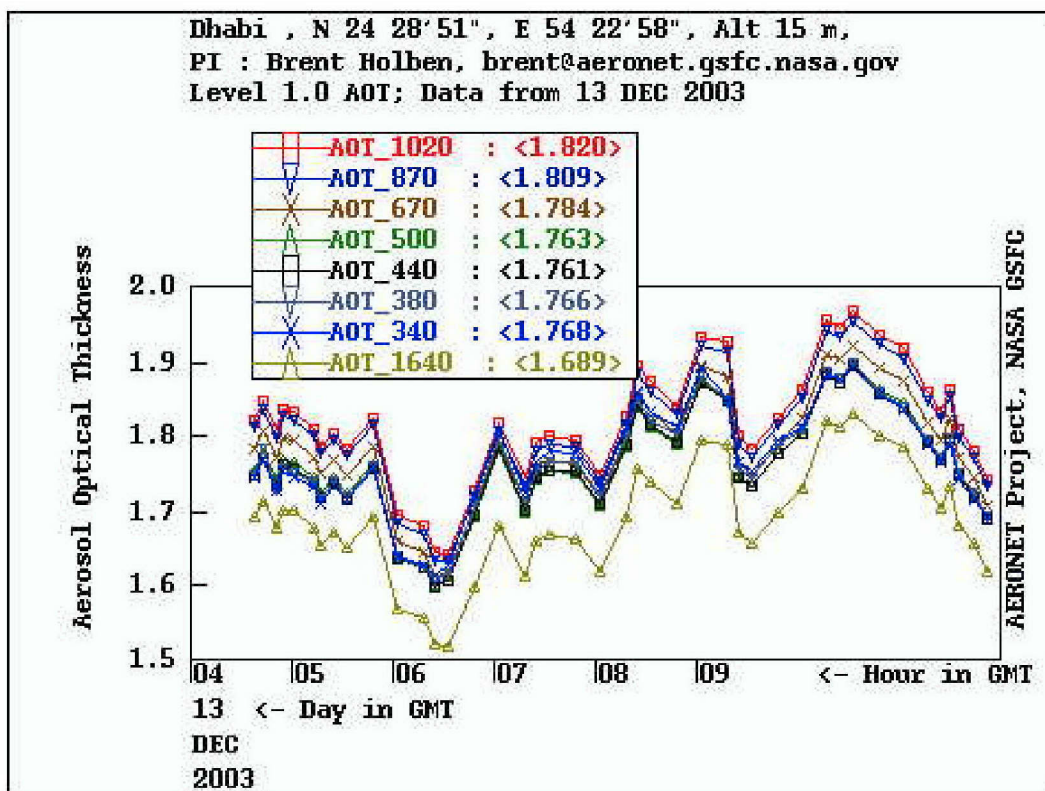
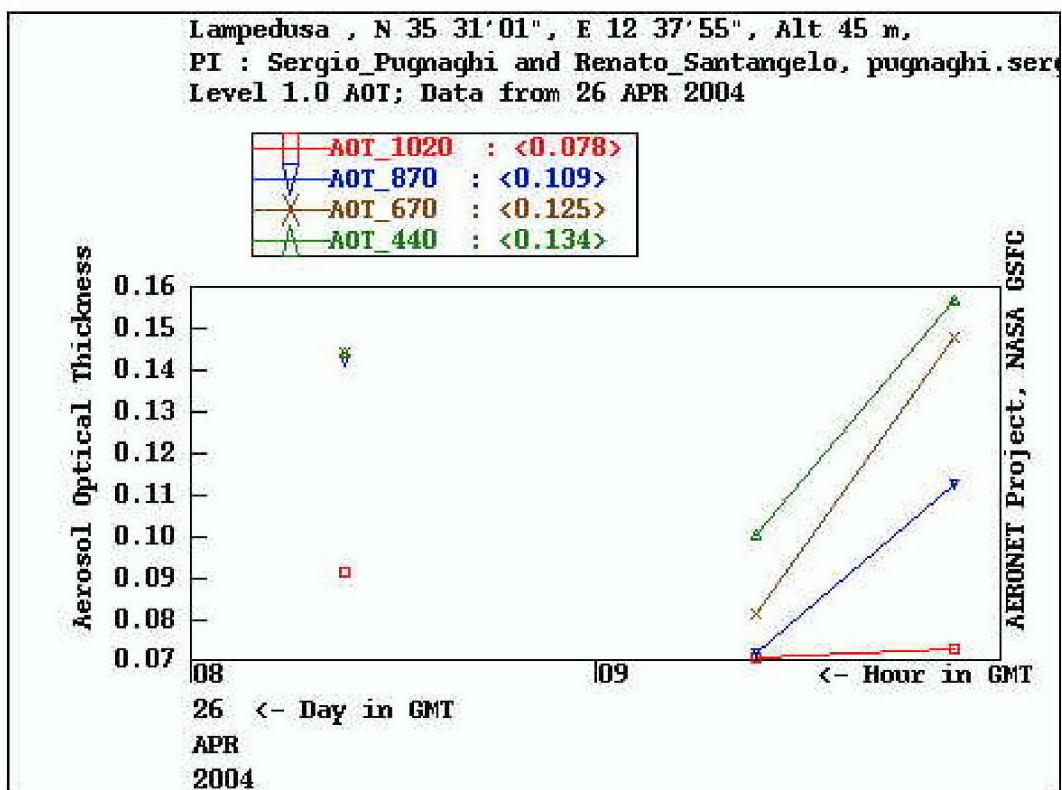Figure 78.   AERONET data from Dhabi, near Persian Gulf

Figure 79.   AERONET data from Lampedusa, near Libya, 26 Apr 2004
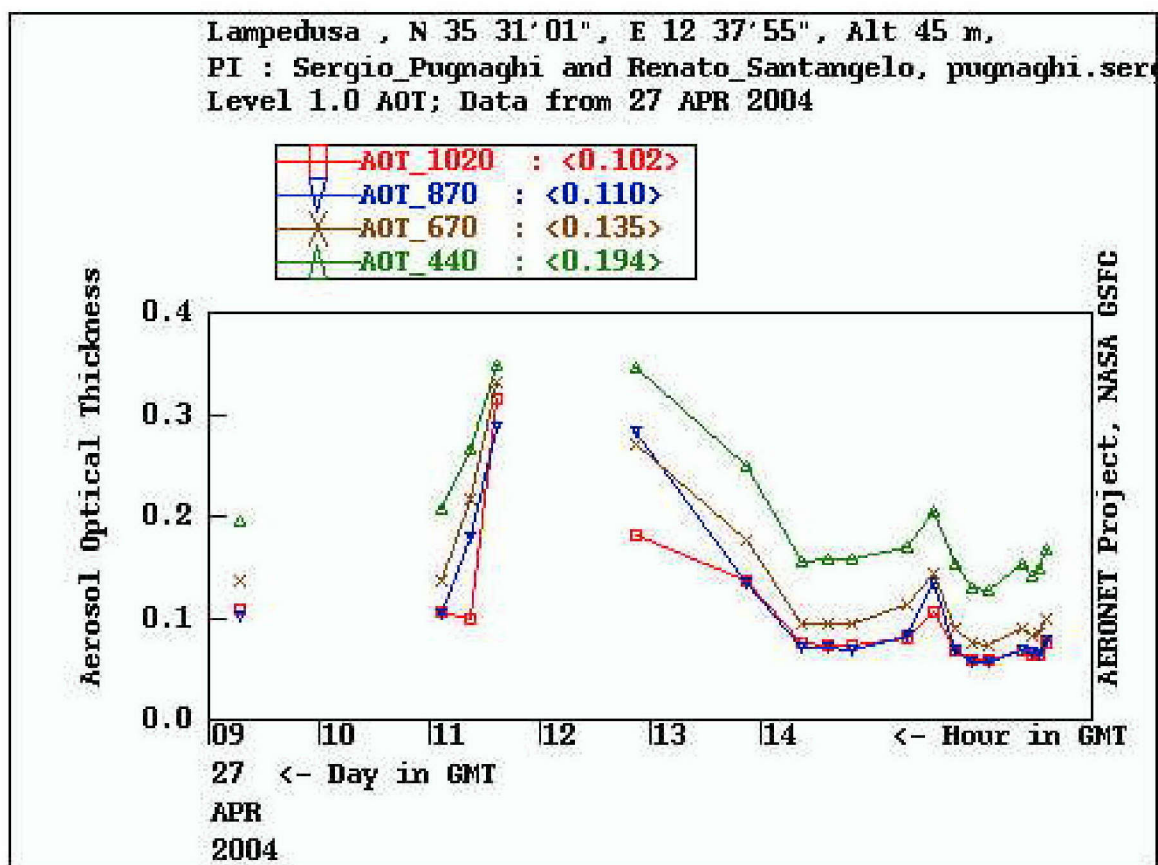
Figure 80.   AERONET data from Lampedusa, near Libya, 27 Apr 2004

LIST OF REFERENCES

Air Force Weather (2004). Air Force weather transformation: Strategic plan and vision FY2008-2032, U.S. Air Force distribution, 18 pp.

Brown, B. A. (2002). Aerosol optical depth retrieval by NPS model modified for SeaWiFS input. M.S. Thesis, Naval Postgraduate School, Monterey, CA.

Brown, B. B. (1997). Remote measurement of aerosol optical properties using the NOAA POES AVHRR and GOES Imager during TARFOX. M.S. Thesis, Naval Postgraduate School, Monterey, CA.

Conboy, B. (2002). MODIS technical specifications. site accessed March 2005, (Available online at http://modis.gsfc.nasa.gov/about/specs.html)

Durkee, P. A. (2004). MR3522 Remote Sensing of the Atmosphere and Oceans, Classroom and Naval Postgraduate School Blackboard Lecture Notes.

Durkee, P. A., D. R. Jensen, E. E. Hindman, and T. H. Vonder Haar (1986). The relationship between marine aerosol particles and satellite-derived radiance. J. Geophys. Res., 91, 4063-4072.

Feldman, G. C. (1997). An overview of SeaWiFS and the SeaStar spacecraft. site accessed March 2005, (Available online at http://seawifs.gsfc.nasa.gov/SEAWIFS/SEASTAR/SPACECRAFT.html)

Holbren, B. (2004). Aerosol Robotic Network (AERONET) federated network background. site accessed March 2005, (Available online at http://aeronet.gsfc.nasa.gov/F_Info/system_info_additional.html)

Kidder, S. Q. and T. h. Vonder Haar (1995). Satellite Meteorology, An Introduction. Academic Press, San Diego.

NASA Goddard Space Flight Center (2005a). AERONET data images generated using NASA AERONET project web site. site accessed March 2005, (http://aeronet.gsfc.nasa.gov/data_menu.html).

NASA Goddard Space Flight Center (2005b). MODIS Rapid Response – Image Gallery, site accessed March 2005, (http://rapidfire.sci.gsfc.nasa.gov/gallery/)

NASA Jet Propulsion Laboratory (2005). MISR's science objectives, site accessed March 2005, (Available online at http://www-misr.jpl.nasa.gov/mission/iangles.html).

NOAA (2002). NOAA KLM User's Guide, Appendix D.3. site accessed March 2005, (Available online at http://www2.ncdc.noaa.gov/docs/klm/html/d/app-d3.htm#td3-10)

US Geological Survey (2004) Advanced Very High Resolution Radiometer (AVHRR) product description. site accessed March 2005, (Available online at http://edc.usgs.gov/products/satellite/avhrr.html)

Wallace, J. M. and P. V. Hobbs (1977). Atmospheric Science: An Introductory survey. Academic Press, New York.

INITIAL DISTRIBUTION LIST

1. Defense Technical Information Center
    Ft. Belvoir, Virginia

2. Dudley Knox Library
    Naval Postgraduate School
    Monterey, California

3. Air Force Weather Technical Library
    Asheville, North Carolina

4. Air Force Institute of Technology
    Wright-Patterson Air Force Base, Ohio

5. Professor Philip A. Durkee
    Naval Postgraduate School
    Monterey, California

6. Professor Carlyle H. Wash
    Naval Postgraduate School
    Monterey, California

7. Kurt Nielsen
    Naval Postgraduate School
    Monterey, California

8. Captain Daniel P. Wunder
    Air Force Combat Climatology Center
    Asheville, North Carolina